



Cite this: RSC Adv., 2017, 7, 28234

Two-dimensional transition metal dichalcogenide-based counter electrodes for dye-sensitized solar cells

 Eric Singh, ^{abc} Ki Seok Kim, ^b Geun Young Yeom ^{*bc} and Hari Singh Nalwa ^{*d}

Dye-sensitized solar cells (DSSCs) are gaining considerable interest as alternatives to semiconductor-based thin film solar cells. The noble metal platinum (Pt) is conventionally used as a counter electrode (CE) material for fabricating DSSCs, since Pt is expensive and scarce, therefore, new materials have been explored to develop cost-effective Pt-free counter electrodes. Two-dimensional (2D) graphene-based counter electrodes have achieved the highest power conversion efficiency (PCE, η) of 13%, which has stimulated research activities in 2D layered transition metal dichalcogenides (TMDs) for developing Pt-free DSSCs. In this review, progress made on alternative counter electrodes for fabricating low-cost Pt-free DSSCs, based on earth-abundant 2D TMDs including MoS_2 , WS_2 , TiS_2 , FeS_2 , CoS_2 , NiS_2 , SnS_2 , MoSe_2 , NbSe_2 , TaSe_2 , NiSe_2 , FeSe_2 , CoSe_2 , Bi_2Se_3 and their based composites, are discussed and summarized. Also, the considerable progress made on thin films of MoS_2 and MoS_2 based carbon, graphene, carbon nanotubes (CNTs), carbon nanofibers (CNFs), and poly(3,4-ethylenedioxythiophene):poly(styrenesulfonate) (PEDOT:PSS) composites as efficient counter electrodes (CEs) for DSSCs are discussed, in terms of their electrochemical and photovoltaic properties. At present, PCE values higher than that of standard Pt CE have been recorded for a number of TMD-based CEs, which include MoS_2 and MoSe_2 /thin films deposited on Mo foil, MoS_2 /CNTs, MoS_2 /graphene, MoS_2 /carbon, MoSe_2 /PEDOT:PSS, NbSe_2 , FeS_2 , FeSe_2 nanosheets, TiS_2 /graphene, and NiS_2 /graphene hybrid systems in DSSCs, for the reduction of triiodide (I_3^-) to iodide (I^-). The highest PCE ($\eta = 10.46\%$) versus Pt CE ($\eta = 8.25\%$) at 1 Sun (100 mW cm^{-2} , AM 1.5G) was measured for DSSCs having a low cost and flexible CoSe_2 /carbon-nanoclimbing wall counter electrode deposited on a nickel foam. Though TMD-based materials show great potential for solar cell devices, their long-term stability is equally important. The DSSCs with a TiS_2 /graphene hybrid, and TiS_2 /PEDOT:PSS composite CEs, showed stability up to 20 to 30 days, respectively, without any measurable degradation in the photovoltaic performance. The long-term stability of TMDs-based DSSCs under different environmental conditions is also described in view of their commercial applications.

Received 28th March 2017
 Accepted 14th May 2017

DOI: 10.1039/c7ra03599c
rsc.li/rsc-advances

1. Introduction: dye-sensitized solar cells (DSSCs)

Silicon has been traditionally used in fabricating solar cells. O'Regan and Grätzel¹ in 1991 demonstrated dye-sensitized solar cells (DSSC) as a low-cost approach and as an alternative to silicon solar cells. The concept of a DSSC system was hypothesized based on photosynthesis in nature. The first DSSC was

fabricated using nanocrystalline porous TiO_2 as optically transparent thin-film photoelectrodes and a ruthenium(II)-bipyridyl complex as a photosensitizer (dye), which generated a power conversion efficiency of 7.9% for the triiodide/iodide (I_3^-/I^-) redox couple. This inspired a new field of research based on DSSCs where a broad range of novel materials are now being explored for electrodes (photoanode and counter electrode (CE; cathode)), photosensitizers (dyes), and reduction-oxidation (redox) electrolytes for fabricating DSSC devices.

The commonly used components in dye-sensitized solar cells are a photoanode, a CE, a photosensitizing dye, and an electrolyte. These include tris(2,2'-bipyridyl) cobalt(II/III) [$\text{Co}(\text{bpy})_3$] ($\text{Co}^{2+}/\text{Co}^{3+}$), triiodide/iodide (I_3^-/I^-) and 5,5'-dithiobis(1-methyltetrazole)/1-methyltetrazole-5-thiolate (T_2/T^-) as redox couples, poly(3,4-ethylenedioxythiophene) (PEDOT), poly(styrenesulfonate) (PSS), poly(3-hexylthiophene) (P3HT), 2,2',7,7'-tetrakis(*N,N*-*p*-dimethoxy-phenylamino)-9,9'-spirobifluorene (spiro-OMTAD) as solid-state hole-transport

^aDepartment of Computer Science, Stanford University, Stanford, California 94305, USA

^bSchool of Advanced Materials Science and Engineering, Sungkyunkwan University, 2066 Seobu-ro, Jangan-gu, Suwon-si, Gyeonggi-do 16419, South Korea. E-mail: ggyeom@skku.edu

^cSKKU Advanced Institute of Nano Technology, Sungkyunkwan University, 2066 Seobu-ro, Jangan-gu, Suwon-si, Gyeonggi-do 16419, South Korea

^dAdvanced Technology Research, 26650 The Old Road, Valencia, California 91381, USA. E-mail: nalwa@mindspring.com



materials (HTM); *cis*-bis(isothiocyanato)bis(2,2'-bipyridyl-4,4'-dicarboxylato)ruthenium(II), (N3 dye), ditetrabutylammonium *cis*-bis(isothiocyanato)bis(2,2'-bipyridyl-4,4'-dicarboxylato)ruthenium(II), where tetrabutyl-ammonium cation: $[(C_4H_9)_4N^+]$ (N719 dye), and (tris(cyanato)-2,2',2"-terpyridyl-4,4',4"-tricarboxylate)ruthenium(II) (N749 or black dye) as photosensitizing dyes, are regularly used. The dye-sensitized mesoporous TiO_2 is used as a photoanode, while the Pt-coated fluorine-doped tin oxide (FTO) on a glass substrate is used as a CE, which facilitates the catalysis process. The counter electrode in a DSSC device acts as a catalyst. Pt counter electrodes yield the maximum electrocatalytic activity for the triiodide/iodide (I_3^-/I^-) redox couple, but are poorly effective for iodine-free redox couple such as Co^{2+}/Co^{3+} and T_2/T^- . Transparent conducting oxides such as FTO or indium-tin oxide (ITO) on glass is the common substrate used in assembling DSSCs with different CE materials. The power conversion efficiency of DSSCs is governed by many factors including light absorbing capacity of photosensitizing dyes and catalytic materials.

The classical photosensitizing dyes were developed by Grätzel's research team,^{2,3} including N3 dye that absorbs up to 800 nm, and N749 dye (also known as black dye) which absorbs sunlight in the longer wavelength region up to 920 nm. In 2014, Mathew *et al.*⁴ used graphene nanoplatelets as a CE, a new push-pull porphyrin with a donor- π -bridge acceptor (D- π -A) chemical structure as a sensitizing dye, and $Co(II)/Co(III)$ redox mediator for developing a DSSC, which exhibited a J_{sc} of 18.1 mA cm^{-2} , V_{oc} of 0.91 V , FF of 0.78 and the highest power conversion efficiency (PCE) of 13% under 100 mW cm^{-2} (AM 1.5) illumination. The high PCE of DSSCs originated from a molecularly engineered porphyrin dye, 4-[7-{2-[2Z,7Z,11E,16Z]-7,17-bis[2,6-bis(octyloxy)phenyl]-12-[bis({4-[2,4-bis(hexyloxy)phenyl]}phenyl})amino]-21,23,24,25-tetraaza-22-zincahexacyclo[9.9.3.13,6.113,16.08,23.018,21]-pentacos-1(20),2,4,6(25),7,9,11,13(24),14,16,18-undecane-2-yl]-ethynyl]-2,1,3-benzothiadiazole-4-yl]benzoic acid, coded as SM315 dye. The sensitizing dyes as a light harvester play a very significant role in achieving high PCE for DSSCs, therefore, dyes such as N3, N719, N749, Y123, Z907, JK-303 those absorb as much sunlight as possible is of a great interest, *i.e.*, Y123 dye = 3-[6-[4-[bis(2',4'-dihexyloxybiphenyl-4-yl)amino]-]phenyl]-4,4-dihexylcyclopenta-[2,1-b:3,4-b]dithiphene-2-yl]-2-cyanoacrylic acid; Z907 = *cis*-bis(isothiocyanato) (2,2'-bipyridyl-4,4'-dicarboxylato) (4,4'-di-nonyl-2'-bipyridyl)ruthenium(II); and JK-306 = (E)-3-[5'-{4-[bis(2',4'-dihexyloxybiphenyl-4-yl)amino]phenyl}-2,2'-bithiophene-5-yl]-2-cyanoacrylic acid. The many types of dye-sensitizers such as ruthenium dyes, metal-free organic dyes, porphyrin dyes, quantum dots, and perovskites have been explored for DSSCs. Over the past 30 years, significant progress has been made in exploring diverse aspects of DSSC components, including dye-sensitizers, CEs, electrolytes and photoanodes, and many outstanding reviews are available in the literature on this exciting research topic.⁵⁻¹⁷ Chemical structures of photosensitizing dyes generally used in evaluating the photovoltaic performance of CEs in DSSCs are also discussed elsewhere. Many different types of Pt-free CE materials have been studied for DSSCs including carbon-based materials such as carbon black, mesoporous carbon, carbon nanotubes

(CNTs), carbon fibers, fullerenes, graphene-based materials, metals, transition metal oxides, sulfides, carbides, nitrides, selenides, tellurides, chalcogenides, layered double hydroxides, phosphides and their alloys, conducting polymers such as PEDOT:PSS and other composites materials.¹⁸⁻²²

Platinum (Pt) and ITO are the traditional materials used in fabricating different types of solar cell devices. In DSSCs, the Pt deposited on a FTO transparent conductive glass substrate is used as a CE for the reduction of triiodide (I_3^-) ions to iodide (I^-) ions. In this case, Pt acts as a catalyst for the regeneration of redox couples while FTO acts as an electron collector. Pt is a highly expensive metal which has been identified as one of the most critically important metals for the U.S. economic growth.^{23,24} Among electrocatalysts for DSSCs, Pt shows the best photovoltaic performance due to its high conductivity, chemical stability, and electrochemical activity but it is scarce. The current idea is to explore new alternative catalytic materials to replace the conventional Pt CE in DSSCs using easily available, inexpensive, highly electrically conductive, and high electrocatalytic activity materials. Earth-abundant 2D materials that offer high optical transparency and high electrocatalytic activity have been explored as potential candidate materials for CEs (cathode) and for replacing Pt in DSSC devices. During the last decade, graphene-based materials in the form of their thin films, nanosheets, fibers, multilayers, nanoplatelets, quantum dots, nanofoams and their nanocomposites with metals, CNTs, organic polymers, upconversion nanoparticles, titanium dioxide (TiO_2), ionic liquids, and halide perovskites, have been extensively investigated as Pt-free CEs for DSSCs²⁵ and heterojunction solar cells.^{26,27} The merit of graphene-based CEs in DSSC devices includes their high optical transparency, high electrical conductivity, large effective specific surface area, and the flexibility to fabricate them on different types of substrates.

Layered 2D TMDs are graphene analogs, therefore, research activities have been strongly diverted towards this new class of low-cost 2D materials. Among 2D TMDs, transition-metal disulfides and diselenides such as MoS_2 , $MoSe_2$, WS_2 , TiS_2 , $NbSe_2$, $TaSe_2$, $NiSe_2$, $FeSe_2$, $CoSe_2$, SnS_2 , Bi_2Se_3 and other TMD thin films have been investigated as CEs to fabricate Pt-free DSSCs. The CE acts as an electrocatalyst, and is one of the main components of a DSSC device which facilitates the reduction of triiodide (I_3^-) ions to iodide (I^-) ions in a redox electrolyte for dye generation. In this review, electrochemical and photovoltaic properties of low-cost catalytic CEs developed from earth-abundant TMDs and their composites with carbon, graphene, CNTs, carbon nanofibers, PEDOT:PSS and other materials are discussed. The impact of materials processing and morphology associated with PCEs of DSSCs has also been analyzed. Finally, this review discusses the electrochemical and environmental stability of TMDs-based CEs for DSSCs.

2. Two-dimensional transition metal dichalcogenides (2D TMDs)

Two-dimensional (2D) transition metal dichalcogenides (TMDs), *i.e.* MX_2 where M is a transition metal (Mo, W, Ti, Zr,



Table 1 Library of 2D materials. Blue cells represent monolayers of 2D materials showing stability under ambient conditions; green denotes probability of stability of 2D materials in air; pink denotes 2D unstable materials in air, but may be stable under inert atmosphere. Grey cells show 3D compounds easily exfoliated down to monolayers. Reprinted with permission from ref. 32, A. K. Geim and I. V. Grigorieva, van der Waals heterostructures. *Nature*, 2013, **499**, 419–425. Copyright © Nature Publishing Group

Graphene family	Graphene	hBN 'white graphene'	BCN	Fluorographene	Graphene oxide
2D chalcogenides	MoS ₂ , WS ₂ , MoSe ₂ , WSe ₂	Semiconducting dichalcogenides: MoTe ₂ , WTe ₂ , ZrS ₂ , ZrSe ₂ and so on		Metallic dichalcogenides: NbSe ₂ , NbS ₂ , TaS ₂ , TiS ₂ , NiSe ₂ and so on	
				Layered semiconductors: GaSe, GaTe, InSe, Bi ₂ Se ₃ and so on	
2D oxides	Micas, BSCCO	MoO ₃ , WO ₃	Perovskite-type: LaNb ₂ O ₇ , (Ca,Sr)Nb ₃ O ₁₀ , Bi ₄ Ti ₃ O ₁₂ , Ca ₂ Ta ₂ TiO ₁₀ and so on	Hydroxides: Ni(OH) ₂ , Eu(OH) ₂ and so on	
	Layered Cu oxides	TiO ₂ , MnO ₂ , V ₂ O ₅ , TaO ₃ , RuO ₂ and so on			Others

Hf, V, Nb, Ta, Tc, Re, Pd, Pt) and X is a chalcogen (S, Se, Te), such as MoS₂, WS₂, MoSe₂, WSe₂, form 2D layered structures and are abundantly available in nature. In a MX₂ monolayer structure (X-M-X), an atomic layer of a transition metal (M) is sandwiched between two chalcogen (X) atomic layers, where transition metal atoms (M) such as Mo and W are covalently bonded with chalcogen atoms (X) such as S, Se, Te. Each layer is 6–7 Å thick in the TMD layered structures. Weak van der Waals interactions occur between two adjacent MX₂ layers of TMDs, whereas the intra-layer M-X bonds are covalent.^{28–31} From an electrical point of view, MoS₂, MoSe₂, WS₂ and WSe₂ are semiconductors, WTe₂ and TiSe₂ are semimetals, VSe₂ and NbS₂ are metals, while NbSe₂ and TaS₂ are superconductors in their bulk crystalline forms.^{26,30} Geim and Grigorieva³² created a library of 2D materials (Table 1) where the 2D materials were classified into three different classes. Their graphene family includes graphene-based materials hBN, and BCN; the 2D chalcogenides include a large family of TMDs having insulator to semiconducting to metallic behavior; and the 2D oxides include layered oxides, perovskite-based materials, hydroxides, and others. The 2D TMDs include MoS₂, WS₂, VS₂, NbS₂, ZrS₂, TiS₂, NbSe₂, WSe₂, MoSe₂, ZrSe₂, WTe₂, and MoTe₂, and layered semiconductor chalcogenides such as GaSe, GaTe, InSe, Bi₂Se₃, and Bi₂Te₃. 2D materials represented by different colors denote their stability under ambient conditions. 2D materials among the graphene family have been extensively studied so far. 2D TMDs such as MoS₂, WS₂, WSe₂ and MoSe₂ are structurally similar. Among 2D TMDs, W based materials have stronger spin-orbit coupling while Se materials exhibit lower stability.

Research activities into 2D TMDs were intensified after the monolayers of MoS₂ showed high carrier mobility of 100 cm² V^{−1} s^{−1} and on/off current ratios of $>10^8$ because of the interesting bandgap of MoS₂.³³ The monolayers of MoS₂ are direct semiconductors whereas MoS₂ bilayers, trilayers, few-layers are indirect semiconductors. Thickness dependent bandgap energies of 2D TMDs-based semiconductors, including MoS₂, MoSe₂, MoTe₂, WS₂, and WSe₂ (2H-MX₂), were calculated by

Yun *et al.*³⁴ using the first-principles calculations as shown in Fig. 1.³⁴ As the number of layers in the TMDs is reduced to a single layer, the band curvatures lead to significant changes of effective masses. When a single layer of the TMDs is strained, the direct bandgap turns to an indirect bandgap. It was found that bandgap energy and effective masses are reduced by tensile strain, contrary to the compressive strain that increases both parameters. Also the applied larger tensile stress gives rise to a metallic character. This study emphasized the electronic structures of 2D TMDs.

The photoluminescence and absorption spectra of monolayers of MoS₂, MoSe₂, WS₂, and WSe₂ have been measured.³⁵ TMDs as bulk crystals are indirect-bandgap semiconductors, however they become direct-bandgap semiconductors as their thickness is reduced to monolayers. The bandgap increases as the number of layers decreases. Photoluminescence peaks at

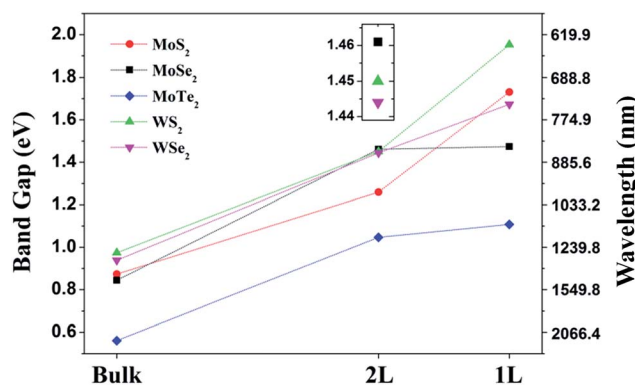


Fig. 1 Colored lines representing thickness dependence of bandgap energies of 2D TMDs including MoS₂, MoSe₂, MoTe₂, WS₂, and WSe₂ attain (2H-MX₂ semiconductors). Reprinted with permission from ref. 34, W. S. Yun, S. W. Han, S. C. Hong, I. G. Kim and J. D. Lee, thickness and strain effects on electronic structures of transition metal dichalcogenides: 2H-MX₂ semiconductors (M = Mo, W; X = S, Se, Te). *Phys. Rev. B*, 2012, **85**, 033305. Copyright © American Physical Society.



1.84 eV for MoS_2 , 1.65 eV for WSe_2 and 1.56 eV for MoSe_2 have been observed.³⁶ The indirect bandgap at 1.2 eV for bulk crystals of WSe_2 was reported,³⁷ whereas the monolayer showed a photoluminescence peak at 1.65 eV (752 nm). In the case of bulk crystals of MoSe_2 , the indirect bandgap was measured as 1.1 eV (1.13 μm) while the monolayer exhibited a photoluminescence peak at 1.57 eV (792 nm). The photoluminescence emission peak for monolayer WS_2 appeared at 1.97 eV.³⁸

Mechanical exfoliation is the most common approach for peeling off monolayers or a few-layers of TMD materials from their bulk crystals,^{39–41} which is a top-down method. A second widely used approach is chemical vapor deposition (CVD), which is a bottom-up method to consecutively deposit desired thickness layers of TMDs.^{42–45} Other approaches for preparing layers of TMDs include chemical,⁴⁶ lithium intercalation,^{47–49} and ultrasonic-assisted liquid exfoliation in organic solvents,^{50–54} and salt-assisted liquid-phase exfoliation,⁵⁵ all of

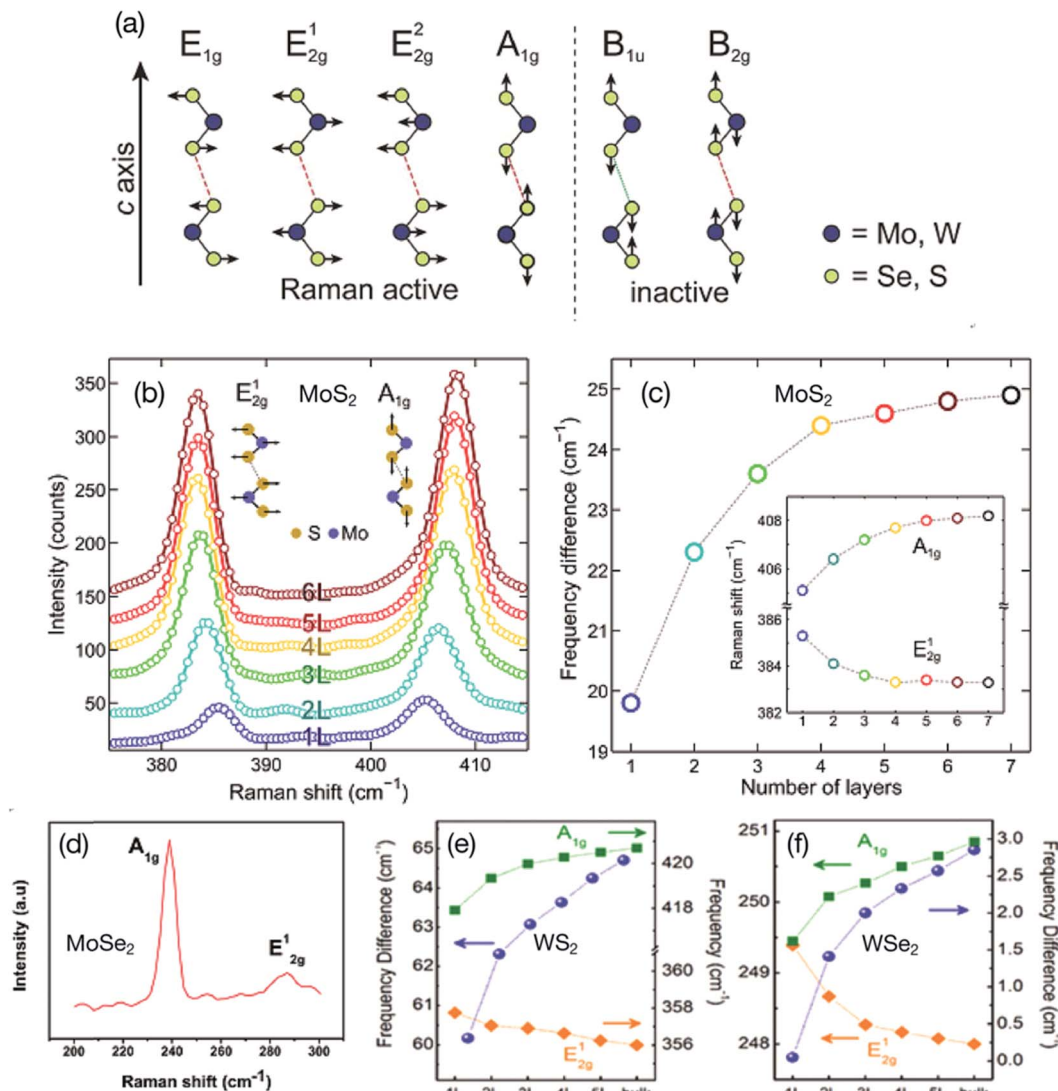


Fig. 2 (a) Schematic representation of the four Raman active modes and two Raman inactive modes of TMDs MX_2 ($\text{M} = \text{Mo, W}$ and $\text{X} = \text{Se, Se}$). Reprinted with permission from ref. 37, P. Tonndorf, R. Schmidt, P. Böttger, X. Zhang, J. Börner, A. Liebig, M. Albrecht, C. Kloc, O. Gorgan, D. R. T. Zahn, S. M. de Vasconcellos and R. Bratschitsch, Photoluminescence Emission and Raman Response of Monolayer MoS_2 , MoSe_2 , and WSe_2 . *Opt. Express*, 2013, **21**, 4908–4916. Copyright© Optical Society of America. (b) Raman spectra of mechanically exfoliated MoS_2 flakes deposited onto a transparent poly(dimethylsiloxane) (PDMS) substrate with different number of layers, single-layer to six-layers of MoS_2 . (c) Peak frequency difference (Δ) between Raman modes as a function of the number of MoS_2 layers. Reprinted with permission from ref. 60, A. Castellanos-Gomez, J. Quereda, H. P. van der Meulen, N. Agrait and G. Rubio-Bollinger, spatially resolved optical absorption spectroscopy of single-and few-layer MoS_2 by hyperspectral imaging. *Nanotechnol.*, 2016, **27**, 115705. Copyright© Institute of Physics (IOP). (d) Raman spectrum of single-and few-layer MoSe_2 nanosheets showing two distinct Raman active modes; A_{1g} and E_{2g}^1 . Reprinted with permission from ref. 61, S. K. Balasingam, J. S. Lee and Y. Jun, few-layered MoSe_2 nanosheets as an advanced electrode material for supercapacitors, *Dalton Trans.*, 2015, **44**, 15491–15498. Copyright© Royal Society of Chemistry. (e, f) Thickness dependence of Raman A_{1g} and E_{2g}^1 modes of 1 to 5 layers and bulk WS_2 and WSe_2 . Reprinted with permission from ref. 62, W. Zhao, Z. Ghorannevis, K. K. Amara, J. R. Pang, M. Toh, X. Zhang, C. Kloc, P. H. Tan and G. Eda, lattice dynamics in mono-and few-layer sheets of WS_2 and WSe_2 . *Nanoscale*, 2013, **5**, 9677–9683. Copyright© Royal Society of Chemistry.



which can prepare mono-layers to multi-layers of TMDs, such as MoS₂, MoSe₂, WS₂, and WSe₂.

Raman scattering methods for single-layer, multi-layer and bulk 2D TMDs, including MoS₂, MoSe₂, WS₂, and WSe₂, in terms of phonons with respect to the number of layers, has been reviewed and analyzed.^{56,57} Tonndorf *et al.*³⁷ studied photoluminescence and Raman characteristics of the monolayers of MoS₂, MoSe₂, and WSe₂. Fig. 2a shows a schematic representation of the four Raman active modes and two Raman inactive modes of TMDs MX₂ (M = Mo, W and X = Se, Se) as predicted for the D6h point group.⁵⁸ The Raman active modes include three in-plane modes referred as E_{1g}, E_{2g}¹ and E_{2g}², and one out-of-plane mode referred as A_{1g}. However, experimentally only the two active Raman modes E_{2g}¹ and A_{1g} were observed. The active Raman E_{2g}² mode appears at very low frequencies, whereas the E_{1g} mode is forbidden.⁵⁹ A systematic study of the optical absorption of single-layer and few-layers of MoS₂ from the 385 nm (3.22 eV) to 1000 nm (1.24 eV) spectral range was conducted by Castellanos-Gomez *et al.*⁶⁰ using a hyperspectral imaging technique. Poly(dimethylsiloxane) (PDMS) was used as a transparent substrate for depositing mechanically exfoliated MoS₂ thin films. The optical absorbance spectra of MoS₂ flakes consisting of single-layer to six-layer were recorded as a function of different excitation wavelengths. The bandgap of a monolayer MoS₂ was measured as 1.85 eV, which decreased with increasing number of MoS₂ layers, reaching a bandgap value of 1.35 eV for the bulk MoS₂. Fig. 2b and c shows Raman spectra for the E_{2g}¹ and A_{1g} modes of the exfoliated MoS₂ flakes ranging from single-layer to six-layer, and the variation of peak frequency difference (Δ) between the E_{2g}¹ and A_{1g} modes as a function of the number of MoS₂ layers. The Δ value increases with the increasing number of layers from 19.8 cm⁻¹ for a single-layer to 25 cm⁻¹ for bulk MoS₂.

Raman spectroscopy for few-layer MoSe₂ nanosheets was recorded by Balasingam *et al.*⁶¹ which showed Raman peaks at 239 cm⁻¹ and 287.11 cm⁻¹ (Fig. 2d) corresponding to the A_{1g} mode (out-of-plane) and E_{2g}¹ mode (in-plane) of MoSe₂, respectively. For bulk crystal MoSe₂, the A_{1g} and E_{2g}¹ modes appear at 242 cm⁻¹ and 286 cm⁻¹, respectively. The red shift in the A_{1g} mode and a blue shift in the E_{2g}¹ mode indicate the formation of a few-layered MoSe₂ nanosheet. Raman spectra of monolayers, few-layers and bulk WS₂ and WSe₂ were evaluated by Zhao *et al.*⁶² Thickness dependent Raman A_{1g} and E_{2g}¹ modes of 1 to 5 layers, as well as bulk WS₂ and WSe₂, are shown in (Fig. 2e and f). As discussed above, the frequency difference (Δ) can be used to distinguish the number of layers. McCreary *et al.*³⁸ reported the E_{2g}¹ mode at 357.5 cm⁻¹ (in-plane) and A_{1g} mode at 419 cm⁻¹ (out-of-plane) with a frequency difference (Δ) of 61.5 cm⁻¹ for WS₂ monolayer. Photoluminescence emission and Raman scattering of 2D TMDs have been extensively studied and analyzed by several research groups around the world.⁶³⁻⁷¹

3. TMD-based counter electrodes for DSSCs

The new materials used as CEs in DSSC devices are generally characterized by their molecular structure and surface

morphology using a wide variety of spectroscopic techniques, including X-ray diffraction (XRD), Raman spectroscopy, X-ray photoelectron spectroscopy (XPS), UV-vis (Ultraviolet-visible) spectrometry, atomic force microscopy (AFM), field-emission scanning electron microscopy (FESEM), high-resolution transmission electron microscopy (HRTEM) and energy dispersive X-ray spectroscopy (EDX). The electrochemical catalytic activity and photovoltaic performance of CEs in DSSCs are evaluated using different methods. Electrocatalytic activity can be evaluated by cyclic voltammetry (CV), rotating disk electrode (RDE) for determining rate constant and effective catalytic surface area, interfacial charge transfer parameters (series resistance and charge-transfer resistance) measurements by electrochemical impedance spectroscopy (EIS) and Tafel polarization plots for electrocatalytic ability, incident photon-to-current conversion efficiency (IPCE) spectra measurements; these measurements of a DSSC device and their electro-catalytic activities are compared with a standard Pt CE. Photovoltaic tests of a DSSC device are performed by measuring photocurrent density-voltage ($J-V$) characteristic curves of CEs under a simulated solar illumination at 100 mW cm⁻² (AM 1.5G) corresponding to 1 Sun intensity unless specified for other sunlight intensity. The photovoltaic and electrochemical parameters of the DSSC system include short-circuit photocurrent density (J_{sc}), open-circuit voltage (V_{oc}), fill factor (FF), power conversion efficiency (PCE) which is the solar-to-electricity conversion efficiency (η), series resistance (R_s), charge-transfer resistance (R_{CT}) at the CE/electrolyte interface, capacitance, and Nernst diffusion impedance (Z_N). When using a new material as a CE catalyst, the electrochemical and photovoltaic properties of a DSSC device are compared with a conventional Pt CE due to its optimal electrocatalytic activity and chemical stability in the electrolyte. The dye-adsorbed TiO₂ mesoporous film deposited on a FTO glass substrate is used as a photoanode (working electrode) of the DSSC device. The ruthenium N719 dye has been commonly used for the reduction of triiodide (I₃⁻) to iodide (I⁻). DSSCs are assembled with different CEs to be studied, and filled with the same redox electrolyte solution such as triiodide/iodide (I₃⁻/I⁻) redox couple. The CE reduces the triiodide (I₃⁻) ions to iodide ions (I⁻). For example, a typical iodide electrolyte solution contains 0.1 M of LiI, 0.05 M of iodine (I₂), 0.6 M of 1,2-dimethyl-3-n-propylimidazolium iodide (DMPII), and 0.5 M of 4-*tert*-butylpyridine (TBP) in acetonitrile. All these spectroscopic techniques and electrochemical measurements were performed, which have been discussed throughout this review as needed in order to evaluate the potential of 2D TMDs (such as MoS₂, WS₂, TiS₂, FeS₂, CoS₂, NiS₂, SnS₂, MoSe₂, NbSe₂, TaSe₂, NiSe₂, FeSe₂, CoSe₂, Bi₂Se₃ and their based hybrids/composites) as CEs for fabricating low-cost Pt-free DSSCs.

3.1 MoS₂ counter electrodes

3.1.1 Pristine MoS₂. TMDs have been traditionally used as solid lubricants⁷²⁻⁸⁰ but recently have found the potential for applications in the fields of electronics and photonics. Like 2D graphene-based materials, layered transition-metal



dichalcogenides MX_2 ($\text{M} = \text{W}, \text{Mo}, \text{Hf}, \text{Nb}, \text{Re}, \text{Ta}; \text{X} = \text{S}, \text{Se}, \text{Te}$) have become of great interest due to their unique electronic and photonic properties and a very wide range of applications in field-effect transistors (FETs),^{81–99} photodetectors,^{100–102} light-emitting diodes (LEDs),^{103,104} ferroelectric memories,¹⁰⁵ static random access memory (RAM),⁸³ high-frequency resonators,¹⁰⁶ supercapacitors,^{107,108} energy conversion and storage devices,^{109–112} gas sensors,^{113,114} biosensors,^{115,116} biomedical applications,¹¹⁷ organic solar cells,¹¹⁸ and photonics/optoelectronics.^{119,120}

TMDs are one of the 2D graphene analogs which show great potential for both bulk-heterojunction (BHJ) and dye-sensitized solar cells. A review article on atomically thin MoS_2 layers used as the electron-transport layer (ETL), hole-transport layer (HTL), interfacial layer, and protective layer in fabricating bulk-heterojunction (BHJ) solar cells has been recently published by Singh *et al.*¹¹⁸ Here, the applications of MoS_2 thin films as CEs for fabricating Pt-free dye-DSSCs are discussed.

Polytypism in MoS_2 has been studied by using Raman spectroscopy.¹²¹ Layered MoS_2 exists in 2H, 3R and 1T phases where monolayers are stacked in a different sequence.^{122–124} The semiconducting 2H- MoS_2 phase of the bulk crystal contains two-layer per unit cell stacked in a hexagonal symmetry, where each Mo atom is coordinated with six sulfur (S) atoms. The 3R- MoS_2 phase contains three-layer per unit cell stacked in a rhombohedral symmetry. The metallic 1T phase contains one MoS_2 layer per unit cell in tetragonal symmetry with octahedral coordination. A structural phase transition of 2H- MoS_2 to 1T- MoS_2 (2H \rightarrow 1T) has been reported due to a lithium ion

intercalation process.^{122–125} The metallic 1T phase of MoS_2 exhibits very interesting electronic properties.^{126–129} Therefore, Wei *et al.*¹³⁰ used metastable 1T metallic phase MoS_2 in fabricating DSSCs. In that work, MoS_2 films were deposited on FTO glass substrate by a hydrothermal method, performing reactions at 180 or 200 °C for 24 hours. The MoS_2 films prepared at 200 °C showed lumps, while those grown at 180 °C had flower-like structures. High-angle annular dark-field scanning transmission electron microscopy (HAADF-STEM) images, Raman spectroscopy, and XPS also showed the formation of 2H and 1T metallic phases of MoS_2 . Fig. 3 represents the J - V curves of 2H- MoS_2 and flower-structured 1T metallic phase MoS_2 . The flower-structured 1T metallic MoS_2 film was grown onto an FTO substrate as a CE of DSSC, which exhibited PCE (η) of 7.08%, that is a three times higher PCE compared with 2H phase MoS_2 ($\eta = 1.72\%$) and comparable to a Pt CE ($\eta = 7.25\%$). Such a large difference in PCE values of 1T and 2H phases occurs because the electrical conductivity of 1T- MoS_2 is 10^7 times larger compared with 2H- MoS_2 , which gives rise to a higher electrocatalytic activity for the 1T phase than that of the 2H phase. The 1T- MoS_2 CE also demonstrated lower charge-transfer resistance (R_{CT}). The IPCE curves and CV measurements also showed a better electrocatalytic activity of 1T- MoS_2 CE in DSSC than that of 2H- MoS_2 .

A very interesting study was conducted by Infant *et al.*¹³¹ who developed CE materials for DSSCs by vertically oriented MoS_2 on an FTO substrate, in order to increase the reflectivity of MoS_2 CE. Fig. 4 shows high resolution SEM images of CVD-deposited MoS_2 thin films, the reflectivity of MoS_2 CE measured by UV-vis spectrophotometer, and CV measurements using standard hydrogen electrode (SHE) as a reference electrode. The high quality thin films of MoS_2 were obtained at the optimum conditions of 600 °C with a 15 minute reaction time at a flow rate of 50 sccm. The FTO substrate is damaged if temperature is increased above 600 °C and the reaction time is over 15 minutes, leading to excessive deposition of sulfur on the surface. The layered MoS_2 thin films are polycrystalline and have 0.18–0.27 nm spacing as evidenced by the TEM image and SEAD pattern. The CVD-prepared MoS_2 thin films are vertically oriented on the FTO substrate, which yields more active sites and eventually enhance the reflectivity so that more photons are absorbed, and also created active edge sites facilitating the generation of the I^-/I_3^- redox couple. The reflectance of vertically inclined MoS_2 films on the FTO substrate was measured by a UV-vis spectrophotometer between 350–800 nm wavelength for reaction temperatures varying from 400 to 700 °C, a reaction time ranging from 5 to 30 minutes, and different flow rates of Ar gas (Fig. 4). The maximum reflectance of 38% was observed for a vertically inclined MoS_2 thin film under optimized conditions, due to high crystallinity, and the inclined angle of 26° was estimated that supports the reflectivity of photons to dye molecules. The reflectivity of 38% was observed for MoS_2 thin films prepared at 50 sccm due to its crystallinity and higher inclination angle, which contributes to more absorption photons, and hence leads to a higher PCE of 7.50% compared to PCE of 7.38% for 150 sccm with 25% reflectivity, due to smaller angle of MoS_2 inclination. This approach yielded a PCE of 7.50% for the MoS_2 CE, exceeding the PCE of Pt based CE ($\eta =$

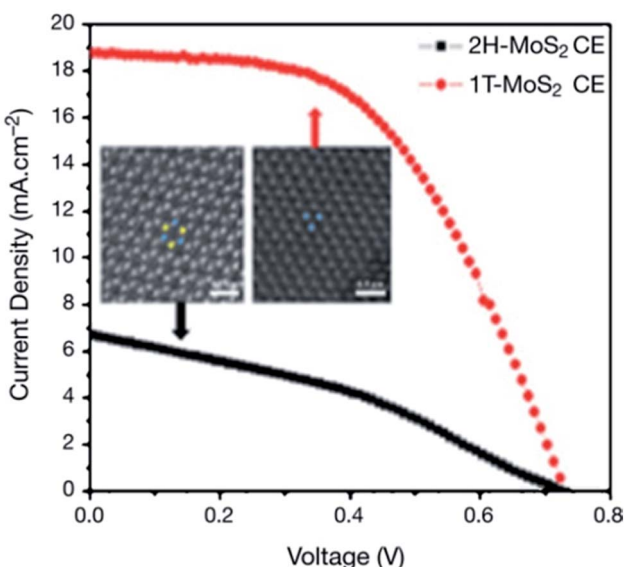


Fig. 3 Photocurrent density–voltage (J – V) curves of 2H-type MoS_2 and flower-structured 1T metallic phase MoS_2 . Insert shows high-angle annular dark-field scanning transmission electron microscopy (HAADF-STEM) confirming 2H and 1T metallic phase of MoS_2 . Reprinted with permission from ref. 130, W. Wei, K. Sun and Y. H. Hu, an efficient counter electrode material for dye-sensitized solar cells—flower-structured 1T metallic phase MoS_2 , *J. Mater. Chem. A*, 2016, 4, 12398–12401. Copyright © Royal Society of Chemistry.



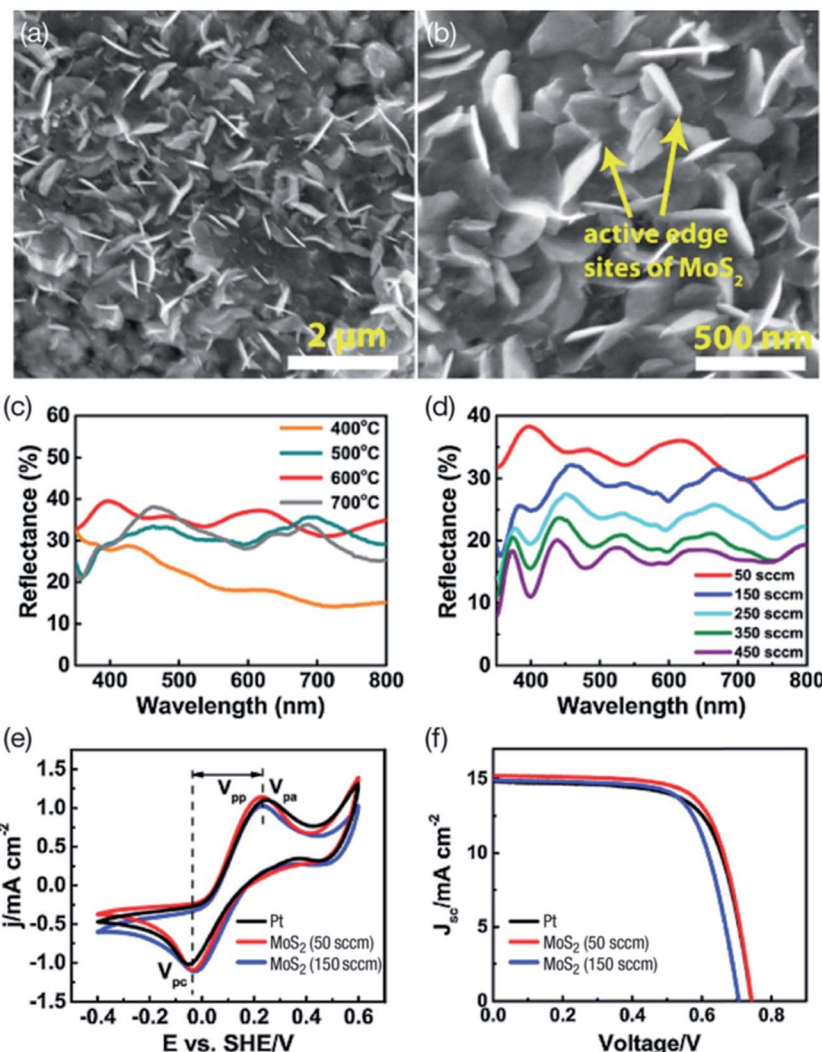


Fig. 4 SEM (a) and high resolution SEM (b) of CVD-deposited MoS₂ thin films. The highest quality thin films of MoS₂ were prepared at 600 °C with 15 minute reaction time at the Ar flow rate of 50 sccm. (c) Optical properties of MoS₂ thin films between 350–800 nm range prepared at different temperature. (d) Flow rates of Ar gas between 50 to 450 sccm for preparing MoS₂ thin films by CVD technique. (e) Cyclic voltammetry (CV) plots using standard hydrogen electrode (SHE) as a reference electrode and (f) photocurrent density–voltage (J – V) curves of MoS₂ and Pt based CEs prepared at 50 and 150 sccm flow rates of Ar gas. Reprinted with permission from ref. 131, R. S. Infant, X. Xu, W. Yang, F. Yang, L. Hou and Y. Li, highly active and reflective MoS₂ counter electrode for enhancement of photovoltaic efficiency of dye sensitized solar cells. *Electrochim. Acta*, 2016, 212, 614–620. Copyright© Elsevier.

7.28%). The MoS₂ CE shows a higher J_{sc} value of 15.2 mA cm⁻², and is higher than Pt CE ($J_{sc} = 14.6$ mA cm⁻²) due to high reflectivity. The R_{CT} of MoS₂ CE was lower than Pt CE, indicating the higher electro-catalytic activity of vertically inclined MoS₂ film on the FTO substrate was due to more active edge sites, which gives rise to enhanced electrocatalytic activity of the MoS₂ CE. Two redox peaks are observed in the CV curves of Pt and MoS₂ CEs, one corresponding to the reduction of I₃⁻, which is a cathodic peak (V_{pc}), and the other corresponding to the oxidation of I⁻, which is an anodic peak (V_{pa}). The value of anodic peak to cathodic peak separation (V_{pp}) was found to be less for the MoS₂ CE (0.456 V) than that of Pt (0.484 V), which also indicates a better electrocatalytic activity of MoS₂ CE due to the presence of active edge sites, as evidenced in the SEM images.

Vertical MoS₂ nanosheets on different substrates using CVD and CS₂ as a sulfur precursor have been developed.¹³² The DSSC CEs with vertical MoS₂ nanosheets showed a comparable electro-catalytic activity to Pt CE for the triiodide (I₃⁻) reduction, resulting from large specific surface areas and more active edges. Li *et al.*¹³³ prepared molybdenum disulfide-based CEs for DSSCs with different morphologies (multilayers, few-layers and nanoparticles) using the thermal decomposition method. The X-ray diffraction and transmission electron microscopy showed edge area to basal-plane ratio in the following order: MoS₂ nanoparticles > multilayered MoS₂ > few-layered MoS₂. A similar order was observed for the PCE values with corresponding CEs-based DSSCs. The MoS₂ nanoparticles-based CE had the minimum R_{CT} , while the few-layered MoS₂ based CE had the maximum, as measured by EIS. The active sites of MoS₂



responsible for the reduction of triiodide lie on the edges of layered materials, instead of their basal planes. MoS_2 nanoparticle CE showed the highest PCE value of 5.41%, compared with 6.58% of Pt CE. A novel approach for improving PCE of MoS_2 CE based DSSCs has been developed,¹³⁴ where electro-catalytic activity was enhanced by artificially generating active edge sites on MoS_2 atomic layers by hole patterning. The PCE of the DSSC increased from 2% to 5.8% after applying the hole patterning approach. Al-Mamun *et al.*¹³⁵ deposited MoS_2 nano-scale thin films onto FTO substrates using a low temperature one-pot hydrazine assisted hydrothermal method. Both the hydrothermal reaction temperature as well as the different molar ratio of reaction precursors was found to impact the structure and performance of MoS_2 films used as CEs for DSSCs. The MoS_2 thin films having surface exposed layered nanosheets were obtained by the hydrothermal process with a molar ratio of reaction precursors as 1 : 28 of $(\text{NH}_4)_6\text{Mo}_7\text{O}_{24} \cdot 4\text{H}_2\text{O}$ and $\text{NH}_2\text{-CSNH}_2$ (thiourea) at 150 °C for 24 hours, referred to as MS-150-28. The molar ratio of $(\text{NH}_4)_6\text{Mo}_7\text{O}_{24} \cdot 4\text{H}_2\text{O}$ and NH_2CSNH_2 was fixed at 1 : 7, 1 : 14, 1 : 28 and 1 : 42 and the hydrothermal temperature was maintained at either 120, 150, 180 or 210 °C. The DSSCs having MoS_2 CEs fabricated using different molar ratios of reaction precursors at a temperature of 150 °C (referred to as MS-150-7, MS-150-14, MS-150-28 and MS-150-42) exhibited PCEs of 3.70, 4.97, 7.41 and 4.96%, respectively. The DSSCs with MS-120-28, MS-180-28, and MS-210-28 CEs showed PCEs of 5.52, 7.15 and 5.47%, respectively. The MoS_2 film based CEs showed a PCE of 7.41%, higher than the Pt electrode based DSSCs ($\eta = 7.13\%$) using TiO_2 photoanodes sensitized by N719 dye.

Pulse electrochemical deposited thin films of molybdenum sulfide (MoS_x) on indium tin oxide/poly(ethylene naphthalate) (ITO/PEN) substrates have been studied as flexible CEs for DSSC, and these showed a PCE of 4.39% for the triiodide (I_3^-) reduction.¹³⁶ The nanostructured MoS_2 thin films developed by a low-temperature thermally reduced technique on a FTO substrate have also been used for DSSCs.¹³⁷ MoS_2 thin film annealed at 300 °C were also used as CEs for DSSCs, which showed a PCE of 6.351%, slightly lower than the Pt reference CE ($\eta = 6.929\%$). The performance of DSSCs was impacted by the molar ratio of reaction precursors and the temperature of thermal reaction. Thermally reduced (TR) MoS_2 thin film annealed at 250 °C showed PCE of 1.917%, while those annealed at 350 °C showed PCE of 3.479%. The 300 °C annealed TR- MoS_2 CE also has larger exchange current density than those of 250 °C and 350 °C annealed TR- MoS_2 CEs and comparable with thermally deposited (TD) Pt CE. The R_{CT} values that correspond to the charge-transfer resistance at the electrolyte-electrode interface were 14.98 $\Omega \text{ cm}^2$ for TD-Pt CE and 30.98, 141.41 $\Omega \text{ cm}^2$ for TR- MoS_2 CEs annealed at 300 °C and 350 °C, respectively. TR- MoS_2 CEs annealed at 250 °C has no R_{CT} value being too large. The annealing temperature of 300 °C generates much larger active area, providing the highest electrocatalytic activity for the reduction of I_3^- , while 350 °C annealing decreases the active sites of the edge-planes in MoS_2 . A PCE of 7.01% was achieved for DSSCs using pristine MoS_2 as a CE, chemically synthesized by low-temperature wet-chemical process, which has a comparable PCE of 7.31% for DSSCs

with Pt CEs.¹³⁸ The R_s and R_{CT} values of 23.51 and 18.50 $\Omega \text{ cm}^2$, respectively, for the MoS_2 CE were lower than those of Pt CE (26.73 and 22.88 $\Omega \text{ cm}^2$), suggesting better electro-catalytic activity of MoS_2 for the reduction of triiodide (I_3^-).

A correlation between the electrical conductivity of the CE, PCE, and the crystallinity of MoS_2 was also demonstrated.¹³⁹ The XRD, XPS, EIS and Hall measurements established a link between the PCE, carrier concentration, mobility, and J_{sc} value. The DSSCs having pristine (non-annealed), vacuum-annealed and N_2 -annealed MoS_2 CEs showed PCE values of 1.0, 1.7 and 0.8%, respectively. Thermal annealing in vacuum was found to reduce the over-potential that leads to an increased J_{sc} value of 7.95 mA cm^{-2} due to high MoS_2 crystallinity, whereas the N_2 -annealing of MoS_2 CEs increases over-potential, which gives rise to lower J_{sc} value of 4.35 mA cm^{-2} due to the poor crystallinity of MoS_2 . Interestingly, the electrical conductivity of MoS_2 CEs follows the order: N_2 -annealed > vacuum-annealed > non-annealed MoS_2 . This indicates that the PCE of the DSSCs is influenced by the over-potential that involves an electron transferring from the MoS_2 CE to the electrolyte, instead of the electrical conductivity of the CE. Antonelou *et al.*¹⁴⁰ reported the growth of monolayer and few-layer MoS_2 films by the sulfidation of molybdenum (Mo) foils at 800 °C. The few-layer thick MoS_2 films were used as CEs for DSSCs for the reduction of I_3^- to I^- . The electrocatalytic activity of MoS_2 CE on flexible Mo substrates depends upon the number of monolayers in the DSSC. DSSCs having the MoS_2/Mo CE yield a PCE of 8.4%, close to Pt/FTO-based DSSCs (PCE of 8.7%). Stability of a three-monolayer thick MoS_2 CE was studied for 100 consecutive cycles, where no degradation of the peak current density was noticed for 100 repeated cycles, confirming long term electrochemical stability in an electrolyte solution. MoS_2 layers with 1–2 nm thickness showed long term chemical stability of the DSSC device for the electrolyte solution comparable to Pt CE. The increased number of active sites due to a grainy surface texture of Mo foil leads to the higher electro-catalytic activity of MoS_2 films.

A very interesting comparison was made by Wu *et al.*¹⁴¹ for chemically synthesized MoS_2 and WS_2 as CEs in the reduction of I_3^- to I^- and disulfide/thiolate (T_2/T^-) based DSSCs. The R_{CT} values of 0.5 $\Omega \text{ cm}^2$ for MoS_2 and 0.3 $\Omega \text{ cm}^2$ for WS_2 , respectively, compared with R_{CT} of 3.0 $\Omega \text{ cm}^2$ for Pt CE, indicates that both MoS_2 and WS_2 are as effective as CEs as standard Pt for triiodide (I_3^-) reduction in DSSCs. The high FFs of 73% for MoS_2 CEs and 70% for WS_2 CEs also confirm high electro-catalytic activities for the reduction of triiodide (I_3^-) to iodide (I^-). Therefore, high PCE values of 7.59% for MoS_2 and 7.73% for WS_2 were observed, which are comparable to the PCE of 7.64% for Pt CEs in DSSCs under simulated AM 1.5 illumination. The Z_N of $>100 \Omega$ for triiodide (I_3^-) reduction on the sulfide electrodes was found to be higher compared with a Z_N of 9.5 Ω on the Pt CE. The photocurrent density voltage ($J-V$) curves of the DSSCs having MoS_2 , WS_2 , and Pt based CEs for the triiodide/iodide (I_3^-/I^-) redox couple and disulfide/thiolate (T_2/T^-) redox couple are shown in (Fig. 5). The TiO_2 film photoanode was obtained after pre-heating at 80 °C and immersing in a $5 \times 10^{-4} \text{ M}$ solution of N719 dye in acetonitrile/tert-butyl alcohol for 20 hours. The



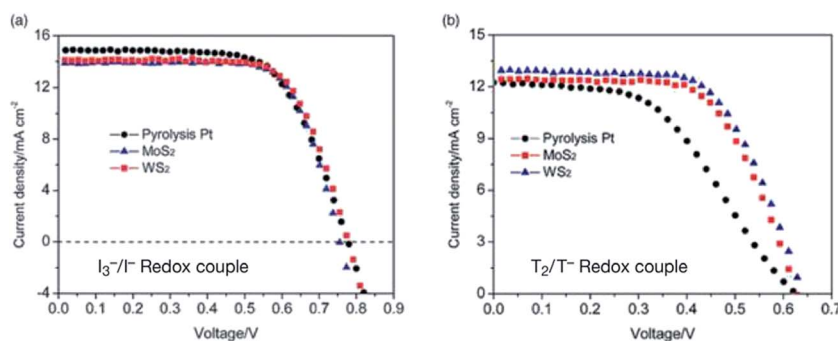


Fig. 5 (a) Photocurrent density–voltage (J – V) curves of the DSSCs having MoS₂, WS₂, and Pt counter electrodes for triiodide to iodide (I₃⁻/I⁻) reduction. (b) J – V curves of the DSSCs using MoS₂, WS₂ and Pt CEs for redox couple of disulfide/thiolate (T₂/T⁻). Reprinted with permission from ref. 141, M. Wu, Y. Wang, X. Lin, N. Yu, L. Wang, L. Wang, A. Hagfeldt and T. Ma, economical and effective sulfide catalysts for dye-sensitized solar cells as counter electrodes. *Phys. Chem. Chem. Phys.*, 2011, **13**, 19298–19301. Copyright© Royal Society of Chemistry/Owner Societies.

triiodide/iodide (I₃⁻/I⁻) electrolyte is made of 0.06 M of lithium iodide (LiI), 0.03 M of I₂, 0.5 M of 4-*tert*-butyl pyridine, 0.6 M of 1-butyl-3-methylimidazolium iodide, and 0.1 M of guanidinium thiocyanate in acetonitrile. The 5-mercaptop-1-methyltetrazole di-5-(1-methyltetrazole) disulfide/N-tetramethylammonium salt (NMe₄T⁻) (T₂/T⁻) electrolyte consists of 0.4 M of NMe₄T⁻, 0.05 M of LiClO₄, 0.4 M of di-5-(1-methyltetrazole) disulfide (T₂), and 0.5 M 4-*tert*-butylpyridine in acetonitrile and ethylene carbonate solution. For both DSSCs, a spray-coating technique was used for fabricating MoS₂ and WS₂ CEs. The J – V curves of the DSSCs having sulfide CEs and T₂/T⁻ electrolyte show PCE values of 4.97% for MoS₂, 5.24% for WS₂, and 3.70% for Pt CE. The PCE values were increased 36% for MoS₂ and 41% for WS₂ compared to the Pt CE, showing that DSSCs having MoS₂ and WS₂ are better than that of the Pt CE for the T₂/T⁻ redox couple.

The interfaced exfoliated MoS₂ thin films with different porphyrin molecules, where the MoS₂ was functionalized with zinc(II) porphyrin (ZnPP), showed a 10-fold increase in photocurrent compared to MoS₂ films.¹⁴² Exfoliated ultrathin porous MoS₂ sheets prepared by a tetraethylorthosilicate (TEOS)-assisted hydrothermal method were used as CEs in DSSCs.¹⁴³ The cyclic voltammograms and electrochemical impedance spectroscopy showed low R_{CT} and high electro-catalytic activity for porous MoS₂ sheets CEs in DSSCs, with a PCE of 6.35%, slightly better than that of Pt CEs ($\eta = 6.19\%$) under similar experimental conditions. A CE created by spin-coating of MoS₂ nanosheets followed by thermal treatment was also prepared.¹⁴⁴ DSSCs having MoS₂ nanosheets thermally treated at 100 °C showed a PCE value of 7.35%, comparable to conventional a Pt CE (7.53%). When MoS₂ nanosheets were thermally treated at 300 °C, the PCE value decreased significantly due to the transformation of MoS₂ to MoO₃. MoS₂ films deposited on FTO glass using an RF sputtering method were also used as CEs for TiO₂-based DSSCs.¹⁴⁵ CV, EIS, and Tafel polarization curve measurements conducted on the MoS₂ CE showed high electrocatalytic activity, low charge-transfer resistance as well as the fast reaction kinetics for triiodide (I₃⁻) reduction. The MoS₂ CE prepared after 5 minutes of sputtering showed a PCE of 6.0%, comparable to Pt CEs ($\eta = 6.6\%$) in DSSCs. The PCE of DSSCs having MoS₂ CEs sputtered for 1, 3, 5 and 7 minutes were 5.7,

5.8, 6.0, and 5.2%, respectively. MoS₂ CEs were also developed by synthesizing MoS₂ films at 70 °C using molybdenum(V) chloride and thioacetamide, followed by near-infrared laser-sintering for 1 minute to enhance crystallinity and inter-connectivity between the MoS₂ particles.¹⁴⁶ The DSSC with laser-sintered MoS₂ CE exhibited a PCE of 7.19%, much higher than heat-sintered MoS₂ CE (5.96%) and comparable with a Pt CE ($\eta = 7.42\%$). The laser-sintered MoS₂ CE offers superior electrocatalytic activity for the triiodide (I₃⁻) to iodide (I⁻) redox couple. Also, a solution-phase process was used to grow MoS₂ nanofilms on FTO glass as a CE for a DSSC, which showed a PCE of 8.3%.¹⁴⁷ Finally, exfoliated and annealed MoS₂Se₂(1-x) as well as exfoliated-MoS₂ films were used as CEs.¹⁴⁸ The thickness and size of exfoliated MoS₂ nanosheets were 0.9 by 1.2 nm and 0.2 by 2 μm, corresponding to a single-layer. The MoS₂ based CE showed a PCE of 6%, compared to 5.1% for the annealed MoS₂ films.

3.1.2 MoS₂/graphene composites. 2D TMDs based composites have been extensively investigated.^{149,150} Like graphene, MoS₂ can be mechanically exfoliated into nanosheets from its bulk crystals and used for studying electronics and photonic properties. These 2D layered materials can be combined into a single hybrid structure, so that both MoS₂ and graphene components can synergistically enhance photovoltaic properties. The nanocomposites of MoS₂ and graphene have been investigated as CEs for DSSCs.

To fabricate a Pt-free DSSC, Lin *et al.*¹⁵¹ used a MoS₂/graphene nanosheet composite as a CE and nanocrystalline TiO₂ as a photoanode. The redox electrolyte solution in the DSSC was made of 1 M 1,3-dimethylimidazolium iodide, 0.15 M iodine, 0.5 M 4-*tert*-butylpyridine and 0.1 M guanidine thiocyanate in 3-methoxypropionitrile. The MoS₂/graphene nanosheet based CE showed a PCE of 5.81%, in comparison to a PCE of 6.24% for the conventional sputtered Pt CE. Yue *et al.*¹⁵² used a MoS₂/graphene flake composite film as the CEs for DSSCs with N719 dye for the reduction of triiodide (I₃⁻) to iodide (I⁻). The MoS₂ powder (ARCOS, 99%) and 8 nm flakes of multi-layer graphene nanopowder (Uni-Onward Corp., 99.5%) were mixed in specific ratios to prepare the composites. The electrocatalytic activity increased after adding graphene flakes to the MoS₂ film.

Charge-transfer resistances (R_{CT}) of $3.98 \Omega \text{ cm}^2$ for graphene, $2.71 \Omega \text{ cm}^2$ for MoS_2 , $2.09 \Omega \text{ cm}^2$ for MoS_2 /graphene, and $2.01 \Omega \text{ cm}^2$ for Pt CEs were measured. The current density of the MoS_2 /graphene composite CE was recorded to be higher than that of the MoS_2 , graphene and Pt CEs. The J - V characteristics of the DSSCs having MoS_2 /graphene as CEs and ranging in thickness from single-layer to six-layer were investigated and compared with conventional Pt CEs. The thickness of the MoS_2 /graphene layers affected the PCE of the DSSCs, and J_{sc} and V_{oc} increased with increasing number of plaster layers from single to 3-layer, and, thereafter, a decrease was noticed for 4-layers and 5-layers. The effect of graphene content was also studied, where, the R_{CT} was found to decrease for the MoS_2 /graphene CE, from 0.5 wt% to 1.5 wt% of graphene content. The PCE of the MoS_2 /graphene composite CE having 1.5 wt% graphene was 5.98%, compared to the PCE of 6.23% for Pt CE. Yu *et al.*¹⁵³ used MoS_2 nanosheets and graphene composites for fabricating CEs for the triiodide (I_3^-) reduction. Graphene thin films were prepared by the chemical vapor deposition (CVD) technique in combination with a hydrothermal process. MoS_2 nanosheets with 210 nm thickness were *in situ* grown on FTO glass substrate, and uniformly dispersed on the surface of a graphene film. Fig. 6 shows the morphology of the synthesized graphene– MoS_2 composites, using field-emission scanning electron microscopy (FESEM) and high-resolution transmission electron microscopy (HRTEM) with different magnifications. The thickness of the graphene film was found to be 2.48 nm by atomic force

microscopy, which corresponds to seven layers of graphene. The top-view FESEM images of graphene– MoS_2 hybrids showed fully covered graphene film with 5 to 20 nm thick MoS_2 nanosheets. The nucleation and growth of MoS_2 nanosheets depends upon the graphene film. Graphene films play an active role for higher electrical conductivity by speeding up the charge transfer process and generating active sites for dispersion and integration of MoS_2 nanosheets. The presence of MoS_2 nanosheets increases the electrode–electrolyte contact area, and therefore helps in improving the electrocatalytic activity. The low R_{CT} of $1.5 \Omega \text{ cm}^2$ for MoS_2 /graphene CE, $1.7 \Omega \text{ cm}^2$ for MoS_2 , $1.70 \Omega \text{ cm}^2$ for graphene, and a high R_{CT} of $2.1 \Omega \text{ cm}^2$ for a Pt CE, indicates better interaction and contact formation of MoS_2 nanosheets and graphene film with fluorine doped tin oxide (FTO) substrates and a fast charge transfer. The FF of graphene is 24% compared to a FF of 65% for MoS_2 , however when both materials are combined into a composite system, the FF raises to 68%. Therefore, MoS_2 nanosheet/graphene composite CEs resulted in a higher PCE of 7.1% because of the synergistic interactions between graphene and MoS_2 , compared to the low PCE values of 2.8% for graphene and 5.6% for MoS_2 , and a comparable PCE of 7.4% for Pt reference CEs. MoS_2 /graphene based CEs in a DSSC offer higher electrocatalytic activity for triiodide (I_3^-) reduction induced by the synergistic interactions. Fig. 7 represents the J - V characteristics of DSSCs having graphene– MoS_2 as CEs with increasing number of layers¹⁵² and

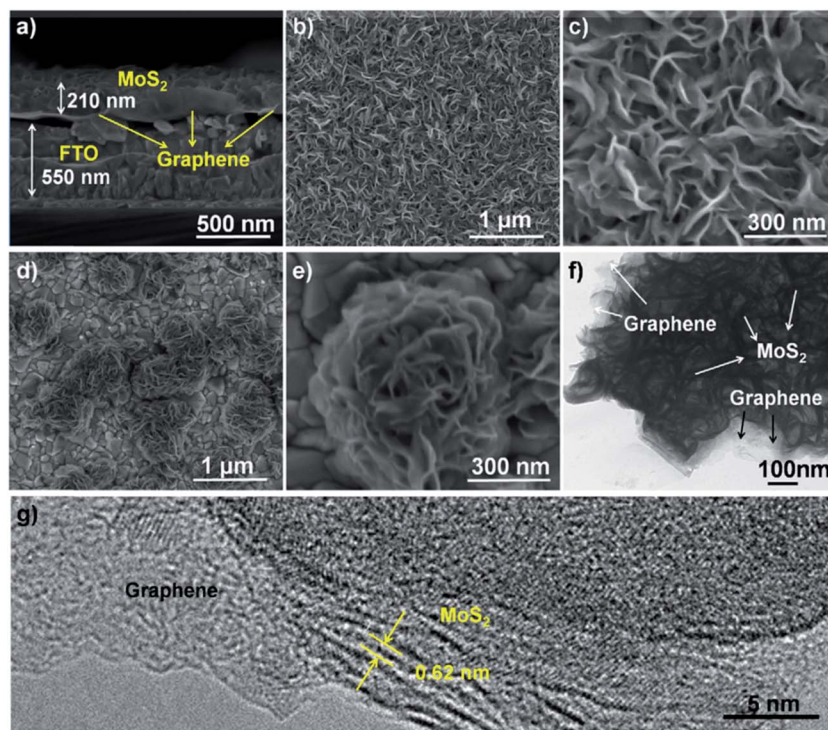


Fig. 6 Field-emission scanning electron microscopy (FESEM) images of graphene– MoS_2 composites with different magnifications; (a) side-view, (b) and (c) top-view. (d) and (e) top-view FESEM images of flower-like MoS_2 clusters without graphene film. (f) and (g) high-resolution transmission electron microscopy (HRTEM) images of as-prepared graphene– MoS_2 hybrids. Reprinted with permission from ref. 153, C. Yu, X. Meng, X. Song, S. Liang, Q. Dong, G. Wang, C. Hao, X. Yang, T. Ma, P. M. Ajayan and J. Qiu, graphene-mediated highly-dispersed MoS_2 nanosheets with enhanced triiodide reduction activity for dye-sensitized solar cells. *Carbon*, 2016, **100**, 474–483. Copyright© Elsevier.



graphene–MoS₂ nanosheet based CEs for the triiodide (I₃[–]) reduction.¹⁵³

MoS₂ nanosheets/graphene electrodes were also studied by Lynch *et al.*¹⁵⁴ the PCE of 95% of the Pt electrode was achieved after adding 10 wt% MoS₂ nanosheets to a graphene film CE. This again confirms that the MoS₂ nanosheet/graphene composite ECs have higher catalytic activity than graphene CEs, though the graphene nanosheets contribute to higher electrical conductivity in the composite. An electrochemical strategy¹⁵⁵ was used for preparing MoS₂/graphene composite as CEs of DSSCs, which included electro-deposition and electro-reduction of graphene oxide, and thereafter electro-deposition of MoS₂ on reduced graphene oxide (GO) layers. The MoS₂/graphene composites were characterized by SEM, TEM and Raman spectroscopy. The MoS₂/graphene CEs based DSSCs exhibited a PCE of 8.01%, comparable to a PCE of 8.21% for the Pt CE. In another study, nanocomposites of MoS₂ and nitrogen-doped graphene oxide (N–GO) were used as a CE for DSSCs.¹⁵⁶ The MoS₂/N–GO nanocomposites were characterized by HRTEM, XPS, and Raman spectroscopy, and their electrochemical properties were evaluated by EIS, CV, and Tafel measurements. The MoS₂/N–GO nanocomposite formation offered high specific surface area of N–GO and many edge sites of MoS₂. The MoS₂/N–GO nanocomposite based CE exhibited a PCE of 5.95%, lower than the standard Pt CE (PCE of 6.43%).

Composite films of MoS₂ with nitrogen-doped graphene (N-graphene) were prepared using a drop-coating method and used as a CE of DSSCs.¹⁵⁷ The N-graphene supported an increase in electrical conductivity, whereas MoS₂ increased the electrocatalytic activity in the composite thin film. The N-graphene/MoS₂ composite film showed a PCE of 7.82%, lower than the Pt CE ($\eta = 8.25\%$) based DSSC. The electrocatalytic capability of N-graphene/MoS₂ composite films for the triiodide (I₃[–]) reduction was much higher compared with pristine N-graphene and MoS₂ thin films, as studied using CV, RDE, the Tafel polarization curve, and EIS. The graphene flakes (GF) into a nanosheet-like MoS₂ matrix were dispersed using an *in situ* hydrothermal

method, and used a MoS₂/GF hybrid as a CE to fabricate Pt-free DSSCs.¹⁵⁸ The incorporation of GFs into the MoS₂ matrix was confirmed using scanning electron microscopy (SEM), transmission electron microscopy (TEM), XRD, and Raman spectroscopy. The electrochemical measurements showed improvement in the electrocatalytic activity after the GFs were integrated into the MoS₂ matrix, where the hybrid containing 1.5 wt% of graphene flakes exhibited the highest electrocatalytic activity. The DSSC with the MoS₂/GF hybrid CE showed a PCE of 6.07%, which was 95% of the Pt CE ($\eta = 6.41\%$).

3.1.3 MoS₂/carbon nanotubes composites. Carbon nanotubes (CNTs) are one of the most interesting materials because they offer high optical transparency, high electrical conductivity, high mechanical strength, and high thermal stability, and therefore CNTs have been studied as CEs for DSSCs. It is of great interest to combine the unique properties of both MoS₂ and CNTs into a single hybrid system which could synergistically enhance the electrocatalytic activity of a DSSC system. Yue *et al.*¹⁵⁹ used a flower-like structure of MoS₂/single-wall carbon nanotubes (MoS₂/SWCNTs) as CE catalyst for DSSCs, synthesized using a glucose and PEDOT:PSS assisted (G-P-A) hydrothermal process. The flower-like structure and surface morphology of the (G-P-A) MoS₂/SWCNTs was confirmed by SEM and TEM techniques. The DSSC having (G-P-A) MoS₂/SWCNTs CE exhibits a lower R_{CT} of 1.46 $\Omega \text{ cm}^2$ compared to the R_{CT} of 2.44 $\Omega \text{ cm}^2$ for the Pt electrode. The PCE reached 8.14%, better than that of the Pt-based DSSC (7.78%) with the iodide/triiodide (I₃[–]) electrolyte. The speedy reduction of triiodide (I₃[–]) to iodide (I[–]) by the (G-P-A) MoS₂/SWCNTs CE is attributed to the fast transport of the electrolyte *via* the flower-like structure. The MoS₂ and multi-walled carbon nanotube (MWCNTs) nanocomposites were employed as a CE in DSSCs for the reduction of triiodide (I₃[–]).¹⁶⁰ The microstructure of the MWCNTs@MoS₂ nanocomposite studied by transmission electron microscopy (TEM) confirmed the deposition of few-layers MoS₂ nanosheets on the MWCNTs surface. A MWCNTs@MoS₂ composite based CE resulted in higher

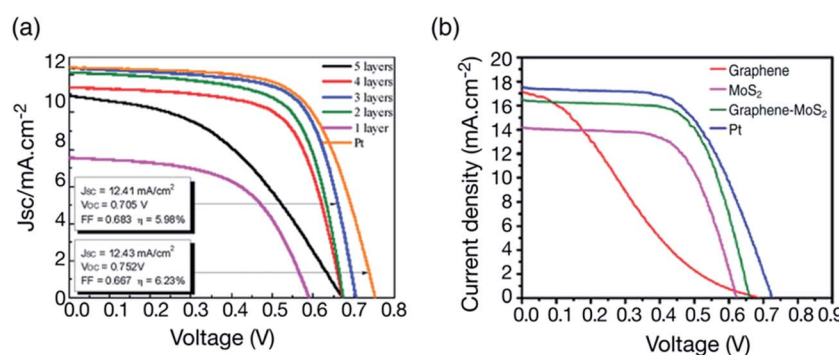


Fig. 7 (a) J–V characteristics of DSSCs having MoS₂/graphene as counter electrodes with different thickness ranging from single-layer to six-layer and a comparison with sputtered Pt counter electrode (PEC of 6.23%). Reprinted with permission from ref. 152, G. Yue, J. Y. Lin, S. Y. Tai, Y. Xiao and J. Wu, A catalytic composite film of MoS₂/graphene flake as a counter electrode for Pt-free dye-sensitized solar cells. *Electrochim. Acta*, 2012, **85**, 162–168. Copyright© Elsevier. (b) J–V curves of DSSCs based on Pt, graphene/MoS₂, MoS₂, and graphene CEs. Reprinted with permission from ref. 153, C. Yu, X. Meng, X. Song, S. Liang, Q. Dong, G. Wang, C. Hao, X. Yang, T. Ma, P. M. Ajayan and J. Qiu, graphene-mediated highly-dispersed MoS₂ nanosheets with enhanced triiodide reduction activity for dye-sensitized solar cells. *Carbon*, 2016, **100**, 474–483. Copyright© Elsevier.



cathodic current density than those of MWCNTs, MoS_2 , and Pt CEs. The MWCNTs@ MoS_2 CE showed a low charge-transfer resistance of $1.69 \Omega \text{ cm}^2$ and no degradation up to 100 repeated cyclic voltammogram tests. The DSSC having a MWCNTs@ MoS_2 composite CE exhibited a PCE of 6.45%, slightly better than that of the DSSC having sputtered Pt CE ($\eta = 6.41\%$). The MWCNT@ MoS_2 based CE also showed improved catalytic activity for the reduction of I_3^- .

The MoS_2 nanosheets anchored onto the CNT surfaces were used in Pt-free CEs for DSSCs.¹⁶¹ The MoS_2 nanosheets offer edge-plane electrocatalytically active sites for the reduction of I_3^- . The large surface area of CNTs supports the loading of MoS_2 nanosheets in order to increase the electrochemical activity. The CNTs deposited onto the FTO substrate promoted charge transport, leading to a higher exchange current density and also to the lower charge-transfer resistance. The MoS_2 /CNT hybrid based DSSCs achieved a PCE of 7.83%, which is 9.5% higher than that of the Pt CE ($\eta = 7.15\%$) based DSSC.

Another research group¹⁶² used flower-like MoS_2 and a multi-walled carbon nanotubes (MoS_2 /MWCNTs) hybrid as a CE for dye-sensitized solar cells. The flower-like MoS_2 /MWCNTs hybrid contains a large specific surface area and lamellar structure, as evidenced by field emission scanning electron microscopy (FESEM). The optimized MoS_2 /MWCNTs has a R_{CT} of $2.05 \Omega \text{ cm}^2$ and series resistance (R_s) of $1.13 \Omega \text{ cm}^2$ as measured by electrochemical impedance spectroscopy. Cyclic voltammogram measurements showed larger current density for MoS_2 /MWCNTs based CEs than those of MoS_2 , MWCNTs, and Pt CEs.

MoS_2 /MWCNTs CE based DSSCs exhibited a PCE of 7.50%, comparable with the DSSC based on the Pt CE ($\eta = 7.49\%$). A carbon nanotubes- MoS_2 -carbon (CNTs- MoS_2 -carbon) hybrid was prepared using wet impregnation and calcination with polyethylene glycol as a CE for DSSCs.¹⁶³ Spectroscopic characterization by Raman spectra, XRD, TEM, XPS, BET and thermal methods indicated a homogenous coating of CNTs with thin layers of MoS_2 , as a result of wetting and emulsification of polyethylene glycol 400. The CNTs- MoS_2 -carbon heterostructure was used as CEs for DSSCs, and showed high stability and electrocatalytic activity in the reduction of I_3^- to I^- because of low R_{CT} . Interestingly, a PCE of 7.23% achieved for the CNTs- MoS_2 -carbon CEs based DSSC was higher than Pt CEs ($\eta = 6.19\%$).

In another study, nanocomposites of MoS_2 and CNTs using a glucose aided (G-A) hydrothermal method were prepared by Yue *et al.*¹⁶⁴ The (G-A) MoS_2 /CNTs nanocomposites obtained by adding 0.5, 1.0, 1.5, 2.0 and 2.5 wt% of acid-treated CNTs were deposited onto a FTO substrate and used as CEs in DSSCs for the reduction of triiodide (I_3^-) to iodide (I^-). The dye-sensitized TiO_2 anode was prepared by dipping the TiO_2 anode in 0.3 mM of dye N719 ethanol for 24 hours. Fig. 8 shows the SEM images of MoS_2 nanopowder and MoS_2 -MWCNTs composites, *J-V* characteristics of the DSSCs fabricated with MoS_2 , MoS_2 /C, (G-A) MoS_2 /CNTs and Pt CEs, and the effect of CNT contents on the PCE of the DSSCs using (G-A) MoS_2 /CNTs. Scanning and transmission electron microscopy showed tentacle-like structures of the MoS_2 /CNTs composites, having large active surface area and

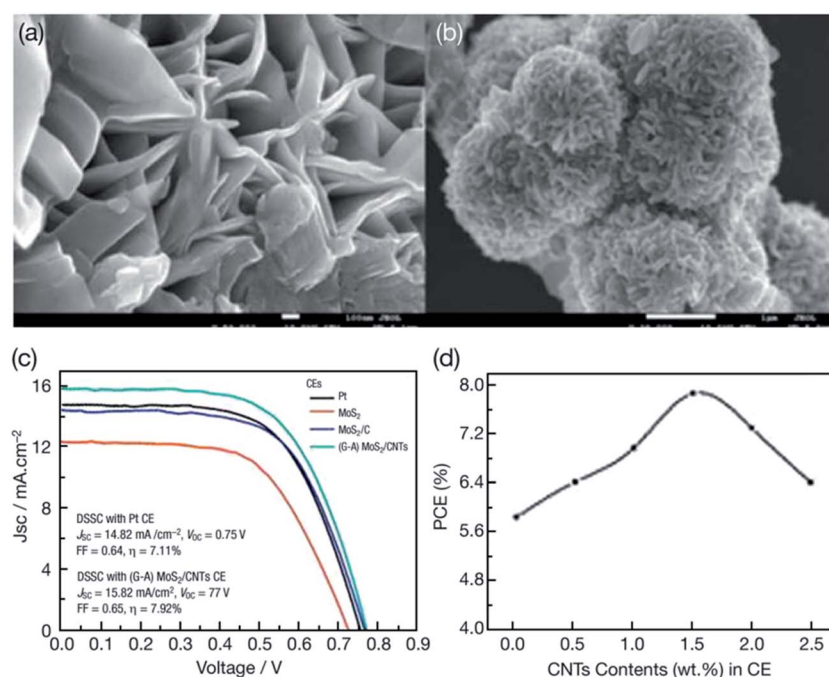


Fig. 8 Scanning electron microscopic image of MoS_2 nanopowder and MoS_2 -MWCNTs composites prepared by glucose aided (G-A) hydrothermal method. Photocurrent-voltage (*J-V*) characteristics of the DSSCs fabricated with MoS_2 , MoS_2 /C, (G-A) MoS_2 /CNTs and Pt CEs. Relationship between the contents of CNTs in (G-A) MoS_2 /CNTs CE and the PCE of DSSCs. Reprinted with permission from ref. 164, G. Yue, W. Zhang, J. Wu and Q. Jiang, glucose aided synthesis of molybdenum sulfide/carbon nanotubes composites as counter electrode for high performance dye-sensitized solar cells. *Electrochim. Acta*, 2013, **112**, 655–662. Copyright© Elsevier.



interconnected networks for fast transport for the electrolyte. The CNTs functionalized with a $-COOH$ functional group were used and MoS_2 was anchored onto the functionalized CNTs. The (G-A) MoS_2 /CNTs had specific surface area of $411.7\text{ m}^2\text{ g}^{-1}$ and exhibited a small overpotential and better conductivity. The Nernst diffusion impedance (Z_w) values of $1.85\text{ }\Omega\text{ cm}^2$ for (G-A) MoS_2 /CNTs CEs and $2.25\text{ }\Omega\text{ cm}^2$ for Pt CEs were measured, which indicates that the (G-A) MoS_2 /CNTs catalyst accelerated the reduction of triiodide ions (I_3^-) to iodide ions (I^-). The (G-A) MoS_2 /CNTs based CEs were found to exhibit enhanced electrocatalytic activity as evidenced by the CV, EIS, and Tafel polarization measurements. The photovoltaic performance of the DSSCs having MoS_2 , MoS_2/C , (G-A) MoS_2 /CNTs, and Pt CEs were compared. The photovoltaic performance of (G-A) MoS_2 /CNTs CEs were also studied as a function of the CNT contents. The PCE of the DSSCs increased as the contents of the CNTs increased from 0 to 1.5 wt%, however, further increase in CNT content leads to a decreased PCE. Likely, the maximum photovoltaic performance of the (G-A) MoS_2 /CNTs CE in the DSSCs was achieved for a film thickness of $12\text{ }\mu\text{m}$. The (G-A) MoS_2 /CNTs composite CE has a lower R_{CT} of $1.77\text{ }\Omega\text{ cm}^2$ at the electrolyte/electrode interface than those of MoS_2 , MoS_2 /carbon and conventional sputtered Pt CEs, and a PCE of 7.92% higher than the PCE of 7.11% for the Pt electrode in DSSCs for the triiodide/iodide (I_3^-/I^-) system. Lin *et al.*¹⁶⁵ fabricated nanocomposites of MoS_2 /reduced graphene oxide (RGO) with CNTs using electrophoretic deposition. The MoS_2 /RGO-CNTs hybrid was then used as a CE in DSSCs. In this hybrid, CNTs offer conductive networks for electron transport to increase the rate of charge-transfer at the CE/electrolyte interface. The MoS_2 /RGO-CNTs hybrid CEs show improved electrocatalytic activity

in comparison with the MoS_2 /RGO alone. The DSSC having a MoS_2 /RGO-CNTs hybrid CE achieved a PCE of 7.46%, exceeding PCE values of DSSCs containing MoS_2 /RGO CE ($\eta = 6.82\%$) and Pt CE ($\eta = 7.23\%$). Thin films of MoS_2 /carbon nanotube composites have also been applied as electrodes for lithium ion batteries.¹⁶⁶

3.1.4 MoS_2/TiO_2 composites. MoS_2/TiO_2 heterostructures were developed by Du *et al.*¹⁶⁷ by depositing few-layer MoS_2 on mesoporous TiO_2 by a chemical-bath method. Raman spectrum and HRTEM images indicated a few-layer structure of the MoS_2 . After few-layer MoS_2 deposition, the UV absorption spectra of the TiO_2 photoanode showed enhanced absorption in the visible wavelength region and a PCE of 1.08% for the MoS_2/TiO_2 based DSSC. Photovoltaic performance of the DSSC was found to be optimized by both thermal annealing and the thickness of the MoS_2 sensitized layer. Jhang *et al.*¹⁶⁸ modified the interface of a MoS_2 CE/electrolyte by incorporating TiO_2 nanoparticles, in order to control the overpotential loss. Their MoS_2/TiO_2 nanocomposite had a weight ratio of 5 : 1. Thermal annealing of the MoS_2 and MoS_2/TiO_2 CEs was performed at $400\text{ }^\circ\text{C}$ in vacuum for 2 hours. Fig. 9 shows the J - V curves for MoS_2 , MoS_2/TiO_2 , and Pt CEs in the DSSCs. The addition of TiO_2 nanoparticles into the MoS_2 CE significantly increased the J_{sc} value from 7.24 mA cm^{-2} for the MoS_2 CE to 13.76 mA cm^{-2} for the MoS_2/TiO_2 CE. The MoS_2/TiO_2 CE based DSSC ($\eta = 5.08\%$) shows two times better photovoltaic performance compared with the MoS_2 CE (2.54%) and comparable to the Pt CE (5.27%), because of an increased active surface area from the incorporated TiO_2 nanoparticles and the low overpotential loss. Though the MoS_2/TiO_2 CE exhibited high PCE, its electrical conductivity was found to be lower compared to the MoS_2 CE, and, therefore, the high electrocatalytic activity was not related to its electrical conductivity.

The MoS_2/TiO_2 based CE doped with different Co contents for the DSSCs were found to influence the PCE by improving electrocatalytic activity.¹⁶⁹ The Co content-optimized MoS_2/TiO_2 CE had enhanced catalytic activity at the electrolyte interfaces. The Co 3d orbit plays a role in increasing in the reduction of I_3^- to I^- . The photoanodes were developed using MoS_2 and TiO_2 nanoparticles.¹⁷⁰ The DSSCs with $MoS_2@TiO_2$ photoanode showed a PCE of 6.02%, 1.5 times higher than that of the TiO_2 film photoanode ($\eta = 4.43\%$).

3.1.5 MoS_2 /carbon composites. A very interesting study on MoS_2 /carbon composites was conducted by Yue *et al.*¹⁷¹ who developed DSSCs using MoS_2 and carbon composites as a CE with different contents of carbon. Fig. 10 represents the SEM images of hydrothermally synthesized MoS_2 and a porous MoS_2 -carbon hybrid, a HRTEM image of MoS_2 -carbon hybrid, an IPCE spectra, and J - V curves of the DSSCs with MoS_2 , MoS_2 -carbon hybrid, and Pt CEs. The commercial MoS_2 particles have lamellar structure with large surface area. The hydrothermally prepared MoS_2 and MoS_2 -carbon hybrid contains a large number of interlaced nanosheets. The intercalated nanosheets in the MoS_2 -carbon hybrid are thinner compared with MoS_2 , indicating an increase in the specific surface area, which is highly suitable for improving the electrocatalytic activity. The MoS_2 and MoS_2 -carbon hybrid CEs were characterized by CV,

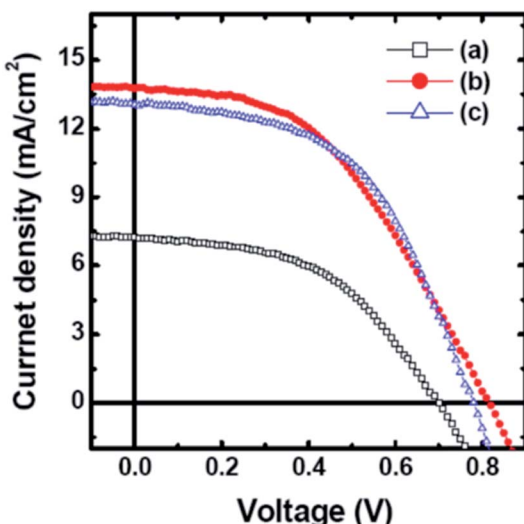


Fig. 9 Photocurrent density–voltage (J – V) characteristics curves of DSSCs with (a) MoS_2 , (b) MoS_2/TiO_2 and (c) Pt counter electrodes measured under the solar light illumination of 100 mW cm^{-2} (AM 1.5G). Reprinted with permission from ref. 168, W. H. Jhang and Y. J. Lin, interface modification of MoS_2 counter electrode/electrolyte in dye-sensitized solar cells by incorporating TiO_2 nanoparticles. *Curr. Appl. Phys.*, 2015, 15, 906–909. Copyright © Elsevier.



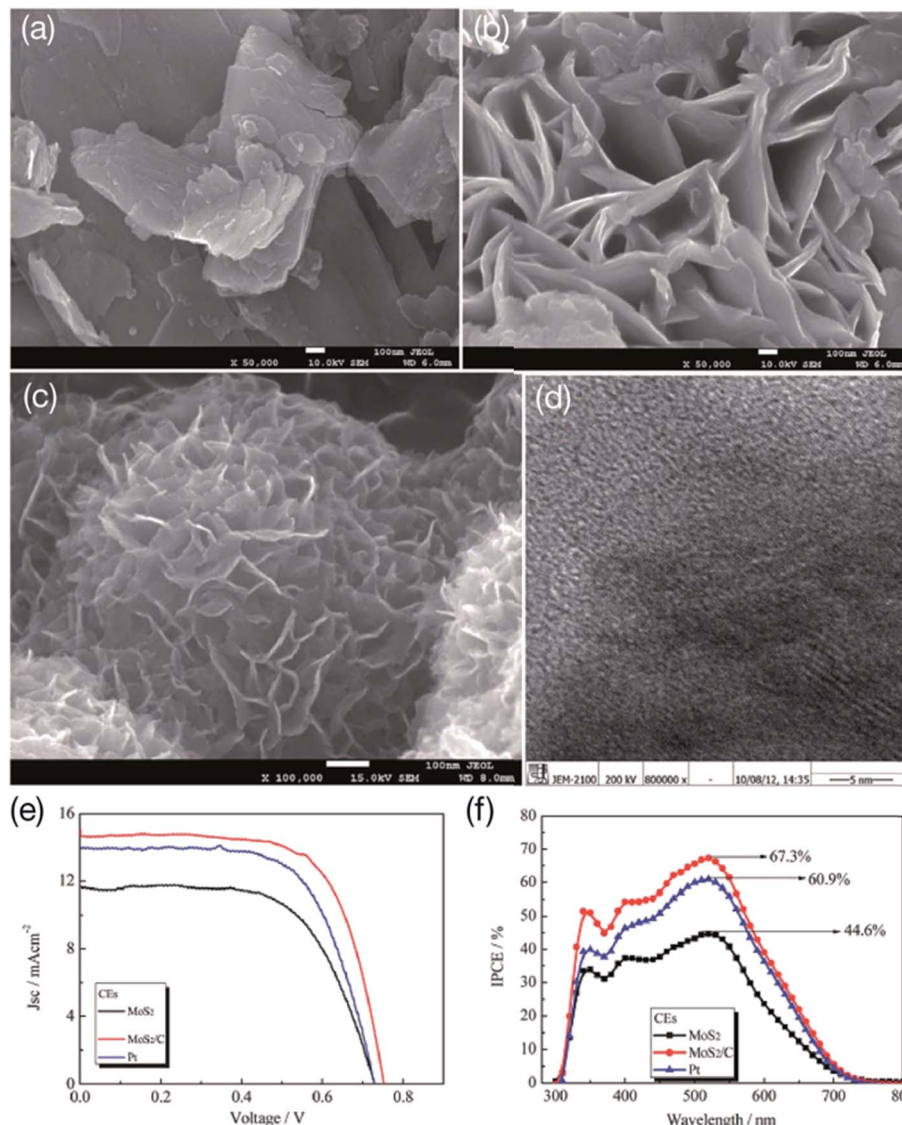


Fig. 10 Scanning electron microscopy (SEM) images of (a) commercial MoS₂, (b) hydrothermal route synthesized MoS₂, (c) porous MoS₂–carbon hybrid prepared by a hydrothermal route, (d) high-resolution TEM image of MoS₂–carbon hybrid, (e) photocurrent–voltage (J – V) curves of the DSSCs with MoS₂, MoS₂–C and Pt CEs and (f) incident photon-to-current efficiency (IPCE) spectra of the DSSCs with MoS₂, MoS₂–C and Pt CEs. Reprinted with permission from ref. 171, G. Yue, J. Wu, Y. Xiao, M. Huang, J. Lin and J. Y. Lin, high performance platinum-free counter electrode of molybdenum sulfide–carbon used in dye-sensitized solar cells. *J. Mater. Chem. A*, 2013, 1, 1495–1501. Copyright © Royal Society of Chemistry.

EIS, and Tafel polarization curve measurements, and compared with the Pt CE. IPCE spectra of MoS₂, MoS₂–C, and Pt CEs in DSSCs measured in the 300–750 nm range show a similar photoelectric response. A strong photoelectric peak in the IPCE spectra appears at 340 nm. DSSCs with MoS₂ CE show the highest photoelectric response of 44.6% in the IPCE spectra at 520 nm, which is lower compared to a DSSC having a Pt CE (60.9%). Interestingly, in the IPCE spectra of the DSSC having porous MoS₂–carbon CE, the highest photoelectric response of 67.3% is observed at 520 nm, which is higher than that of the Pt CE based DSSC. If one compares the R_{CT} values of 4.13 Ω cm² for MoS₂ and 2.29 Ω cm² for Pt electrodes, the MoS₂/carbon electrode had a low R_{CT} value of 2.07 Ω cm², appearing as a result of the high conductivity and large surface area for the MoS₂/

carbon composite, which eventually contributes to enhanced electrocatalytic activity of the CE. The R_{CT} values of the MoS₂/carbon electrode are also influenced by the carbon content, which decreases with the increase in carbon content, from 3.60 Ω cm² for 1.13 wt% carbon to 2.07 Ω cm² for 3.30 wt% carbon. Thereafter, the R_{CT} values increased from 2.40 Ω cm² for 4.35 wt% carbon content to 3.13 Ω cm² for 5.38 wt% carbon content. PCE values of 6.01, 7.03, 7.69, 7.33 and 5.76% were measured for MoS₂–carbon electrodes having 1.13, 2.23, 3.30, 4.35 and 5.38 wt% of carbon content, respectively. The highest value of 7.69% was achieved at 3.30 wt% carbon content in a MoS₂/carbon composite CE based DSSC for the I^-/I_3^- redox reaction, and exceeded the PCE value of 6.74% for a Pt CE under similar experimental conditions. PCE values of the DSSCs were also

Table 2 Photovoltaic parameters of MoS_2 based counter electrodes (CEs) used for DSSCs. FTO glass is the common substrate used in assembling DSSCs with different CE materials. The measurements were conducted at a simulated solar light intensity of 100 mW cm^{-2} (AM 1.5G) unless specified. The photovoltaic parameters short-circuit photocurrent density (J_{sc}), open-circuit voltage (V_{oc}), fill factor (FF), power conversion efficiency (η), series resistance (R_s), charge-transfer resistance (R_{CT}), electrolyte and dye used of DSSCs of graphene/ MoS_2 nano-composites are summarized and compared with standard Pt counter electrode^a

Counter electrodes	Redox couple	Dye	J_{sc} (mA cm^{-2})	V_{oc} (V)	FF (%)	PCE (η , %)	R_s ($\Omega \text{ cm}^2$)	R_{CT} ($\Omega \text{ cm}^2$)	Ref.
2H- MoS_2 (hydrothermal, 200 °C)	I^-/I_3^-	N719	6.78	0.73	35	1.72	16	49	130
1T- MoS_2 (hydrothermal, 180 °C)	I^-/I_3^-	N719	8.76	0.73	52	7.08	16	19	130
Pt reference	I^-/I_3^-	N719	17.75	0.702	58	7.25	—	—	130
MoS_2 (CVD) vertically inclined	I^-/I_3^-	N719	15.2	0.707	69.7	7.50	9.5	3.10	131
Pt reference	I^-/I_3^-	N719	14.6	0.712	70.0	7.28	6.7	5.36	131
MoS_2 /graphite	I^-/I_3^-	N719	15.64	0.685	67	7.18	—	8.05	132
Graphite	I^-/I_3^-	N719	11.62	0.445	63	3.26	—	15.70	132
Pt reference	I^-/I_3^-	N719	15.84	0.735	65	7.57	—	6.35	132
MoS_2 (multi-layer)	I^-/I_3^-	N719	15.81	0.745	25	2.92	27.3	186.2	133
MoS_2 (few-layer)	I^-/I_3^-	N719	14.90	0.744	16	1.74	35.8	281.2	133
MoS_2 (nanoparticle)	I^-/I_3^-	N719	14.72	0.745	49	5.41	26.9	93.0	133
Pt reference	I^-/I_3^-	N719	13.41	0.754	65	6.58	34.2	3.9	133
MoS_2 (hydrothermal method)	I^-/I_3^-	N719	18.37	0.698	57.8	7.41	—	0.619	135
Pt reference	I^-/I_3^-	N719	16.78	0.722	58.8	7.13	—	3.78	135
MoS_2 (300 °C annealed)	I^-/I_3^-	N719	16.905	0.727	51.7	6.351	23.89	30.98	137
Pt reference	I^-/I_3^-	N719	17.056	0.724	55.7	6.929	27.17	14.98	137
MoS_2 (chemical deposition)	I^-/I_3^-	N719	18.46	0.68	58	7.01	23.51	18.50	138
Pt reference	I^-/I_3^-	N719	16.80	0.71	60	7.31	26.73	22.88	138
MoS_2 (non-annealed)	I^-/I_3^-	N719	5.24	0.74	27	1.0	28	—	139
MoS_2 (vacuum-annealed)	I^-/I_3^-	N719	7.95	0.74	29	1.7	22	—	139
MoS_2 (N_2 -annealed)	I^-/I_3^-	N719	4.35	0.67	27	0.8	44	—	139
MoS_2/Mo (<i>in situ</i> sulfurization)	I^-/I_3^-	N719	22.6	0.74	50	8.4	—	—	140
Pt reference	I^-/I_3^-	N719	21.9	0.735	53.4	8.7	—	—	140
MoS_2 (hydrothermal method)	I^-/I_3^-	N719	13.84	0.76	73	7.59	20.8	0.5	141
WS_2 (hydrothermal method)	I^-/I_3^-	N719	14.13	0.78	70	7.73	19.4	0.3	141
Pt reference	I^-/I_3^-	N719	14.89	0.78	66	7.64	12.7	3.0	141
MoS_2 (hydrothermal method)	T_2/T^-	N719	12.52	0.63	63	4.97	—	—	141
WS_2 (hydrothermal method)	T_2/T^-	N719	12.99	0.64	64	5.24	—	—	141
Pt reference	T_2/T^-	N719	12.23	0.63	48	3.70	—	—	141
MoS_2 (porous sheets)	I^-/I_3^-	N719	15.40	0.763	53	6.35	7.95	1.73	143
MoS_2 (flower-shaped)	I^-/I_3^-	N719	13.73	0.700	52	5.23	7.89	2.67	143
Pt reference	I^-/I_3^-	N719	16.34	0.745	51	6.19	8.06	1.82	143
MoS_2 (sputtering, 5 min)	I^-/I_3^-	N719	13.17	0.71	64	6.6	30.1	2.2	145
Pt reference	I^-/I_3^-	N719	14.70	0.71	66	6.0	3.1	1.5	145
MoS_2 (as-prepared)	I^-/I_3^-	N719	11.92	0.656	35	2.74	—	1.01×10^4	146
MoS_2 (heat-sintered)	I^-/I_3^-	N719	13.01	0.705	65	5.96	—	18.50	146
MoS_2 (laser-sintered)	I^-/I_3^-	N719	14.94	0.718	67	7.19	—	15.29	146
Pt reference	I^-/I_3^-	N719	14.30	0.741	70	7.42	—	3.99	146
MoS_2 (growth time, 5 h)	I^-/I_3^-	N719	15.15	0.76	52	5.96	50.9	118.8	147
MoS_2 (growth time, 10 h)	I^-/I_3^-	N719	15.94	0.71	63	7.14	50.4	21.2	147
MoS_2 (growth time, 15 h)	I^-/I_3^-	N719	16.96	0.74	66	8.28	38.8	12.9	147
Pt reference	I^-/I_3^-	N719	13.77	0.74	74	7.53	36.3	13.1	147
MoS_2 (exfoliated)	I^-/I_3^-	N719	11.54	0.80	65	6.0	29.60	19.60	148
MoS_2 (annealed)	I^-/I_3^-	N719	10.92	0.80	58	5.1	28.10	121.10	148
Pt reference	I^-/I_3^-	N719	—	—	—	—	—	—	148
MoS_2	I^-/I_3^-	N719	12.92	0.701	46	4.15	11.69	3.65	151
Graphene nanosheet	I^-/I_3^-	N719	11.99	0.754	30	2.68	9.31	6.24	151
MoS_2 -graphene nanosheet	I^-/I_3^-	N719	12.79	0.773	59	5.81	9.52	2.34	151
Pt reference	I^-/I_3^-	N719	13.12	0.763	62	6.24	9.11	1.79	151
MoS_2 /graphene	I^-/I_3^-	N719	12.41	0.71	68	5.98	24.42	4.94	152
Pt reference	I^-/I_3^-	N719	12.43	0.73	67	6.23	24.72	4.74	152
MoS_2 (CVD)	I^-/I_3^-	N719	14.0	0.62	65	5.6	1.5	2.3	153
MoS_2 /graphene (CVD)	I^-/I_3^-	N719	16.1	0.66	67	7.1	1.7	1.6	153
Graphene	I^-/I_3^-	N719	16.9	0.68	24	2.8	1.7	2.8	153
Pt reference	I^-/I_3^-	N719	17.2	0.72	60	7.4	2.1	1.8	153
MoS_2	I^-/I_3^-	N719	9.14	0.589	47	2.53	—	—	154
Graphene	I^-/I_3^-	N719	10.7	0.652	51.9	3.62	—	—	154
MoS_2 : graphene (10 : 90)	I^-/I_3^-	N719	11.91	0.646	56.5	4.35	—	—	154
Pt reference	I^-/I_3^-	N719	13.39	0.657	50	4.40	—	—	154



Table 2 (Contd.)

Counter electrodes	Redox couple	Dye	J_{sc} (mA cm $^{-2}$)	V_{oc} (V)	FF (%)	PCE (η , %)	R_s (Ω cm 2)	R_{CT} (Ω cm 2)	Ref.
MoS ₂ /graphene oxide (N ₂ doped)	I ⁻ /I ₃ ⁻	N719	15.98	0.70	53	5.95	25.7	5.4	156
Graphene oxide (N ₂ doped)	I ⁻ /I ₃ ⁻	N719	14.66	0.71	38	3.95	25.7	21.3	156
MoS ₂	I ⁻ /I ₃ ⁻	N719	15.39	0.69	39	4.09	26.0	10.1	156
Pt reference	I ⁻ /I ₃ ⁻	N719	16.14	0.70	57	6.43	26.3	4.3	156
MoS ₂ (drop-coating)	I ⁻ /I ₃ ⁻	N719	13.46	0.79	58	6.20	21.14	24.93	157
Nitrogen-doped graphene (NGr)	I ⁻ /I ₃ ⁻	N719	12.72	0.68	64	5.50	16.31	30.17	157
MoS ₂ /NGr (8 wt%)	I ⁻ /I ₃ ⁻	N719	15.36	0.77	66	7.82	15.60	16.73	157
Pt reference	I ⁻ /I ₃ ⁻	N719	15.71	0.77	68	8.25	15.23	10.15	157
MoS ₂	I ⁻ /I ₃ ⁻	N719	10.56	0.67	58	4.10	—	—	158
Graphene flake (GF)	I ⁻ /I ₃ ⁻	N719	10.96	0.69	48	3.63	—	—	158
MoS ₂ (GF is 0.5 wt%)	I ⁻ /I ₃ ⁻	N719	12.09	0.69	59	4.85	—	—	158
MoS ₂ (GF is 1 wt%)	I ⁻ /I ₃ ⁻	N719	12.68	0.74	59	5.35	—	—	158
MoS ₂ (GF is 1.5 wt%)	I ⁻ /I ₃ ⁻	N719	13.27	0.75	61	6.07	—	—	158
MoS ₂ (GF is 2 wt%)	I ⁻ /I ₃ ⁻	N719	12.95	0.74	58	5.56	—	—	158
MoS ₂ (GF is 2.5 wt%)	I ⁻ /I ₃ ⁻	N719	12.63	0.70	58	5.04	—	—	158
Pt reference	I ⁻ /I ₃ ⁻	N719	12.95	0.75	66	6.41	—	—	158
MoS ₂	I ⁻ /I ₃ ⁻	N719	11.25	0.72	61	4.99	11.37	2.43	160
Multi-walled CNT (MWCNT)	I ⁻ /I ₃ ⁻	N719	9.11	0.65	58	3.53	9.91	8.59	160
MoS ₂ /MWCNT	I ⁻ /I ₃ ⁻	N719	13.69	0.73	65	6.45	10.22	1.69	160
Pt reference	I ⁻ /I ₃ ⁻	N719	13.24	0.74	66	6.41	9.06	1.91	160
MoS ₂	I ⁻ /I ₃ ⁻	N719	14.44	0.74	64	6.81	—	—	161
Carbon nanotubes	I ⁻ /I ₃ ⁻	N719	13.33	0.75	62	6.15	—	—	161
MoS ₂ /carbon nanotubes	I ⁻ /I ₃ ⁻	N719	16.65	0.74	66	7.83	—	—	161
Pt reference	I ⁻ /I ₃ ⁻	N719	14.83	0.74	65	7.15	—	—	161
MoS ₂ /CNTs	I ⁻ /I ₃ ⁻	N719	14.93	0.65	47	4.51	8.42	4.35	163
CNTs/MoS ₂ /carbon	I ⁻ /I ₃ ⁻	N719	16.44	0.79	57	7.23	8.14	1.73	163
Pt reference	I ⁻ /I ₃ ⁻	N719	15.40	0.75	55	6.19	8.31	1.95	163
MoS ₂ /CNTs (G-A)	I ⁻ /I ₃ ⁻	N719	15.82	0.77	65	7.92	5.20	1.77	164
MoS ₂ /carbon	I ⁻ /I ₃ ⁻	N719	14.52	0.76	64	7.06	5.24	2.35	164
MoS ₂	I ⁻ /I ₃ ⁻	N719	12.33	0.72	61	5.42	5.33	4.16	164
Pt reference	I ⁻ /I ₃ ⁻	N719	14.82	0.75	64	7.11	5.06	2.22	164
MoS ₂ /reduced graphene oxide (RGO)	I ⁻ /I ₃ ⁻	N719	14.31	0.76	63	6.82	20.58	4.42	165
MoS ₂ /RGO-CNTs	I ⁻ /I ₃ ⁻	N719	14.59	0.76	67	7.46	20.37	3.31	165
Pt reference	I ⁻ /I ₃ ⁻	N719	14.53	0.77	65	7.23	20.13	4.06	165
MoS ₂ (spin-coating)	I ⁻ /I ₃ ⁻	N719	7.24	0.70	49	2.54	59.5	—	168
MoS ₂ /TiO ₂ (5 : 1 wt ratio)	I ⁻ /I ₃ ⁻	N719	13.76	0.82	45	5.08	56.5	—	168
Pt reference	I ⁻ /I ₃ ⁻	N719	13.06	0.78	52	5.27	—	—	168
MoS ₂ /TiO ₂	I ⁻ /I ₃ ⁻	N719	4.67	0.68	44	1.4	—	—	169
MoS ₂ /TiO ₂ /Co	I ⁻ /I ₃ ⁻	N719	9.21	0.70	50	3.2	—	—	169
MoS ₂ /carbon (C is 2.23 wt%)	I ⁻ /I ₃ ⁻	N719	13.98	0.74	68	7.03	5.87	2.67	171
MoS ₂ /carbon (C is 3.30 wt%)	I ⁻ /I ₃ ⁻	N719	15.07	0.75	68	7.69	5.77	2.07	171
MoS ₂ /carbon (C is 4.35 wt%)	I ⁻ /I ₃ ⁻	N719	14.37	0.75	68	7.33	5.83	2.40	171
MoS ₂	I ⁻ /I ₃ ⁻	N719	11.66	0.73	63	5.36	5.87	4.13	171
Pt reference	I ⁻ /I ₃ ⁻	N719	13.98	0.73	66	6.74	5.79	2.29	171
MoS ₂ /PEDOT-PSS	I ⁻ /I ₃ ⁻	N719	14.55	0.68	58	5.7	—	—	174
PEDOT-PSS	I ⁻ /I ₃ ⁻	N719	14.6	0.68	26	2.5	—	—	174
Pt reference	I ⁻ /I ₃ ⁻	N719	15.26	0.73	59	6.6	—	—	174

^a Disulfide/thiolate (T₂/T⁻) redox couple. In the case of R_s and R_{CT} : some of the authors used Ω instead of Ω cm 2 for the resistances without mentioning the size of the electrode.

found to vary as a function of the thickness of MoS₂/carbon CE. PCE values of 5.10, 6.89, 7.69, 7.01 and 4.85% were measured for the CE thicknesses of 4, 8, 12, 16 and 20 μ m for the MoS₂/carbon CE. EIS, CV, and Tafel curve analysis showed low R_{CT} , high electrocatalytic activity, and faster reduction of triiodide (I₃⁻) to iodide (I⁻) for the MoS₂/carbon CE compared to that of the Pt CE.

In yet another study, MoS₂/carbon fibers were used as CEs for DSSCs.¹⁷² Both electrocatalytic activity and the PCE (3.26%) of

the MoS₂/carbon fiber based CE was found to be better than that of Pt/carbon fiber CE ($\eta = 2.93\%$). In another study, composites of flower-like MoS₂ microspheres and carbon materials such as vulcan carbon, acetylene black, MWCNTs, carbon nanofibers (CNFs), and rice husk ash were studied as cost-effective Pt-free CEs for DSSCs.¹⁷³ The electrolyte used in the DSSC was a phthaloylchitosan-based polymer. The carbon materials/MoS₂ CEs showed low R_{CT} at the CE/electrolyte interface and high electro-catalytic activity for I₃⁻ reduction. The DSSC with MoS₂/



CNF CE showed a PCE of 3.17%, compared to a PCE of 1.04% for the pure MoS_2 CE.

Another study used MoS_2 and PEDOT:PSS composites as CEs for DSSCs.¹⁷⁴ The MoS_2 /PEDOT:PSS composite CE exhibits a PCE of 5.7% and FF of 58%, comparable to the Pt CE. The high PCE of the MoS_2 /PEDOT:PSS CE originated from high electrocatalytic activity of the MoS_2 active sites for triiodide (I_3^-) reduction and high conductivity of PEDOT:PSS. The inorganic/organic MoS_2 /PEDOT:PSS composite may be useful as a low-cost Pt-free CEs for DSSCs. Another study used $\text{Bi}_5\text{FeTi}_3\text{O}_{15}$ (BFTO) nanofibers of 40–100 nm diameter developed by a sol-gel aided electrospinning method.¹⁷⁵ The MoS_2 /BFTO nanocomposite-based CE for DSSCs was prepared by uniformly dispersing MoS_2 nanoparticles into the BFTO matrix. The optical bandgap of the MoS_2 /BFTO nanocomposites was found to decrease with increasing MoS_2 contents. The DSSC with a MoS_2 /BFTO nanocomposite-based CE showed a PCE of 5.20%, 24 times higher than that of the pure BFTO nanofiber based CE. Table 2 summarizes the electrochemical and photovoltaic properties of all types of MoS_2 based CEs discussed in this section above, and a comparison is made with conventional Pt CEs for DSSCs.

3.2 WS_2 counter electrodes

Tungsten disulfide (WS_2), traditionally used as a lubricant, is a semiconductor having van der Waals bonding which forms 2D layered-structures similar to other TMDs. WS_2 can form atomically thin nanosheets,^{176,177} nanorods,¹⁷⁸ and nanotubes,^{179,180} which have been actively studied for potential applications.

Carbon-coated WS_2 CEs have been fabricated for DSSCs at low temperature and characterized using FESEM, XRD, and Raman spectroscopy.¹⁸¹ The electrocatalytic activity of the WS_2 CEs was studied using CV and EIS. The DSSCs with carbon-coated WS_2 CEs show a PCE of 5.5%, comparable to that of Pt CE based DSSCs ($\eta = 5.6\%$). A DSSC having plastic WS_2 CEs exhibited a PCE of 5.0%. Carbon-coated WS_2 seems promising to develop low cost Pt-free CEs for DSSCs. The WS_2 films were

deposited by radio frequency (RF) sputtering and a sulfurization process as CE for DSSCs.¹⁸² The WS_2 films were characterized using XRD, FESEM, Raman spectroscopy, and XPS techniques. The transparent WS_2 CEs demonstrated high electrocatalytic activity and fast reduction of triiodide, (I_3^-) as characterized using CV, EIS, and Tafel polarization curve. WS_2 CE sputtered for 10 minutes showed a PCE of 6.3%, slightly lower than the Pt-based CE ($\eta = 6.64\%$) used in the DSSC. The J - V characteristics as a function of sputtering time used to prepare WS_2 films as a CE were also studied. WS_2 film CEs prepared at sputtering time of 5, 10 and 15 minutes showed PCEs of 5.4%, 6.3% and 5.8%, respectively.

Another research team¹⁸³ used edge-oriented WS_2 based CEs for DSSCs. Edge-oriented WS_2 was obtained from mesoporous interconnected WO_3 structures using a high temperature sulfurization process. The DSSCs with edge-oriented WS_2 CEs show a PCE of 8.85%, higher compared to the Pt CE ($\eta = 7.20\%$). The large number of active edge sites in edge-oriented WS_2 is responsible for high electrocatalytic activity for the reduction of triiodide (I_3^-) in the DSSCs. The WS_2 films were fabricated by the doctor-blade method (or tape casting method; a method removing excessive liquid material using a moving blade for uniform coating) to use as CEs for DSSCs.¹⁸⁴ The TiO_2 (P25) and carbon nanoparticles were introduced into WS_2 films to increase electrical conductivity and bonding strength. The electrochemical catalytic activity of WS_2 /P25/C CEs was compared with Pt for the triiodide (I_3^-) to iodide (I^-) electrolyte system using CV and EIS measurements. The DSSC developed with WS_2 /P25/C CE was shown to yield a PCE of 4.56%.

Yue *et al.*¹⁸⁵ prepared WS_2 decorated multi-walled carbon nanotubes (MWCNTs) by applying a hydrothermal method, for use as a low-cost Pt-free CE for DSSCs. The contents of MWCNTs in MWCNTs- WS_2 CEs varied from 1 to 10 wt%. PCE values of 5.20, 5.45, 6.41, 5.53 and 5.22% were measured in the DSSCs for CEs having 1, 3, 5, 7 and 10 wt% contents of MWCNTs, respectively. CV and EIS showed high electrocatalytic activity for the MWCNTs- WS_2 CE for the triiodide (I_3^-) reduction. The R_{CT}

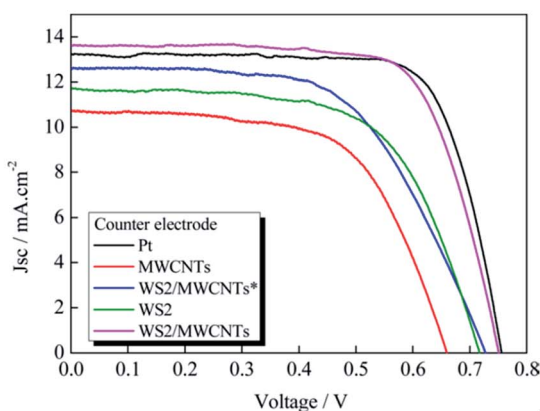
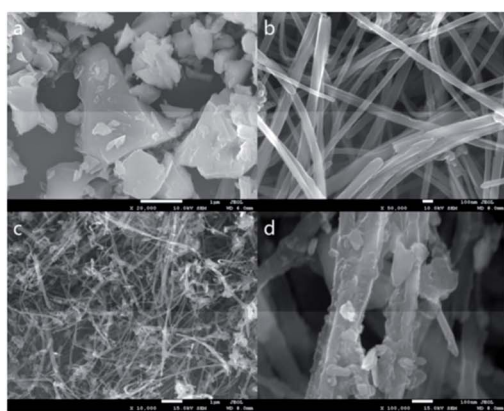


Fig. 11 (Left) SEM images of (a) WS_2 , (b) MWCNTs, and (c and d) WS_2 /MWCNTs composites. (Right) photocurrent–voltage (J - V) curves of the DSSCs with Pt, WS_2 , MWCNTs, WS_2 /MWCNTs* (prepared without glucose aid), and (G-A) WS_2 /MWCNTs counter electrodes under a simulated solar illumination of 100 mW cm^{-2} . Reprinted with permission from ref. 186, J. Wu, G. Yue, Y. Xiao, M. Huang, J. Lin, L. Fan, Z. Lan and J. Y. Lin, glucose aided preparation of tungsten sulfide/multi-wall carbon nanotube hybrid and use as counter electrode in dye-sensitized solar cells. *ACS Appl. Mater. Interfaces*, 2012, 4, 6530–6536. Copyright© American Chemical Society.



of MWCNTs–WS₂ CEs having 1, 3, 7, and 10 wt% contents of MWCNTs were 4.54, 3.47, 3.24, and 4.59 $\Omega \text{ cm}^2$, respectively. The R_{CT} of the MWCNTs–WS₂ CE with 5 wt% contents of MWCNTs shows 2.53 $\Omega \text{ cm}^2$, comparable to the R_{CT} of 2.74 $\Omega \text{ cm}^2$ for a Pt CE. The DSSCs based on WS₂/MWCNTs CEs showed a PCE of 6.41% for 5 wt% MWCNTs, comparable to the PCE of 6.56% for Pt CE under a simulated AM 1.5 solar illumination (100 mW cm^{-2}). The low R_{CT} of WS₂/MWCNTs CEs at the electrolyte/electrode interface contributed to the higher PCEs.

The WS₂ based CEs prepared by a hydrothermal method was also used for DSSC by Wu *et al.*¹⁴¹ which exhibited a PCE of 7.73%. The same research team¹⁸⁶ also synthesized WS₂/MWCNTs hybrids by a glucose-aided (G-A) hydrothermal route, which is discussed here in detail. Fig. 11 presents the SEM images of WS₂, MWCNTs, and (G-A)WS₂/MWCNTs composites, and J – V curves of the DSSCs with WS₂, MWCNTs, WS₂/MWCNTs* (prepared without the aid of glucose), WS₂/MWCNTs, and Pt CEs, under a simulated solar illumination of 100 mW cm^{-2} . The WS₂ exhibits graphene-like lamellar structure, whereas the MWCNTs have a fiber-like structure, indicating both materials have a large specific surface area. The specific surface area of the (G-A)WS₂/MWCNTs composite was estimated to be 230 $\text{m}^2 \text{ g}^{-1}$ by the Brunauer–Emmett–Teller (BET) technique, indicating high electrochemical activity as well as photovoltaic efficiency for CEs. The cathodic peak potentials of the WS₂, WS₂/MWCNTs, and WS₂/MWCNTs* CEs showed cathodic peak potentials of –0.14, –0.13 and –0.17 V, respectively, which implies that the MWCNTs help in improving the electrocatalytic activity, and a lower cathodic peak potential observed for (G-A)WS₂/MWCNTs as opposed to WS₂/MWCNTs* results from the large specific surface area generated by glucose aided preparation. The EIS measurements yielded an R_{CT} of 2.49 $\Omega \text{ cm}^2$ and R_s of 2.54 $\Omega \text{ cm}^2$ for the WS₂/MWCNTs hybrid CE, which is smaller compared with WS₂ CE, and indicates the synergistic effect between WS₂ and MWCNTs that enhanced the electrical conductivity of the hybrid. The (G-A)WS₂/MWCNT CE based DSSC resulted in a PCE of 7.36%, comparable to WS₂ CE (5.32%), MWCNTs CE (4.34%), and the Pt CE (7.54%). The J_{sc} and PCE values increased with increasing content of MWCNTs, up to 5 wt% in the WS₂/MWCNT hybrid CEs, and thereafter started decreasing with further increases in MWCNTs content. The (G-A)WS₂/MWCNT (5 wt%) film also exhibits a smaller transmission between 320 to 800 nm than Pt film, therefore the WS₂/MWCNT film absorbs more incident light, which also further improves photovoltaic performance. The glucose aided (G-A)WS₂/MWCNTs (5 wt%) CE in the DSSC had low R_{CT} and high electrocatalytic activity for the reduction of triiodide (I_3^-), due to the synergistic effects induced by glucose.

3.3 TiS₂ counter electrodes

Titanium disulfide (TiS₂) is a metallic thermoelectric material which attains unique morphologies such as nanotubes, nano-clusters and nanodisks, and exhibits interesting physical properties.^{187–198} Meng *et al.*¹⁹⁹ has prepared 2D TiS₂ nanosheets decorated on graphene using a ball milling method and followed by high-temperature annealing. The electroactive surface

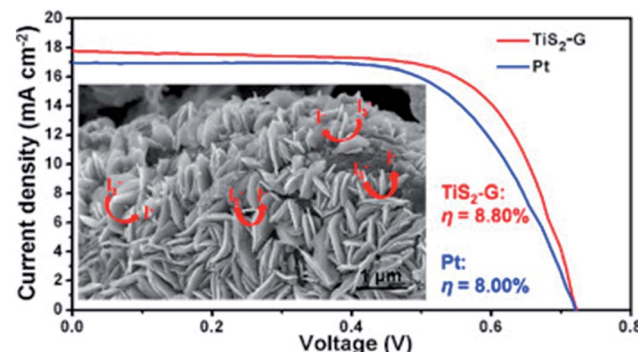


Fig. 12 A comparison of photocurrent density–voltage (J – V) curves of DSSCs having TiS₂–graphene hybrid and Pt counter electrodes. Reprinted with permission from ref. 199, X. Meng, C. Yu, B. Lu, J. Yang and J. Qiu, dual integration system endowing two-dimensional titanium disulfide with enhanced triiodide reduction performance in dye-sensitized solar cells. *Nano Energy*, 2016, 22, 59–69. Copyright © Elsevier.

areas of 1.70 cm^2 for TiS₂–graphene and 0.232 cm^2 for Pt electrodes, measured by CV, indicate more active sites for the hybrid. Fig. 12 compares J – V curves of DSSCs having TiS₂–graphene and Pt/FTO CEs. The CEs based on TiS₂–graphene hybrids exhibited higher electrocatalytic activity for the reduction of triiodide (I_3^-) to iodide (I^-) in electrolyte with a PCE of 8.80%, which is higher than the Pt CE ($\eta = 8.00\%$). The R_s of TiS₂–graphene CEs (2.32 $\Omega \text{ cm}^2$) was found to be smaller compared to the Pt CEs (6.90 $\Omega \text{ cm}^2$), showing better contact between the hybrid CE and FTO glass. Furthermore, the R_{CT} of TiS₂–graphene CE (0.63 $\Omega \text{ cm}^2$) was also lower than the Pt CE (1.32 $\Omega \text{ cm}^2$), which again indicates a higher electrocatalytic activity for the reduction of triiodide (I_3^-). Also, the Z_N of TiS₂–graphene CE (10.52 $\Omega \text{ cm}^2$) was found to be higher than the Pt CE (6.89 $\Omega \text{ cm}^2$). The high electrocatalytic activity of the TiS₂–graphene hybrids is attributed to the highly electroactivity of TiS₂ and enhanced transport facilitated by the graphene conductive network.

Li *et al.*²⁰⁰ deposited composite films of TiS₂/PEDOT:PSS on ITO substrates by drop coating, to study CEs of DSSCs. The wt% of TiS₂ particles in TiS₂/PEDOT:PSS composite films varied from 5 to 15 wt%. TiS₂ particles were dispersed in a PEDOT:PSS matrix to be used as an electrocatalyst for the I^-/I_3^- redox reaction. In the composite, conducting polymer PEDOT:PSS plays the role of a binder for the TiS₂ nanoparticles, as well as a linking agent between TiS₂ particles and the ITO substrate, and also facilitates electron transfer. The TiO₂ photoanode for a DSSC was prepared by immersing it in N719 dye solution for 24 hours at room temperature. Fig. 13 shows the photocurrent density–voltage curves and IPCE curves of the DSSCs with Pt, bare TiS₂, bare PEDOT:PSS, and 10 wt% TiS₂/PEDOT:PSS composite CEs. The TiS₂/PEDOT:PSS composite CE offered a large surface area, yielding a high PCE of 7.04%. The CEs of bare TiS₂, bare PEDOT:PSS, the TiS₂/PEDOT:PSS composite, and Pt were characterized by AFM, SEM, and EDX. AFM images indicated a roughness of 45 nm for PEDOT:PSS and of 378 nm for TiS₂/PEDOT:PSS composite film; therefore, the higher



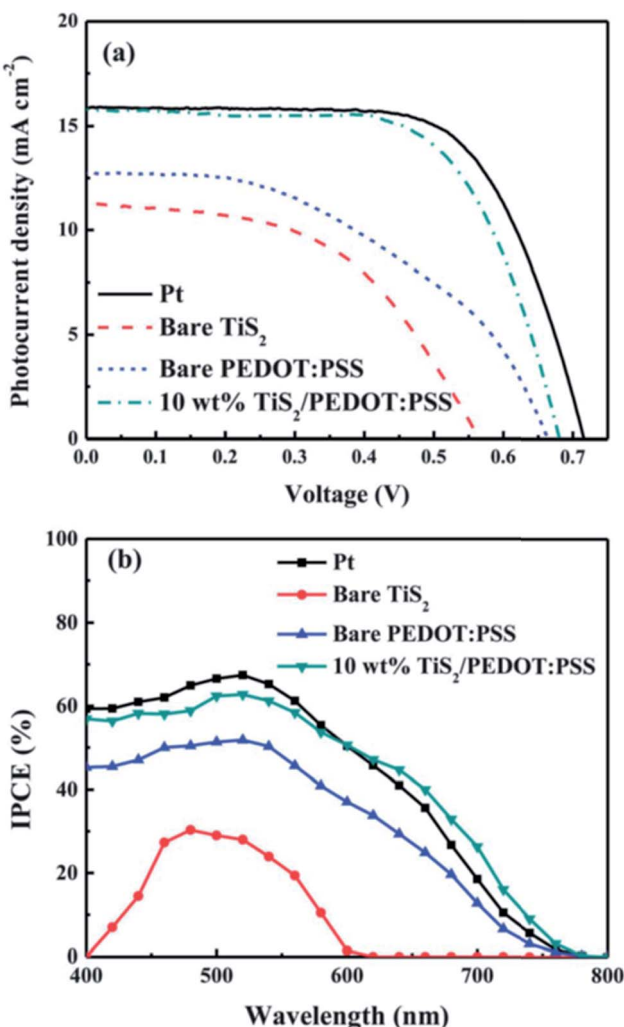


Fig. 13 (a) Photocurrent density–voltage curves of DSSCs with Pt, bare TiS₂, bare PEDOT:PSS, and 10 wt% TiS₂/PEDOT:PSS composite based CEs recorded under light illumination of 100 mW cm⁻² (AM 1.5). (b) Incident photon-to-current conversion efficiency (IPCE) curves of the DSSCs with similar CEs. Reprinted with permission from ref. 200, C. T. Li, C. P. Lee, Y. Y. Li, M. H. Yeh and K. C. Ho, a composite film of TiS₂/PEDOT:PSS as the electrocatalyst for the counter electrode in dye-sensitized solar cells. *J. Mater. Chem. A*, 2013, **1**, 14888–14896. Copyright © Royal Society of Chemistry.

roughness could lead to a larger active surface area and consequently to the higher electrocatalytic activity for the TiS₂/PEDOT:PSS composite thin. The electrocatalytic properties of the DSSCs using the CEs of bare TiS₂, bare PEDOT:PSS, the TiS₂/PEDOT:PSS composite, and Pt were evaluated by CV, RDE, EIS, and Tafel polarization measurements. The high PCE of the TiS₂/PEDOT:PSS composite CE based DSSC was also measured by IPCE curves. The maximum of the IPCE spectra at 520 nm increased from 52% to 63% as the content of TiS₂ particles increased from 0 to 10 wt%, respectively, and similar characteristics were observed for the J_{sc} values from the $J-V$ curves of the DSSCs. The 10 wt% TiS₂/PEDOT:PSS composite film based CE shows a higher redox current density compared with bare TiS₂ and PEDOT:PSS CEs, therefore, it possesses high

electrocatalytic activity for triiodide (I_3^-) reduction, and it also exhibits high electrochemical stability after 100 consecutive cycles in the I^-/I_3^- redox electrolyte.

3.4 NiS₂ counter electrodes

Nickel disulfide (NiS₂) is a semiconducting material with pyrite structure which acquires unique morphologies such as hollow prisms, nano/microspheres, nanocubes, nanosheets, nanoparticles, and also exhibits interesting electrical, optical, magnetic, and catalytic properties.^{201–205} Depending upon the synthesis procedures, the stoichiometric composition of nickel sulfide varies to a great extent (NiS, NiS₂, Ni₃S₂, Ni₃S₄, Ni₆S₅, Ni₇S₆, Ni₉S₈, etc.).

In one study, hierarchical NiS₂ hollow microspheres on a FTO substrate were prepared by a hydrothermal method to use as a CE for a DSSC.²⁰⁶ The NiS₂ hollow microspheres were partially broken, offering more active sites for electrocatalysis and electrolyte adsorptions. The IPCE values of 81.3% for the NiS₂ microspheres CE and 76.6% for the Pt CEs at 500 nm were observed. The peak current density of the NiS₂ microspheres CE was found to be higher than the Pt CE, whereas the peak-to-peak separation (E_{pp}) value was lower by 10 mV compared to Pt CE, which suggests a high electrocatalytic activity for the NiS₂ microspheres CE in the reduction of triiodide (I_3^-) in the electrolyte. The NiS₂ hollow microspheres CE based DSSC showed a PCE of 7.84%, equal to the Pt CE (7.89%), indicating their potential as low-cost CEs for DSSCs. The NiS/NiS₂ composite hollow spheres prepared by a solvothermal method exhibited a low R_{CT} of 0.34 Ω cm⁻² at the CE/electrolyte interface, and a PCE of 7.66%, outperforming the Pt CE (7.01%), and showed high electrocatalytic activity for I_3^- reduction, and also better electrochemical stability.²⁰⁷ The NiS and NiS₂ hollow spheres were synthesized through a solvothermal process.²⁰⁸ The Ni/S molar ratio controlled the different stoichiometric ratios of nickel sulfides. The NiS₂ CE based DSSC showed a higher electrocatalytic activity than that of the NiS CE for I_3^- reduction. The DSSC with NiS₂ CE yielded a PCE value of 7.13% in comparison to 6.49% for NiS CE.

NiS₂ polyhedrons were studied as CEs for DSSCs by Zheng *et al.*²⁰⁹ Fig. 14 shows SEM, TEM, and selected area electron diffraction (SAED) images of NiS₂ octahedrons and NiS₂ cubes, and electrochemical characteristics of DSSCs having NiS₂ octahedrons, NiS₂ cubes and Pt CEs, under simulated AM1.5G solar light. The average size of NiS₂ octahedrons and cubes were about 250 nm. The electrochemical performance of NiS₂ octahedron and cube based CEs were evaluated using CV, $J-V$ characteristics, EIS, and the Tafel polarization method. The NiS₂ octahedron CEs showed peak current density of 1.40 mA cm⁻², compared to 1.22 mA cm⁻² for the NiS₂ cubes, indicating better electrocatalytic activity. The NiS₂ octahedron CEs also exhibited a higher J_{sc} of 13.55 mA cm⁻² and FF of 62%, higher than that of the NiS₂ cube CE (J_{sc} of 12.62 mA cm⁻² and FF of 60%), giving rise to a higher PCE. Octahedral NiS₂ nanocrystals based CEs incorporated into DSSCs exhibited a PCE of 5.98%, slightly higher than that of the NiS₂ cube nanocrystals (η = 5.43%). The NiS₂ octahedron CE had a PCE of up to 91% of the



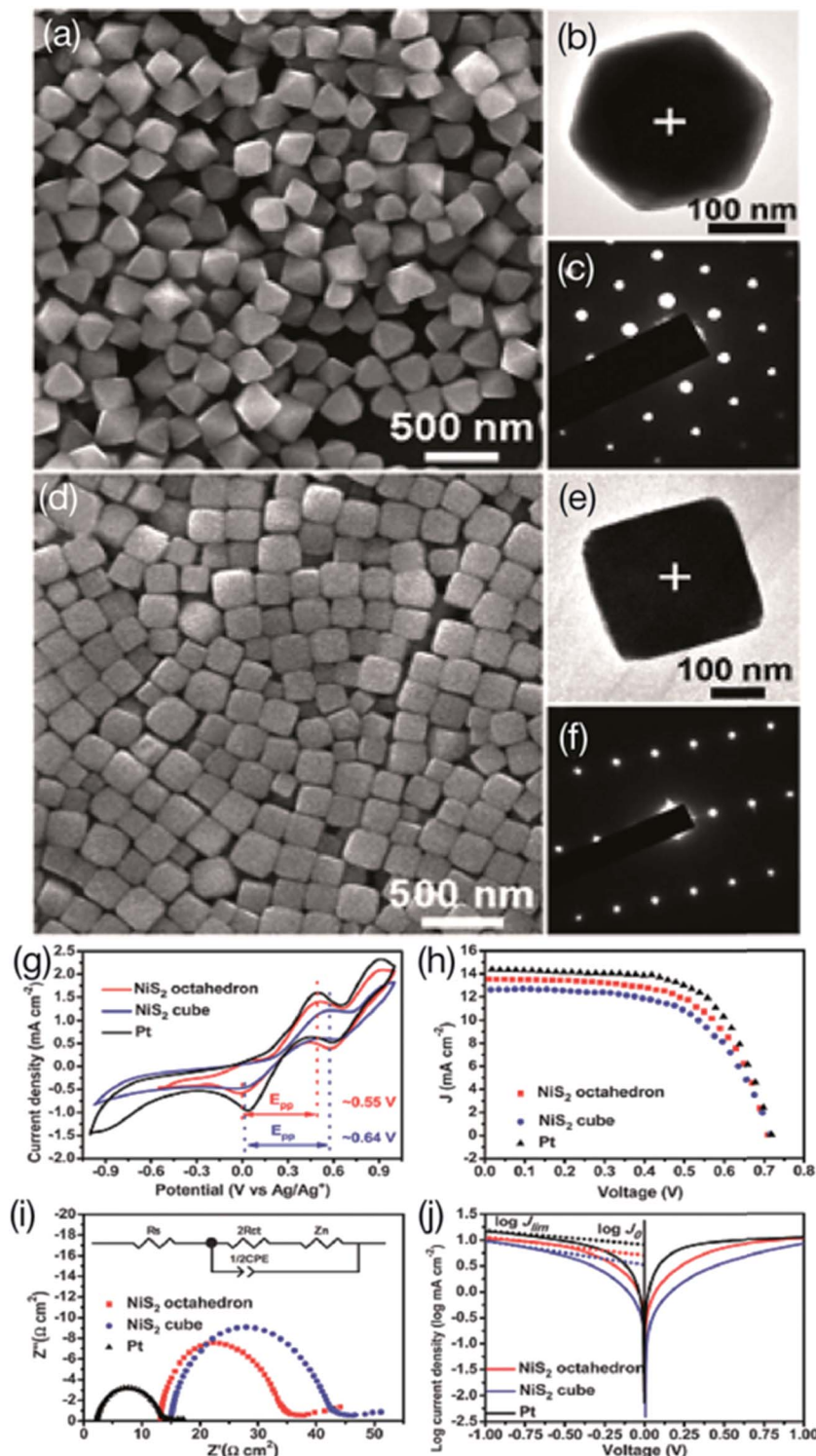


Fig. 14 SEM, TEM, and SAED images of NiS_2 octahedrons (a–c) and NiS_2 cubes (d–f). SAED patterns of NiS_2 octahedrons (c) and NiS_2 cubes (f) were recorded from the corresponding particles depicted (b) and (e), respectively. (g) C–V curves of DSSCs having counter electrodes of NiS_2 octahedrons, NiS_2 cubes and Pt for the reduction of tri-iodide (h) J – V curves of DSSCs with NiS_2 octahedrons, NiS_2 cubes and Pt CEs under simulated AM1.5G solar light. Nyquist plots (i) and Tafel polarization curves (j) of DSSCs having NiS_2 octahedrons, NiS_2 cubes and Pt CEs. Reprinted with permission from ref. 209, J. Zheng, W. Zhou, Y. Ma, W. Cao, C. Wang and L. Guo, facet-dependent NiS_2 polyhedrons on counter electrodes for dye-sensitized solar cells. *Chem. Commun.*, 2015, 51, 12863–12866. Copyright © Royal Society of Chemistry.

conventional Pt CE in DSSCs ($\eta = 6.55\%$). The R_s of the NiS_2 octahedron based CE was $13.14 \Omega \text{ cm}^2$, somewhat lower than that of the NiS_2 cube CE (R_s of $14.98 \Omega \text{ cm}^2$), indicating higher

electrical conductivity of the NiS_2 octahedron based CE. The R_{CT} of the NiS_2 octahedron CE was measured as $9.86 \Omega \text{ cm}^2$, also lower than that of the NiS_2 cube CE (R_{CT} of $13.17 \Omega \text{ cm}^2$), which

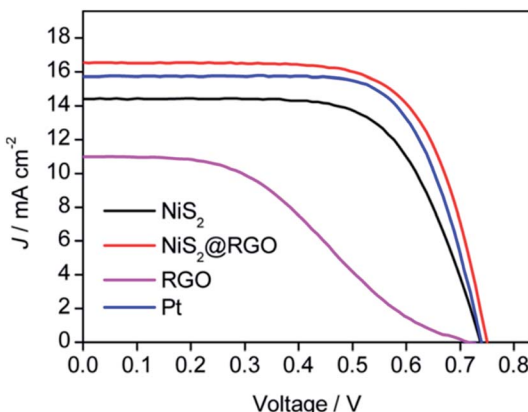


Fig. 15 (a) Photocurrent density–voltage (J – V) curves of DSSCs with bare NiS_2 , $\text{NiS}_2@\text{RGO}$ nanocomposites, bare RGO, and Pt CEs measured under light illumination of 100 mW cm^{-2} (AM 1.5). Reprinted with permission from ref. 210, Z. Li, F. Gong, G. Zhou and Z. S. Wang, NiS_2 /reduced graphene oxide nanocomposites for efficient dye-sensitized solar cells. *J. Phys. Chem. C*, 2013, **117**, 6561–6566. Copyright © American Chemical Society.

demonstrates that the NiS_2 octahedrons with $\{111\}$ facets possesses better electrocatalytic activity than the NiS_2 cubes with $\{100\}$ facets.

The electrocatalytic performance of NiS_2 nanoparticles and their nanocomposites with RGO were compared by Li *et al.*²¹⁰ In a hydrothermal process, graphene oxide was transformed to RGO, and then $\text{NiS}_2@\text{RGO}$ nanocomposites were formed by depositing NiS_2 nanoparticles on the surface of RGO. CEs for DSSCs were fabricated by drop-casting solutions of NiS_2 , $\text{NiS}_2@\text{RGO}$, and RGO nanocomposites on FTO-coated glass substrate. The surface areas measured by the BET method were 11.4 , 9.4 , and 8.6 , and $5.8 \text{ m}^2 \text{ g}^{-1}$ for $\text{NiS}_2@\text{RGO}$, NiS_2 , and RGO, respectively. Fig. 15 shows J – V curves of DSSCs with bare NiS_2 , $\text{NiS}_2@\text{RGO}$ nanocomposites, bare RGO, and Pt CEs. The $\text{NiS}_2@\text{RGO}$ nanocomposites based CE showed a PCE of 8.55% ($J_{sc} = 16.55 \text{ mA cm}^{-2}$, $V_{oc} = 0.749 \text{ V}$, and $FF = 0.69$), much higher than that of the NiS_2 CE ($\eta = 7.02\%$), RGO CE ($\eta = 3.14\%$), or standard Pt CE ($\eta = 8.15\%$) for the DSSCs under the same experimental conditions. The larger R_{CT} values of $100.2 \Omega \text{ cm}^2$ for RGO and $8.8 \Omega \text{ cm}^2$ for NiS_2 also suggest the low electrocatalytic activity. On the other hand, the smaller R_{CT} value of $2.9 \Omega \text{ cm}^2$ for the $\text{NiS}_2@\text{RGO}$ nanocomposite indicates much higher electrocatalytic activity for the reduction of triiodide (I_3^-) in electrolyte due to the cooperative synergistic effect and the increased conductivity from the RGO nanosheets. This study demonstrates that $\text{NiS}_2@\text{RGO}$ nanocomposites are a promising alternate CE to conventional Pt CE for DSSC devices.

3.5 FeS_2 based counter electrodes

Pyrite iron disulfide (NiS_2) acquires unique morphological structures including nanocrystals, nanowires, nanosheets, nanocubes, and exhibits interesting electrical, photovoltaic, and catalytic properties.^{211–220} An interesting comparative study was done by Shukla *et al.*²²¹ on pyrite iron disulfide (FeS_2) as a CE material in comparison with Pt and PEDOT CEs in DSSCs.

The FeS_2 film CEs were fabricated on a FTO glass substrate by a spray pyrolysis method and used in I_3^-/I^- and $\text{Co}(\text{III})/\text{Co}(\text{II})$ electrolyte-mediated DSSCs. N719 dye was used for the DSSC with I_3^-/I^- redox electrolyte and C128 dye for the $[\text{Co}(\text{bpy})_3]^{2+/3+}$ redox electrolyte. The I_3^-/I^- redox electrolyte contained 1.0 mM of 1,3-dimethylimidazolium iodide, 50 mM of LiI , 30 mM of I_2 , 0.5 mM of *tert*-butylpyridine, and 0.1 mM of guanidinium thiocyanate in a acetonitrile and valeronitrile (v/v, 85/15) mixed solution. The cobalt electrolyte was made up of 0.22 M of $\text{Co}(\text{bpy})_3(\text{TFSI})_2$, ($\text{bpy} = 2,2'$ -bipyridine and $\text{TFSI} = [\text{bis}(\text{trifluoromethane})\text{-sulfonimide}]$), 0.05 M of $\text{Co}(\text{bpy})_3(\text{TFSI})_3$, 0.1 M of lithium *bis*(trifluoromethanesulfonyl)imide (LiTFSI), and 0.2 M of *tert*-butylpyridine (*tBP*) in acetonitrile. Fig. 16 shows the J – V curves and IPCE of the DSSCs with FeS_2 and Pt CEs in I_3^-/I^- electrolyte, and DSSCs with FeS_2 and PEDOT CEs in the $\text{Co}(\text{III})/\text{Co}(\text{II})$ electrolyte. The catalytic activity of the FeS_2 film CEs was found to be comparable to the Pt and PEDOT CEs, which were both in I_3^-/I^- and $\text{Co}^{2+}/\text{Co}^{3+}$ electrolytes, respectively. With the I_3^-/I^- electrolyte, a PCE of 7.97% was observed for the FeS_2 film CE and a PCE of 7.54% for the Pt CE in the I_3^-/I^- electrolyte, whereas the PCEs were almost the same (6.3%) for the FeS_2 film and PEDOT CEs in the $[\text{Co}(\text{bpy})_3]^{2+/3+}$ redox-mediated DSSCs. The performance of the DSSCs with FeS_2 and Pt CEs was studied by varying solar light illumination intensities between 1 Sun and 0.1 Sun . The current density was observed to be higher for the FeS_2 CE (15.20 mA cm^{-2}) than for the Pt CE (14.77 mA cm^{-2}) at 1 Sun light intensity. When the solar light intensity was reduced to 0.5 and 0.1 Sun , the difference in current density between the FeS_2 and Pt CEs was not noticeable, with the J_{sc} values being 8.97 and 8.91 mA cm^{-2} at 0.5 Sun , and 1.75 and 1.74 mA cm^{-2} at 0.1 Sun for the Fe and Pt CEs, respectively. The PCE values for the FeS_2 and Pt CEs were 9.27% and 8.92% at 0.5 Sun , and 8.68% and 8.32% at 0.1 Sun , respectively. The excellent performance of FeS_2 film in both electrolyte systems makes it very interesting for applications in DSSCs.

In an interesting study, FeS_2 nanorod arrays were fabricated on a FTO substrate after sulfurizing $\text{FeO}(\text{OH})$ nanorods, and used as a CE for DSSCs.²²² The FeS_2 nanorods exhibited better electrocatalytic activity than FeS_2 films and Pt-based CEs due to more active sites, which resulted in high J_{sc} value of the DSSCs. The FeS_2 nanorods-based CEs showed lower interface resistance compared with FeS_2 thin films, which leads to a higher FF and hence a higher PCE comparable to Pt CE based DSSCs. The electrochemical stability of the FeS_2 nanorod arrays-based CE measured in I_3^-/I^- electrolyte showed a slight change in CV plots up to 10 consecutive days of aging time. In another study, FeS_2 powder prepared through a hydrothermal method was used as a CE for fabricating DSSCs.²²³ The effect of NaOH addition on FeS_2 crystal size and electrocatalytic activities was then studied. It was observed that the size of FeS_2 nanoparticles decreased after adding NaOH , and the resulting photovoltaic performance and electrocatalytic activity of DSSC with FeS_2 powder significantly increased, achieving a PCE of 5.78% under simulated sunlight irradiation of 1 Sun .

A chemically prepared FeS_2 nanocrystal ink was used to fabricate a CE for a DSSC, which showed a PCE of 7.31% after



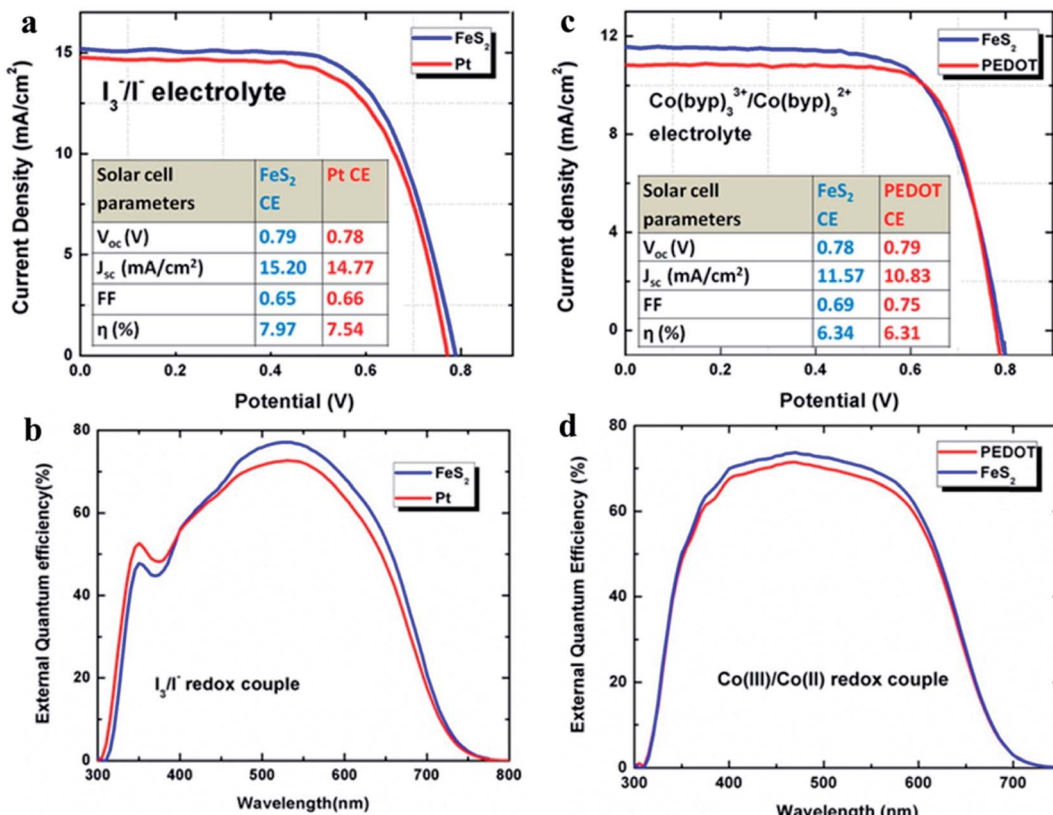


Fig. 16 (a) Photocurrent density–voltage (J – V) curves and (b) IPCE of the DSSCs with FeS_2 and Pt counter electrodes using N719 dye in I_3^-/I^- electrolyte. (c) J – V curve and (d) IPCE of the DSSCs with FeS_2 and PEDOT counter electrodes using C128 dye in $\text{Co}^{3+}/\text{Co}^{2+}$ electrolyte. Reprinted with permission from ref. 221, S. Shukla, N. H. Loc, P. P. Boix, T. M. Koh, R. R. Prabhakar, H. K. Mulmudi, J. Zhang, S. Chen, C. F. Ng, C. H. A. Huan and N. Mathews, iron pyrite thin film counter electrodes for dye-sensitized solar cells: high efficiency for iodine and cobalt redox electrolyte cells. *ACS Nano*, 2014, 8, 10597–10605. Copyright © American Chemical Society.

ethanedithiol (EDT) treatment.²²⁴ FeS_2 nanocrystal ink casted on a flexible ITO/PET substrate exhibited a J_{sc} of 14.93 mA cm^{-2} , V_{oc} of 0.71 V , FF of 0.60 , and a PCE of 6.36% . The semi-transparent FeS_2 nanocrystal/ITO glass CE has an optical transmittance of $50\text{--}70\%$ between 300 to 800 nm in comparison to 15% transmittance for the reference Pt/ITO glass CE. When the DSSC with the FeS_2 nanocrystal CE was illuminated from the rear side, it showed a PCE of 4.17% , which was 57% of the front illumination value, whereas opaque Pt CE had a PCE of 1.06% from the rear side. Semi-transparent FeS_2 nanocrystal CEs offer bifacial DSSCs utilizing incident light from both front and rear sides, and thus could be cost-effective for energy production. The FeS_2 nanocrystal ink also demonstrated high electrocatalytic activity and electrochemical stability. Additionally, MWCNT/TiO₂ hybrid and pure TiO₂ mesoporous photoanodes with FeS_2 thin films as CEs were studied for DSSCs by Kilic *et al.*²²⁵ In the MWCNT/TiO₂ hybrid photoanode, CNT played an important role of increasing the optical absorption and shifting it toward a longer wavelength region, where the bandgap of 3.15 eV for mesoporous TiO₂ shifted to 2.5 eV for the MWCNT/TiO₂ hybrid. The DSSC with the MWCNT/TiO₂ hybrid photoanode and the Pt CE showed values of J_{sc} of 15.96 mA cm^{-2} , V_{oc} of 0.77 V , FF of 0.57 and a PCE of 7.0% . The DSSC with a pure TiO₂ photoanode and the Pt CE both resulted in

PCEs of 6.51% . The enhancement in PCE value of the hybrid photoanode is associated with MWCNTs, which offer an electrical conduction pathway for speedy electron transport. The MWCNT/TiO₂ hybrid photoanode also showed an increase in IPCE in the $350\text{--}600 \text{ nm}$ wavelength range compared to the mesoporous TiO₂ photoanode. When FeS_2 thin films were used as a CE with a MWCNT/TiO₂ hybrid photoanode, the PCE of the DSSC increased to 7.27% under 1 Sun . The DSSC with a FeS_2 CE and a pure TiO₂ photoanode both yielded a PCE of 6.65% . The FeS_2 thin films showed an optical bandgap of 1.27 eV and large effective surface area, which contribute to more light absorption and increased electrocatalytic activity for the reduction of triiodide (I_3^-).

3.6 CoS₂ counter electrodes

Cobalt disulfide (CoS₂) is a semiconducting material that exhibits interesting magnetic, electrical, and catalytic properties for energy storage applications.^{226–231} The properties of CoS₂ nanocrystalline thin films prepared by a hydrothermal method were reported by Jin *et al.*²³² CoS₂ powder was dispersed in ethanol in order to prepare a nanoink (40 mg m L^{-1}) for fabricating a CE. The CoS₂ nanoink ($10 \mu\text{L}$) was drop-cast on an FTO glass or flexible ITO/PET substrate, followed by ethanol



evaporation. The self-assembled CoS_2 film CE has a thickness of $2.5\ \mu\text{m}$ which can be controlled by the nanoink content. DSSCs were assembled by using a N719 dye-sensitized TiO_2 photo-anode as the working electrode, a CoS_2 nanocrystal film or a Pt as the CE, and an electrolyte solution containing LiI (0.1 M), I_2 (0.05 M) I_3^- , 1,2-dimethyl-3-*n*-propylimidazolium iodide (DMPII, 0.6 M), and 4-*tert*-butylpyridine (TBP, 0.5 M) in acetonitrile. The morphology and structure of the CoS_2 self-assemblies were studied by SEM and TEM techniques. Fig. 17 shows an SEM image of a self-assembled CoS_2 nanocrystal film, a photographic image of CoS_2 nanoink, a self-assembled CoS_2 CE, and J – V curves of the DSSCs, fabricated with the CoS_2 nanocrystal thin film and a Pt CE on the FTO and flexible ITO/polyethylene terephthalate (PET) substrate. The CoS_2 nanoparticles were stabilized with poly(vinylpyrrolidone) (PVP) to form an oriented structure. The DSSC with self-assembled CoS_2 CE shows a J_{sc} of $14.62\ \text{mA cm}^{-2}$, V_{oc} of $0.71\ \text{V}$, and a FF of 0.64, resulting in a PCE of 6.78%, which is comparable to a Pt CE with a value of 7.38%. The PCE was found to decrease when the thickness of the self-assembled CoS_2 film was either higher or lower than $2.5\ \mu\text{m}$. The CoS_2 shows a R_s value of $34.20\ \Omega\ \text{cm}^2$, slightly higher compared to Pt ($27.13\ \Omega\ \text{cm}^2$), indicating comparable electrical conductivity. The R_{CT} value of $7.21\ \Omega\ \text{cm}^2$ for the CoS_2 CE indicates higher electrocatalytic activity for the reduction of triiodide (I_3^-). The CoS_2 CE has a high chemical capacitance (C_{μ}) of $27.57\ \mu\text{F}$, compared to $2.76\ \mu\text{F}$ for the Pt CE, which also is evidence of a high surface area for CoS_2 CE which is beneficial to electrocatalysis. The DSSCs with CoS_2 deposited on a flexible ITO/PET substrate showed a J_{sc} of $13.17\ \text{mA cm}^{-2}$, V_{oc} of $0.70\ \text{V}$,

FF of 0.68 and a PCE of 6.40%. The fabrication of a CoS_2 CE is low-cost and solution processable at room temperature, which could make it an alternative to Pt CEs for flexible DSSCs.

Another study used mesoporous CoS_2 nanotube arrays deposited on an FTO glass substrate and used as a CE for a DSSC.²³³ The CoS_2 nanotube arrays were characterized by SEM, TEM, and XRD techniques for their morphology and crystal structures. The electrocatalytic properties of the CoS_2 nanotube arrays were measured using CV and Tafel polarization curve measurements. The DSSCs having CoS_2 CEs achieved a PCE of 6.13%, comparable to that of sputtered Pt CE (6.04%). The R_{CT} of the mesoporous CoS_2 nanotube array CE was found to be $3.51\ \Omega\ \text{cm}^2$ and comparable to the Pt CE ($5.78\ \Omega\ \text{cm}^2$). The CoS_2 nanotube array based CEs have large active surface area due to the mesoporous nanotube structure. The CoS_2 nanotube array CE also exhibits electrocatalytic activities comparable to Pt CE. Tsai *et al.*²³⁴ also prepared CoS_2 nanoflake arrays from Co(OH)_2 nanoflake arrays through an ion exchange reaction to develop CEs for DSSCs. The CoS_2 nanoflakes were found to be composed of CoS_2 single crystals as well as their aggregates. The DSSC with CoS_2 nanoflake arrays as a CE showed a PCE of 5.20%, comparable to a sputtered Pt CE (5.34%).

Different types of cobalt sulfide (CoS) have been used as CEs for DSSCs. The CoS nanoparticles deposited onto FTO glass substrates showed good transparency and high electrocatalytic activity for the I^-/I_3^- redox couple for a DSSC.²³⁵ CoS nanoparticle CEs showed a low R_{CT} value of $1.3\ \Omega\ \text{cm}^2$, less than that of Pt on FTO glass (R_{CT} of $2.3\ \Omega\ \text{cm}^2$) and achieved a PCE of 6.6%. An optimized CoS nanoparticle CE was also studied for

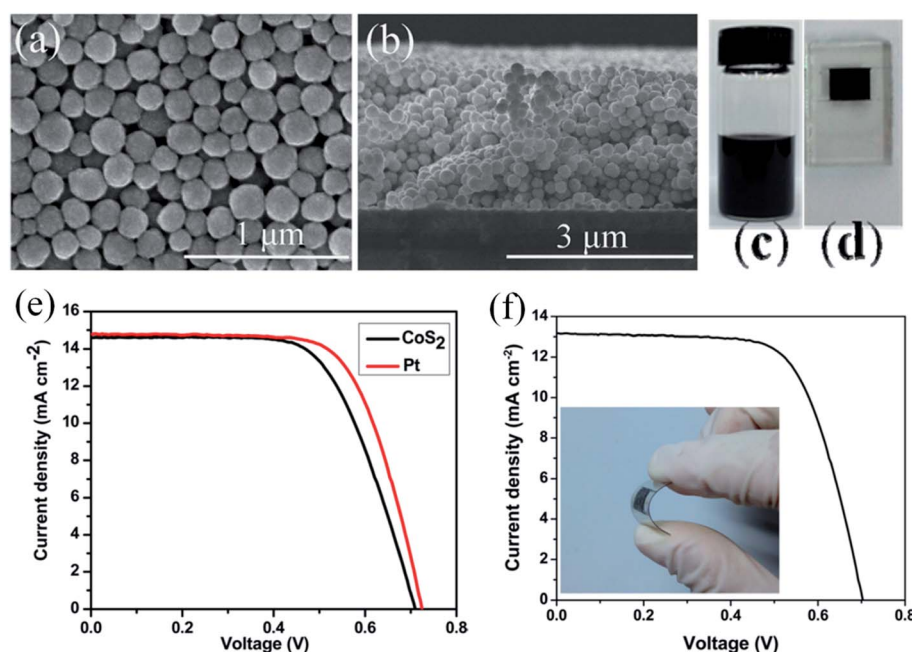


Fig. 17 (a) SEM image of a self-assembled CoS_2 nanocrystal film on FTO glass substrate, (b) cross-sectional SEM image of the CoS_2 counter electrode (CE), (c) photographic image of CoS_2 nanoink, and (d) self-assembled CoS_2 CE. (e) Photocurrent density–voltage (J – V) curves of the DSSCs with CoS_2 nanocrystal thin film and Pt CEs. (f) J – V curves of the DSSCs with CoS_2 deposited on a flexible ITO/PET substrate. Reprinted with permission from ref. 232, J. Jin, X. Zhang and T. He, self-assembled CoS_2 nanocrystal film as an efficient counter electrode for dye-sensitized solar cells. *J. Phys. Chem. C*, 2014, **118**, 24877–24883. Copyright © American Chemical Society.



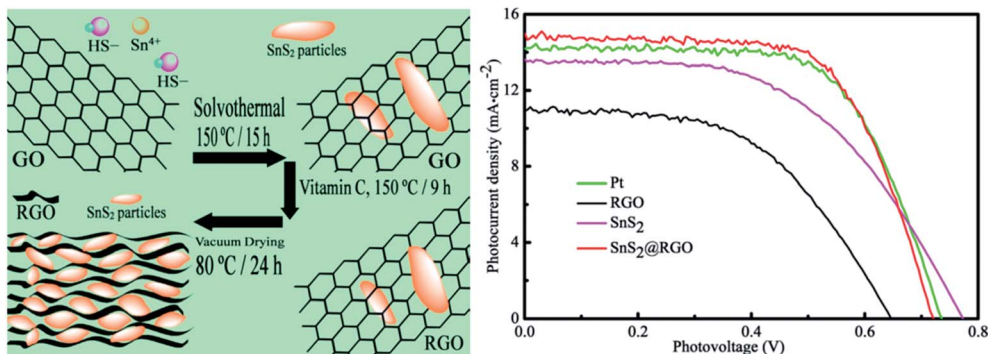


Fig. 18 (Left) illustration depicting preparation of tin sulfide nanoparticles/reduced graphene oxide (SnS_2 @RGO) nanocomposites. (Right) photocurrent density–photovoltage (J – V) curves for DSSCs having Pt, RGO, SnS_2 , and SnS_2 @RGO composite CEs. Reprinted with permission from ref. 250, B. Yang, X. Zuo, P. Chen, L. Zhou, X. Yang, H. Zhang, G. Li, M. Wu, Y. Ma, S. Jin and X. Chen, nanocomposite of tin sulfide nanoparticles with reduced graphene oxide in high-efficiency dye-sensitized solar cells. *ACS Appl. Mater. Interfaces*, 2015, 7, 137–143. Copyright © American Chemical Society.

a ferrocene-based liquid electrolyte. The rose-petal like CoS_2 was deposited on an FTO as CE using a chemical bath deposition method.²³⁶ The DSSC assembled with a CoS_2 CE achieved a PCE of 5.32%, higher than that of a Pt CE (5.02%). The PCEs of CoS_2 CEs depend on the deposition parameters including the concentrations of urea and thioacetamide, and the deposition time of the CEs. Also, CoS_2 embedded carbon nanocages were fabricated as CEs for DSSCs through a zeolitic imidazolate framework-67, $\text{Co}(\text{2-methylimidolate})_2$ template.²³⁷ The performance of the CoS_2 CE in a DSSC was optimized *via* a sulfurization process, where CoS_2 nanoparticles with embedded carbon nanocages were sulfurized for a period of 4 hours, and showed the highest PCE of 8.20%, even higher than Pt-based CE (7.88%). The synergic effect of CoS_2 nanoparticles and the carbon matrix resulted in the CE having high electrical conductivity and catalytic activity. Kim *et al.*²³⁸ deposited CoS_2 , nickel sulfide (NiS), and Ni-doped CoS_2 nanoparticles on a FTO substrate as CEs for DSSCs *via* a chemical bath deposition method. The surface morphology of the thin films was analyzed by SEM. Electrochemical properties of Ni-doped CoS_2 thin films evaluated by EIS, CV, and Tafel polarization curves indicated increased electrocatalytic activity for the reduction of I_3^- in the DSSCs compared to Pt CEs. The Ni-doped CoS_2 CE (15% Ni) showed a PCE of 5.50% under 1 Sun illumination, exceeding the PCE of the Pt CE ($\eta = 5.21\%$). PCE and R_{CT} values of the DSSCs were found to depend on the amount of Ni-doping of the CoS_2 nanoparticles. These yielded PCEs of 4.81, 5.17, 5.50, and 4.12%, for R_{CT} values of 279.7, 36.63, 8.53 and 82.72 Ωcm^2 , at 5, 10, 15 and 20% Ni contents in the CoS_2 CE, respectively. Comparatively, DSSCs with bare CoS_2 and NiS CEs showed poor electrocatalytic activity of I_3^- reduction.

In another study, CoS_2 /graphene composites were prepared *via* a hydrothermal method using Co ions with thiourea in the presence of graphene oxide (GO).²³⁹ The distribution and size of the CoS_2 nanoparticles deposited onto a flexible graphene sheet was controlled in order to optimize the electrocatalytic activity for I_3^- reduction. A CoS_2 nanoparticles/graphene sheet ($\text{CoS}_2/\text{G}_{50}$) CE was prepared by incorporating 50 mg graphene oxide,

and exhibited the lowest electrolyte diffusion resistance and the highest electrocatalytic activity. The DSSC with $\text{CoS}_2/\text{G}_{50}$ CE achieved a PCE of 6.55%, higher than bare CoS_2 or graphene CEs or a conventional Pt CE ($\eta = 6.20\%$). Also, CoS_2 /RGO composite films for a CE of a DSSC were prepared using the layer-by-layer (LbL) assembly method, followed by thermal annealing.²⁴⁰ The photovoltaic parameters of the CoS_2 /RGO CE based DSSCs were found to depend upon the deposition times of graphene oxide. PCE values of 2.6, 4.1, 5.4, 2.9 and 1.4% were measured for 2, 4, 6, 8 and 10 deposition times of graphene oxide, respectively. It appeared that the lowest R_{CT} of 4.8 Ωcm^2 was observed for a CoS_2 /RGO CE prepared with 6 deposition times.

3.7 SnS_2 counter electrodes

Tin disulfide (SnS_2) attains morphological structures which include nanocrystals, nanosheets, nanowires, nanobelts, and these show potential for field-effect transistors, gas sensors, photocatalysts, and solar cells.^{241–248} In one study, semi-transparent SnS_2 nanosheets were prepared as a CE to develop a Pt-free DSSC for the reduction of I_3^- .²⁴⁹ The SnS_2 -based CE with 300 nm thickness showed high electrocatalytic activity, with a PCE of 7.64% compared to a PCE of 7.71% for a Pt CE based DSSC. When SnS_2 nanosheets were functionalized with carbon nanoparticles, the CE exhibited a PCE of 8.06%, a better electrocatalytic performance than a Pt CE. SnS_2 nanosheets could therefore be used as a low cost electrocatalytic electrode material for DSSCs. Yang *et al.*²⁵⁰ prepared SnS_2 nanoparticles and a RGO nanocomposite as a Pt-free CE for a DSSC. The SnS_2 nanoparticles dispersed onto RGO sheets exhibited improved electrocatalytic activity for reducing I_3^- , and also increased conductivity. Fig. 18 illustrates the preparation of SnS_2 @RGO nanocomposites and compares J – V curves for DSSCs having Pt, RGO, SnS_2 , and SnS_2 @RGO composite CEs. The DSSC with SnS_2 @RGO nanocomposite CE showed a PCE of 7.12%, much higher than that of the RGO sheet alone (3.73%) and SnS_2 nanoparticles (5.58%), and a comparable PCE value to Pt CE (6.79%). The Z_N values were 0.64, 4.36, 5.01 and 0.95 Ω for the

Table 3 Photovoltaic parameters of WS_2 , NiS_2 , TiS_2 , FeS_2 , CoS_2 , and SnS_2 based CEs used in DSSCs. FTO glass is the common substrate used in assembling DSSCs with different CE materials. The measurements were conducted at a simulated solar light intensity of 100 mW cm^{-2} (AM 1.5G) unless specified. The photovoltaic parameters short-circuit photocurrent density (J_{sc}), open-circuit voltage (V_{oc}), fill factor (FF), and power conversion efficiency (η), series resistance (R_s), charge-transfer resistance (R_{CT}), electrolyte and dye used for DSSCs are summarized and compared with standard Pt counter electrode^a

Counter electrodes	Redox couples	Dye	J_{sc} (mA cm^{-2})	V_{oc} (V)	FF (%)	PCE (η , %)	R_s ($\Omega \text{ cm}^2$)	R_{CT} ($\Omega \text{ cm}^2$)	Ref.
WS_2	I^-/I_3^-	N719	12.1	0.662	55	4.4	—	—	181
WS_2 (glucose solution, 0.3 M)	I^-/I_3^-	N719	12.8	0.658	63	5.3	—	—	181
WS_2 (glucose solution, 0.6 M)	I^-/I_3^-	N719	13.1	0.670	62	5.5	—	—	181
WS_2 (glucose solution, 1.2 M)	I^-/I_3^-	N719	12.4	0.675	63	5.3	—	—	181
Pt reference	I^-/I_3^-	N719	13.2	0.668	63	5.6	—	—	181
WS_2 (sputtering time, 10 min)	I^-/I_3^-	N719	13.43	0.71	66	6.3	—	—	182
WS_2 (sputtering time, 15 min)	I^-/I_3^-	N719	15.01	0.69	55	5.8	—	—	182
Pt reference	I^-/I_3^-	N719	16.50	0.66	61	6.8	—	—	182
WS_2 (hydrothermal method)	I^-/I_3^-	N719	11.28	0.72	59	4.79	4.86	5.13	185
WS_2/MWCNTs (3 wt%)	I^-/I_3^-	N719	12.65	0.73	59	5.45	3.75	3.47	185
WS_2/MWCNTs (5 wt%)	I^-/I_3^-	N719	13.51	0.73	65	6.41	3.01	2.53	185
WS_2/MWCNTs (10 wt%)	I^-/I_3^-	N719	12.09	0.72	60	5.22	4.17	4.59	185
MWCNTs	I^-/I_3^-	N719	10.77	0.66	61	4.34	6.52	6.60	185
Pt reference	I^-/I_3^-	N719	13.23	0.74	67	6.56	2.26	2.74	185
WS_2 (hydrothermal method)	I^-/I_3^-	N719	11.72	0.72	63	5.32	2.86	4.60	186
WS_2/MWCNTs (1 wt%)	I^-/I_3^-	N719	11.95	0.73	63	5.50	2.80	3.86	186
WS_2/MWCNTs (5 wt%)	I^-/I_3^-	N719	13.63	0.75	72	7.36	2.54	2.49	186
WS_2/MWCNTs (7 wt%)	I^-/I_3^-	N719	12.75	0.75	68	6.50	2.67	2.94	186
WS_2/MWCNTs (10 wt%)	I^-/I_3^-	N719	12.47	0.74	68	6.27	2.78	3.46	186
WS_2/MWCNTs^*	I^-/I_3^-	N719	12.65	0.73	59	5.45	2.85	3.47	186
MWCNTs	I^-/I_3^-	N719	10.77	0.66	61	4.34	2.95	6.60	186
Pt reference	I^-/I_3^-	N719	13.23	0.76	75	7.54	2.27	2.74	186
TiS_2 nanosheets	I^-/I_3^-	N719	17.48	0.73	60.3	7.66	—	—	199
TiS_2 /graphene hybrid	I^-/I_3^-	N719	17.76	0.72	68.5	8.80	2.32	0.63	199
Graphene	I^-/I_3^-	N719	15.41	0.71	48.4	5.33	—	—	199
Pt reference	I^-/I_3^-	N719	16.93	0.72	65.6	8.00	6.90	1.32	199
TiS_2 (drop coating method)	I^-/I_3^-	N719	11.27	0.565	51	3.24	16.12	—	200
$TiS_2/\text{PEDOT:PSS}$ (5 wt%)	I^-/I_3^-	N719	13.81	0.686	62	5.91	—	—	200
$TiS_2/\text{PEDOT:PSS}$ (10 wt%)	I^-/I_3^-	N719	15.78	0.681	66	7.04	15.78	4.78	200
PEDOT:PSS	I^-/I_3^-	N719	12.74	0.664	46	3.91	14.92	7.27	200
Pt reference	I^-/I_3^-	N719	15.83	0.716	68	7.65	14.29	3.02	200
NiS_2 –hollow microspheres	I^-/I_3^-	N719	17.48	0.712	63	7.84	10.56	9.68	206
Pt reference	I^-/I_3^-	N719	17.04	0.747	62	7.89	12.78	8.76	206
NiS_2 –octahedron	I^-/I_3^-	N719	13.55	0.712	62	5.98	13.14	9.86	209
NiS_2 –cube	I^-/I_3^-	N719	12.62	0.715	60	5.43	14.98	13.17	209
Pt reference	I^-/I_3^-	N719	14.37	0.718	63	6.55	2.24	6.25	209
NiS_2 (hydrothermal method)	I^-/I_3^-	N719	14.42	0.738	66	7.02	5.1	8.8	210
NiS_2/RGO	I^-/I_3^-	N719	16.55	0.749	69	8.55	6.4	2.9	210
Reduced graphene oxide (RGO)	I^-/I_3^-	N719	10.98	0.716	40	3.14	14.2	100.2	210
Pt reference	I^-/I_3^-	N719	15.75	0.739	70	8.15	2.2	0.5	210
FeS_2 (spray pyrolysis)	I^-/I_3^-	N719	15.20	0.79	65	7.97	—	—	221
Pt reference	I^-/I_3^-	N719	14.77	0.78	66	7.54	—	—	221
FeS_2	Co^{2+}/Co^{3+}	C128	11.57	0.78	69	6.34	4.9	7.2	221
PEDOT	Co^{2+}/Co^{3+}	C128	10.83	0.79	75	6.31	6.0	3.9	221
FeS_2 films	I^-/I_3^-	N719	12.56	0.658	57.8	4.78	9.60	213.1	222
FeS_2 nanorods	I^-/I_3^-	N719	13.68	0.653	65.7	5.88	9.61	11.0	222
Pt reference	I^-/I_3^-	N719	13.36	0.685	68.2	6.23	5.62	9.2	222
FeS_2 (without NaOH)	I^-/I_3^-	N719	10.20	0.70	66	4.76	3.73	13.6	223
FeS_2 (with NaOH)	I^-/I_3^-	N719	12.08	0.74	64	5.78	2.91	5.99	223
Pt reference	I^-/I_3^-	N719	11.58	0.74	69	5.93	3.09	1.16	223
FeS_2 (with ethanedithiol)	I^-/I_3^-	N719	15.14	0.71	68	7.31	—	1.60	224
FeS_2 (without ethanedithiol)	I^-/I_3^-	N719	12.63	0.71	64	5.74	—	4.45	224
Pt reference	I^-/I_3^-	N719	15.37	0.71	69	7.52	—	1.47	224
FeS_2 (MWCNT/TiO ₂ photoanode)	I^-/I_3^-	N719	16.86	0.77	56	7.27	—	—	225
FeS_2 (TiO ₂ photoanode)	I^-/I_3^-	N719	15.16	0.77	57	6.65	—	—	225
Pt (MWCNT/TiO ₂ photoanode)	I^-/I_3^-	N719	15.96	0.77	57	7.00	—	—	225
Pt (TiO ₂ photoanode)	I^-/I_3^-	N719	15.68	0.77	54	6.51	—	—	225
CoS_2 nanocrystals	I^-/I_3^-	N719	14.62	0.71	64	6.78	34.20	7.21	232
Pt reference	I^-/I_3^-	N719	14.78	0.72	68	7.38	27.13	4.57	232



Table 3 (Contd.)

Counter electrodes	Redox couples	Dye	J_{sc} (mA cm $^{-2}$)	V_{oc} (V)	FF (%)	PCE (η , %)	R_s (Ω cm 2)	R_{CT} (Ω cm 2)	Ref.
Co ₃ S ₄ nanotube (NT1)	I $^-$ /I ₃ $^-$	N719	5.26	0.765	52.5	2.13	—	—	233
Co ₃ S ₄ nanotube (NT2)	I $^-$ /I ₃ $^-$	N719	10.68	0.794	64.6	5.48	—	—	233
Co ₃ S ₄ nanotube (NT3)	I $^-$ /I ₃ $^-$	N719	11.70	0.797	65.5	6.11	—	—	233
Co ₃ S ₄ nanotube (NT4)	I $^-$ /I ₃ $^-$	N719	11.58	0.804	65.8	6.13	—	—	233
Pt reference	I $^-$ /I ₃ $^-$	N719	12.28	0.770	63.9	6.04	—	—	233
Co ₃ S ₄ nanoflakes	I $^-$ /I ₃ $^-$	N719	10.13	0.747	68.8	5.20	—	—	234
Pt reference	I $^-$ /I ₃ $^-$	N719	10.04	0.767	69.4	5.34	—	—	234
CoS(50) (chloroform, 50 mM)	I $^-$ /I ₃ $^-$	N3	8.48	0.703	53.1	3.4	—	—	235
CoS(25) (chloroform, 25 mM)	I $^-$ /I ₃ $^-$	N3	9.23	0.700	51.3	3.5	—	—	235
CoS(25)A (annealed for 240 min)	I $^-$ /I ₃ $^-$	N3	3.86	0.560	23.2	0.5	—	—	235
CoS(12.5) (chloroform, 12.5 mM)	I $^-$ /I ₃ $^-$	N3	6.08	0.701	54.1	2.3	—	—	235
CoS(2.5) (chloroform, 2.5 mM)	I $^-$ /I ₃ $^-$	N3	4.32	0.700	47.9	1.4	—	—	235
Pt reference	I $^-$ /I ₃ $^-$	N3	9.05	0.702	56.4	3.6	—	—	235
CoS(25) (chloroform, 25 mM)	I $^-$ /I ₃ $^-$	N719	14.15	0.703	66.7	6.6	—	—	235
Pt reference	I $^-$ /I ₃ $^-$	N719	13.90	0.692	62.4	6.0	—	—	235
Co ₃ S ₄ rose-petal structure	I $^-$ /I ₃ $^-$	N719	12.14	0.64	68	5.32	9.88	3.52	236
Pt reference	I $^-$ /I ₃ $^-$	N719	13.35	0.61	61	5.02	9.09	3.65	236
Co ₃ S ₄ (chemical bath deposition)	I $^-$ /I ₃ $^-$	N719	8.41	0.628	73.6	4.01	12.02	326.6	238
Co ₃ S ₄ (Ni-doped, 15%)	I $^-$ /I ₃ $^-$	N719	12.12	0.649	69.8	5.50	9.21	8.53	238
NiS nanoparticles	I $^-$ /I ₃ $^-$	N719	9.54	0.592	67.8	3.83	—	—	238
Pt reference	I $^-$ /I ₃ $^-$	N719	12.33	0.649	65.0	5.21	10.4	14.18	238
Co ₃ S ₄	I $^-$ /I ₃ $^-$	N719	6.25	0.58	51	1.86	9.7	3.4	239
Co ₃ S ₄ -G ₂₀ (GO powder, 20 mg)	I $^-$ /I ₃ $^-$	N719	14.38	0.71	57	5.86	7.7	2.3	239
Co ₃ S ₄ -G ₅₀ (GO powder, 50 mg)	I $^-$ /I ₃ $^-$	N719	15.12	0.73	60	6.55	7.6	1.3	239
Co ₃ S ₄ -G ₈₀ (GO powder, 80 mg)	I $^-$ /I ₃ $^-$	N719	13.11	0.71	52	4.83	7.9	2.7	239
Graphene	I $^-$ /I ₃ $^-$	N719	3.68	0.65	58	1.37	7.6	4.0	239
Pt reference	I $^-$ /I ₃ $^-$	N719	14.69	0.73	58	6.20	7.2	1.9	239
Co ₃ S ₄ /reduced graphene oxide	I $^-$ /I ₃ $^-$	Z907	12.87	0.67	63	5.4	22.5	4.8	240
SnS ₂ (350 °C, 30 min)	I $^-$ /I ₃ $^-$	N719	15.63	0.725	55.3	6.27	21.5	8.3	249
SnS ₂ (400 °C, 30 min)	I $^-$ /I ₃ $^-$	N719	16.96	0.743	60.7	7.64	18.6	5.6	249
C/SnS ₂ (400 °C, 30 min)	I $^-$ /I ₃ $^-$	N719	17.47	0.745	61.9	8.06	17.4	5.2	249
SnS ₂ (450 °C, 30 min)	I $^-$ /I ₃ $^-$	N719	13.37	0.734	62.6	6.14	20.8	10.6	249
Pt reference	I $^-$ /I ₃ $^-$	N719	16.53	0.730	63.9	7.71	16.2	6.7	249
SnS ₂ @RGO hybrid	I $^-$ /I ₃ $^-$	N719	14.80	0.718	67.02	7.12	17.96	7.24	250
SnS ₂	I $^-$ /I ₃ $^-$	N719	13.60	0.770	53.28	5.58	39.73	11.24	250
RGO	I $^-$ /I ₃ $^-$	N719	10.08	0.661	52.29	3.73	34.20	50.25	250
Pt reference	I $^-$ /I ₃ $^-$	N719	14.00	0.720	67.36	6.79	24.21	5.08	250

^a WS₂/MWCNTs* prepared without glucose aid. In the case of R_s and R_{CT} : some of the authors used Ω instead of Ω cm 2 for the resistances without mentioning the size of the electrode.

SnS₂@RGO nanocomposite, SnS₂, RGO and Pt CEs, respectively. The RGO and SnS₂ CEs have larger R_{CT} values, hence lower electrocatalytic ability among these CEs, whereas the SnS₂@RGO composite has a lower R_{CT} value, leading to a higher electrocatalytic activity. The role of the RGO sheets is to facilitate the conduction pathway. The E_{pp} of the SnS₂@RGO nanocomposite CE is 593 mV, similar to a Pt CE (E_{pp} of 605 mV). This indicates that the electrocatalytic activity of the SnS₂@RGO nanocomposite CE is similar to that of a conventional Pt CE. The electrochemical stability of the SnS₂@RGO nanocomposite CE was analyzed up to 25 cycles of CV curves, where no drastic change was noticed in peak current density, confirming that SnS₂@RGO nanocomposite CEs are stable for electrocatalysis of I₃ $^-$ in the electrolyte. The SnS₂@RGO nanocomposite CEs are as promising as Pt CEs in DSSCs. Table 3 lists a summary of the photovoltaic parameters of WS₂, NiS₂, TiS₂, FeS₂, CoS₂, and SnS₂ based CEs for DSSCs and their comparison with a standard Pt CE.

4. Transition-metal diselenides based counter electrodes

4.1 MoSe₂ counter electrodes

Molybdenum dichalcogenides, such as MoS₂, MoSe₂, and MoTe₂, are a very interesting class of materials that has attracted a great attention because of their unique properties.²⁵¹⁻²⁵⁷ Molybdenum diselenide (MoSe₂) is a semiconductor that has been studied for device applications.^{92,258,259} The nanosheets of MoSe₂ have weak van der Waals forces, therefore, poorly adhere to the surface of substrates. To resolve this problem, Lee *et al.*²⁶⁰ and Chen *et al.*²⁶¹ applied a CVD technique to grow catalytic MoSe₂ films on Mo foils. Lee *et al.*²⁶⁰ used few-layer MoSe₂ in a DSSC as CE for the reduction of I₃ $^-$ to I $^-$. Fig. 19 shows a schematic representation for the preparation of few-layer MoSe₂, and their SEM and TEM images. The few-layer MoSe₂ on Mo film was developed by selenizing the Mo-coated soda-lime glass in a tube furnace. X-ray diffraction analysis exhibits



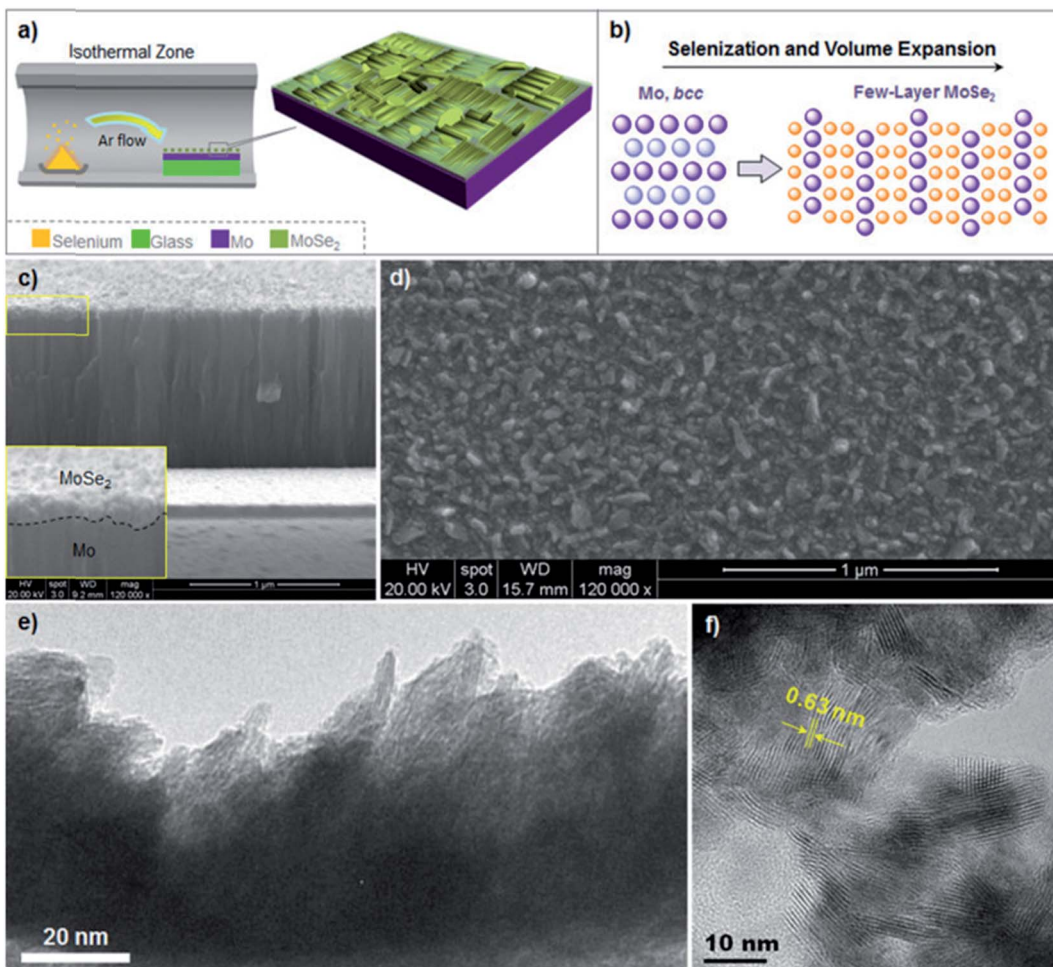


Fig. 19 (a) Schematic representation for the selenization of Mo-coated soda-lime glass in a tube furnace for few-layer MoSe₂; (b) schematic illustration showing the formation of few-layer MoSe₂ from body-centered cubic (bcc) crystal structures of Mo (c) cross-sectional SEM image of the MoSe₂ on Mo surface, inset shows the borderline between MoSe₂ and Mo substrate; (d) SEM image of the as-synthesized MoSe₂ nanostructures; (e) HRTEM image of the few-layer MoSe₂; (f) high magnification HRTEM image of the few-layer MoSe₂ with interlayer spacing of 0.63–0.64 nm. Reprinted with permission from ref. 260, L. T. L. Lee, J. He, B. Wang, Y. Ma, K. Y. Wong, Q. Li, X. Xiao and T. Chen, few-layer MoSe₂ possessing high catalytic activity towards iodide/tri-iodide redox shuttles. *Sci. Rep.*, 2014, 4, 4063–4069. Copyright © Nature Publishing Group.

body-centered cubic (bcc) crystal structures of the Mo film. The Mo film thickness was 1 μm and selenization was performed at 550 °C for 5 minutes, and produced the best performance for the DSSC. The MoSe₂ layer was about 70 nm as confirmed by the cross-sectional SEM image. The surface of the selenized Mo/glass contains nanoparticles, and the HRTEM image shows the few-layer structures. The interlayer spacing was measured as 0.63–0.64 nm. The few-layer MoSe₂ was prepared by surface selenization of Mo-coated soda-lime glass, which yielded a PCE of 9.0%, compared to a PCE of 8.68% for the Pt/FTO-based photoanode, thus showing the Pt/FTO free MoSe₂ CE outperformed the conventional CE. An MoS₂/Mo combination as a CE in a DSSC shows a PCE of 8.69%. Fig. 20 shows a comparison of *J-V* curves of the DSSCs having MoSe₂/Mo and MoS₂/Mo CEs with different temperatures and times of selenization and sulfurization, and the Pt/FTO CE. The PCE of the DSSCs decreased from 7.14% for MoSe₂ CEs selenized at 580 °C

for 60 minutes, to a PCE of 4.26% for 120 minutes. The edge sites were also found to be important for the high catalytic activity. The Mo substrate plays an important role in significantly reducing the sheet resistance of the CE, which eventually leads to a high DSSC performance. The low sheet resistance of 0.29 Ωsq^{-1} for MoSe₂/Mo, compared to 12.60 Ωsq^{-1} for Pt/FTO, indicates that MoSe₂/Mo is better as a CE in a DSSC than a Pt/FTO. The R_{CT} of 0.87 Ωcm^2 for MoSe₂ and 0.61 Ωcm^2 for MoS₂ is lower compared to Pt (6.26 Ωcm^2) due to high conductivity of the Mo substrate, therefore the Mo substrate seems superior to the FTO substrate. Chen *et al.*²⁶¹ also used a MoSe₂/Mo based CE in a DSSC to develop a Pt/FTO-free CE, which showed a PCE of 8.13%, slightly higher than the Pt/FTO CE (PCE of 8.06%). The R_s and R_{CT} values of the MoSe₂/Mo CEs were found to be 16.5% and 3.35% of the Pt/FTO CE, indicating a higher electrocatalytic activity of the MoSe₂/Mo.



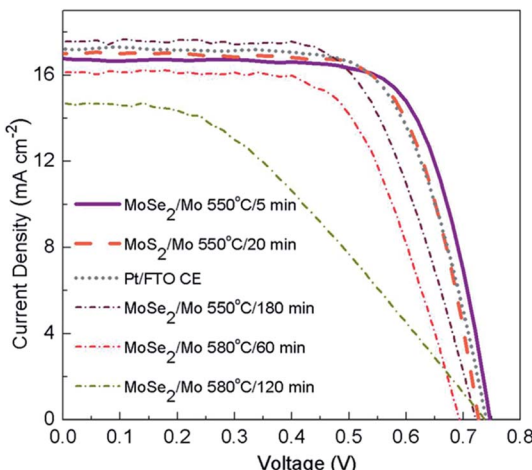


Fig. 20 Photocurrent density–voltage (J – V) curves of DSSCs having MoSe_2/Mo and MoS_2/Mo counter electrodes with different temperatures and time of selenization and sulfurization and a comparison with conventional Pt/FTO counter electrodes. Reprinted with permission from ref. 260, L. T. L. Lee, J. He, B. Wang, Y. Ma, K. Y. Wong, Q. Li, X. Xiao and T. Chen, few-layer MoSe_2 possessing high catalytic activity towards iodide/tri-iodide redox shuttles. *Sci. Rep.*, 2014, 4, 4063–4069. Copyright © Nature Publishing Group.

Thin films of the metal selenides NiSe_2 , CoSe_2 , and MoSe_2 were used as CEs for DSSCs for I_3^- reduction by Ji *et al.*²⁶² NiSe_2 was found to be equally efficient to conventional Pt CEs. In comparison, NiSe_2 also showed a higher PCE than its sulfide analog (NiS_2) due to lower resistance to charge transfer. Fig. 21 shows SEM images of NiSe_2 , CoSe_2 , and MoSe_2 , and Tafel polarization curves and J – V curves of the metal selenides NiSe_2 , CoSe_2 , MoSe_2 , WSe_2 , Bi_2Se_3 , MnSe , PbSe , as well as Pt based CEs used in DSSCs. The metal selenides were deposited on FTO glass. The NiSe_2 , CoSe_2 , and MoSe_2 showed higher exchange current densities compared to other selenides. The J – V curve measurements of the DSSCs indicated better performance of the NiSe_2 CE than that of the Pt CE, however the performance of DSSCs having CoSe_2 and MoSe_2 CEs was lower compared to the Pt CE.

In another study, MoSe_2 nanosheets were prepared using a solvothermal method which shows microsphere hierarchical architecture.²⁶³ MoSe_2 nanosheets used as CE in fabricating a DSSC device showed a PCE of 9.80%, exceeding the PCE of a Pt CE based DSSC ($\eta = 8.17\%$) for the triiodide/iodide (I_3^-/I^-) redox reaction. Bi *et al.*²⁶⁴ anchored fullerene-structured MoSe_2 hollow spheres on highly nitrogen-doped graphene (HNG) as a CE for a DSSC. Diethylenetriamine (DETA) was used as a dopant for nitrogen of graphene. The hollow spheres consisted of 12–15 layers of MoSe_2 which formed the conductive network for facilitating rapid electron transfer in the DSSC. The MoSe_2 hollow spheres of 60–100 nm diameter and 8–12 nm thickness were dispersed on a HNG surface. The HNG– MoSe_2 hybrid has 52.4 wt% of MoSe_2 content. The N content increased from 2.5% in MoSe_2 /graphene hybrid to 12.5% in the HNG– MoSe_2 hybrid, which also showed high stability after 200 consecutive cycles of CV measurements. The HNG– MoSe_2

hybrid CE showed a PCE of 10.01%, slightly lower than a Pt CE ($\eta = 10.55\%$) under similar conditions, while the MoSe_2 /graphene hybrid CE had a PCE of 7.34% arising from a poor fill factor of 0.60.

Composites of MoSe_2 nanosheets (NS) and poly(3,4 ethylenedioxythiophene):poly(styrenesulfonate) were investigated as the CE of a DSSC by Huang *et al.*²⁶⁵ MoSe_2 NS acts as an electrocatalyst, while the PEDOT:PSS plays a role of a conductive binder to facilitate electron transfer between the MoSe_2 and the substrate. The weight ratios of MoSe_2 and PEDOT:PSS (MP) in the composites varied from 0.25 to 2.00. Each composite film contained 50 mg of MoSe_2 powder and 200 mg, 100 mg, 50 mg, and 25 mg of PEDOT:PSS, which are respectively referred to as MP-0.25, MP-0.50, MP-1.00, and MP-2.00, as per the ratios. The DSSC with a MP-1.00 composite film (equal weights of MoSe_2 and PEDOT:PSS) CE exhibits the highest electrocatalytic activity for the reduction of I_3^- . The DSSC containing the MoSe_2 NS/PEDOT:PSS composite film based CE shows a PCE of 7.58%, compared to the Pt CE exhibiting a PCE of 7.81% under similar experimental conditions. When MoSe_2 NS/PEDOT:PSS composite films coated on a titanium (Ti) foil flexible substrate was used as CE, the DSSC showed a PCE of 8.51%, compared to a PCE of 8.21% for the Pt-coated Ti foil CE. The CEs in the DSSCs show the relative order of the electrocatalytic activity as Pt > MP-1.00 > bare MoSe_2 > bare PEDOT:PSS, which is the same as observed by the IPCE spectra. The MP-1.00 composite film shows larger values of the heterogeneous rate constant, and the effective catalytic surface area as compared to bare MoSe_2 and bare PEDOT:PSS, because of MoSe_2 NS contents. The $R_{\text{CT-Tafel}}$ values of $3.23 \Omega \text{ cm}^2$ for Pt, $181.46 \Omega \text{ cm}^2$ for bare PEDOT:PSS, $3.77 \Omega \text{ cm}^2$ for MP-1.00, and $3.11 \Omega \text{ cm}^2$ for bare MoSe_2 were observed. The electrocatalytic ability of the CEs follow a trend seen in the R_{CT} values measured from Tafel polarization curves and EIS. The MoSe_2 NS/PEDOT:PSS composite film based CEs thus show potential to replace a costly Pt electrode.

A cobalt selenide ($\text{Co}_{0.85}\text{Se}$)/ MoSe_2 /molybdenum oxide (MoO_3) ternary hybrid was evaluated as a CE for DSSCs.²⁶⁶ $\text{Co}_{0.85}\text{Se}/\text{MoSe}_2/\text{MoO}_3$ ternary hybrids consist of nanorods, nanosheets, and nanoparticles, as confirmed by FESEM. CV showed larger current density for the $\text{Co}_{0.85}\text{Se}/\text{MoSe}_2/\text{MoO}_3$ hybrid compared with a sputtered Pt CE. The $\text{Co}_{0.85}\text{Se}/\text{MoSe}_2/\text{MoO}_3$ CE based DSSCs showed a PCE of 7.10%, much higher than that of a DSSC with a Pt CE ($\eta = 6.03\%$). For comparison, the $\text{Co}_{0.85}\text{Se}$ hollow nanoparticles as a CE for DSSCs showed a PCE of 6.03%, lower compared to the Pt CE based DSSC ($\eta = 6.45\%$).²⁶⁷ The transparent CEs using metal selenides alloys (M–Se; M = Co, Ni, Cu, Fe, Ru) were studied for the electrocatalytic activity for DSSCs and triiodide (I_3^-) reduction.²⁶⁸ The DSSCs containing CEs consisting of a metal selenide alloy showed PCEs of 8.30% for $\text{Co}_{0.85}\text{Se}$, 7.85% for $\text{Ni}_{0.85}\text{Se}$, 6.43% for $\text{Cu}_{0.50}\text{Se}$, 7.64% for FeSe , and 9.22% for $\text{Ru}_{0.33}\text{Se}$. A Pt CE based DSSC exhibited PCE of 6.18%. Also, a nickel cobalt sulfide (NiCo_2S_4) nanoneedle array²⁶⁹ used as a CE for a DSSC showed a PCE value of 6.9%, which is comparable to a Pt CE ($\eta = 7.7\%$).



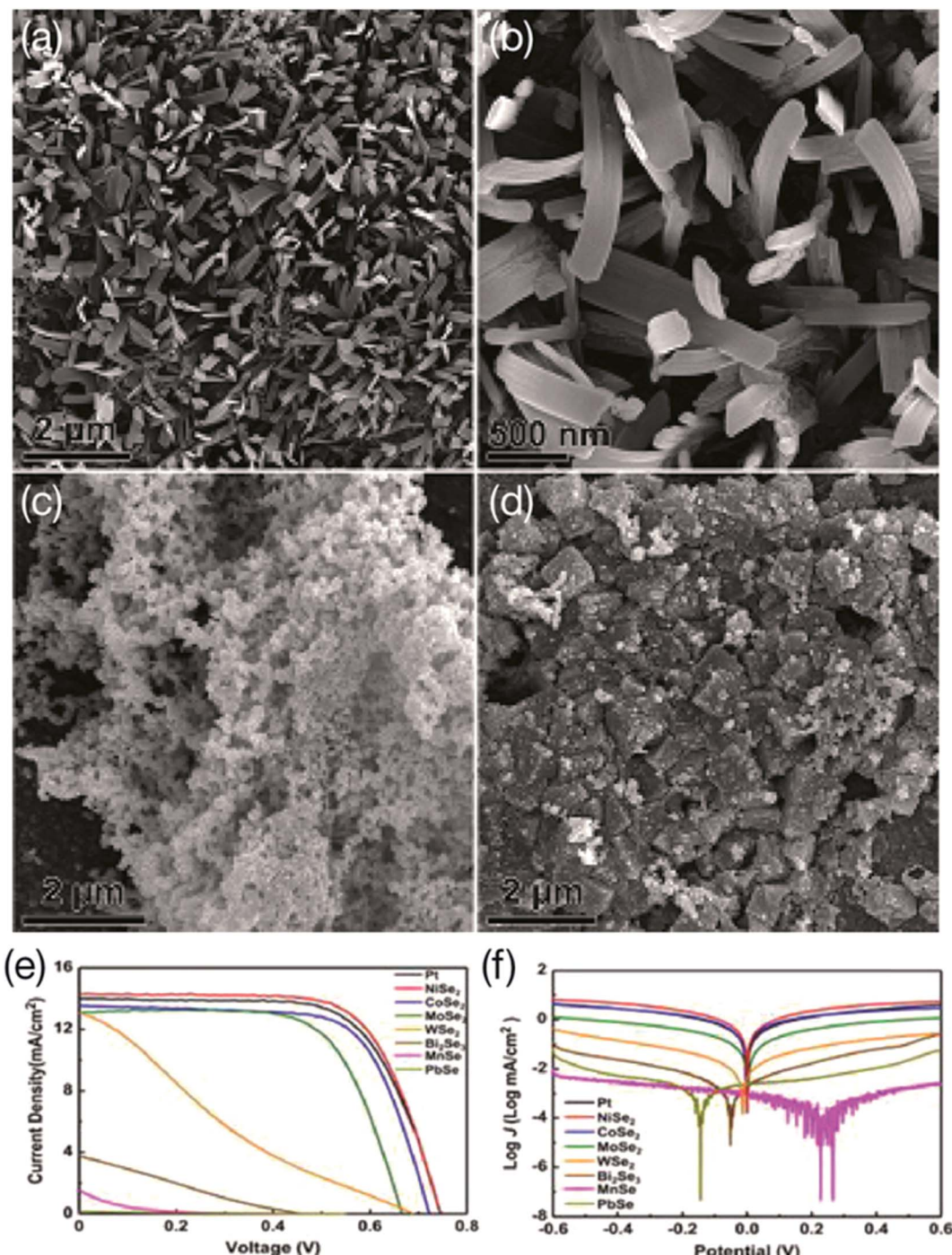


Fig. 21 SEM images of NiSe₂ (a, b) and SEM images of CoSe₂ (c) and MoSe₂ (d). $J-V$ characteristic curves (e) and Tafel polarization curves (f) of DSSCs based on CEs of made of metal selenides; NiSe₂, CoSe₂, MoSe₂, WSe₂, Bi₂Se₃, MnSe, PbSe, and Pt. Reprinted with permission from ref. 262, I. A. Ji, H. M. Choi and J. H. Bang, metal selenide films as the counter electrode in dye-sensitized solar cell. *Mater. Lett.*, 2014, **123**, 51–54. Copyright© Elsevier.

4.2 NbSe₂ counter electrodes

Niobium diselenide (NbSe₂) has attracted attention due to its superconducting properties^{270–275} and can be easily processed into nanosheets, nanoflakes, nanowires and nanotubes usable for applications in field-effect transistors,^{99a} light-emitting diodes,²⁷⁶ superconductors,²⁷⁷ and lithium batteries.²⁷⁸

NbSe₂ nanosheets, nanorods, and NbSe₂/C composites were used as CEs for DSSCs.²⁷⁹ The morphology and structure of the NbSe₂ materials were characterized by SEM, TEM, and XRD while their electrochemical properties were evaluated by CV, EIS, and Tafel polarization curve measurements. The CEs based on NbSe₂ nanorods and NbSe₂ nanosheets showed lower charge

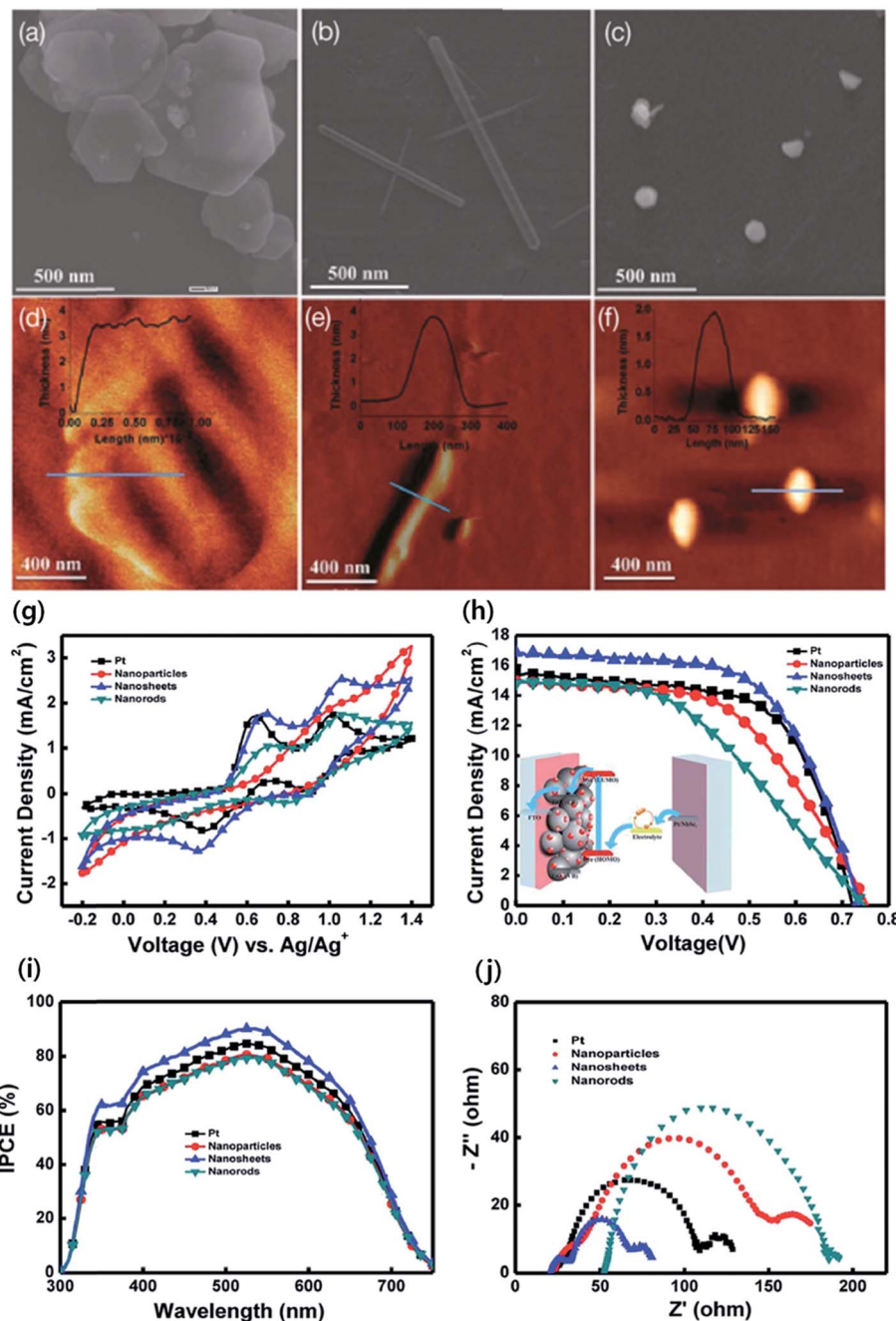


Fig. 22 SEM images of NbSe_2 nanostructures that include nanosheets (a), nanorods (b), and nanoparticles (c). (d–f) AFM height images of NbSe_2 nanosheets (d), nanorods (e), and nanoparticles (f). The insets show height profiles measured by AFM images. (g) Cyclic voltammograms (CV) of Pt CE and NbSe_2 nanostructures based CEs. (h) J – V curves of Pt and NbSe_2 nanostructures. The inset represents DSSC structure with an energy level diagram of the materials. (i) Photon-to-current conversion efficiency (IPCE) curves of Pt and NbSe_2 nanostructures, and (j) EIS Nyquist plots of Pt and NbSe_2 nanostructures based CEs used in DSSCs. Reprinted with permission from ref. 280, M. A. Ibrahim, W. C. Huang, T. W. Lan, K. M. Boopathi, Y. C. Hsiao, C. H. Chen, W. Budiarwan, Y. Y. Chen, C. S. Chang, L. J. Li, C. H. Tsai, C. C. Chu, controlled mechanical cleavage of bulk niobium diselenide to nanoscaled sheet, rod, and particle structures for Pt-free dye-sensitized solar cells. *J. Mater. Chem. A*, 2014, 2, 11382–11390. Copyright© Royal Society of Chemistry.

transfer resistance and ionic diffusion. DSSCs having NbSe_2 nanosheet-based CEs achieved a PCE of 7.34%, which further increased to 7.80% for the NbSe_2/C composite-based CEs due to reduced series resistance, which is a PCE of 98.7% of the conventional Pt-based CEs ($\eta = 7.90\%$). Also, NbSe_2

nanostructures deposited *via* spray-coating were used to develop Pt-free CEs for DSSCs by Ibrahim *et al.*²⁸⁰ Fig. 22 shows SEM images and AFM height profiles of NbSe_2 nanosheets, nanorods, and nanoparticles, CV, J – V curves, IPCE spectra, and EIS (presented in Nyquist plots) of Pt and NbSe_2 nanostructures

based CEs used in DSSCs. The morphology of the synthesized NbSe_2 nanostructures was analyzed by SEM and AFM techniques. SEM analysis indicated the pristine NbSe_2 2D sheets were 100 μm thick. The separate NbSe_2 nanosheets were between 100–500 nm in lateral dimension. The length of NbSe_2 nanorods were up to 1.2 μm with diameters ranging between 20 to 100 nm. The average size of the NbSe_2 nanoparticles was between 50–100 nm. The AFM images revealed an average thickness of <8 nm for the NbSe_2 nanosheets, <5 nm for the NbSe_2 nanorods, and <3 nm for the NbSe_2 nanoparticles. HRTEM of the NbSe_2 nanosheets on their edge showed a spacing of 6.3 \AA . HRTEM revealed the crystalline nature of individual NbSe_2 nanorods and nanoparticles. The NbSe_2

nanosheets, nanorods and nanoparticles were studied as CEs in DSSCs as a replacement to a conventional Pt CE. The dye-absorbed TiO_2 electrodes were prepared by dipping electrodes into ruthenium dye 719 solution for 24 hours at room temperature. The dye solution contained 0.5 mM dye N719, [*cis*-di(thiocyanato)-*N*-N0-*bis*(2,20-bipyridyl-4-carboxylic acid-40-tetrabutyl-ammonium carboxylate) ruthenium(II)], and 0.5 mM chenodeoxycholic acid in a 1 : 1 mixture of *tert*-butanol and acetonitrile. The electrolyte solution was composed of 1-butyl-3-methylimidazolium iodide (BMII, 0.6 M), 4-*tert*-butylpyridine (0.5 M), iodine (0.03 M), and guanidinium thiocyanate (0.1 M) in a acetonitrile–valeronitrile mixture. The NbSe_2 nanosheet CEs achieved a PCE of 7.73%, compared to a PCE of 7.01% for

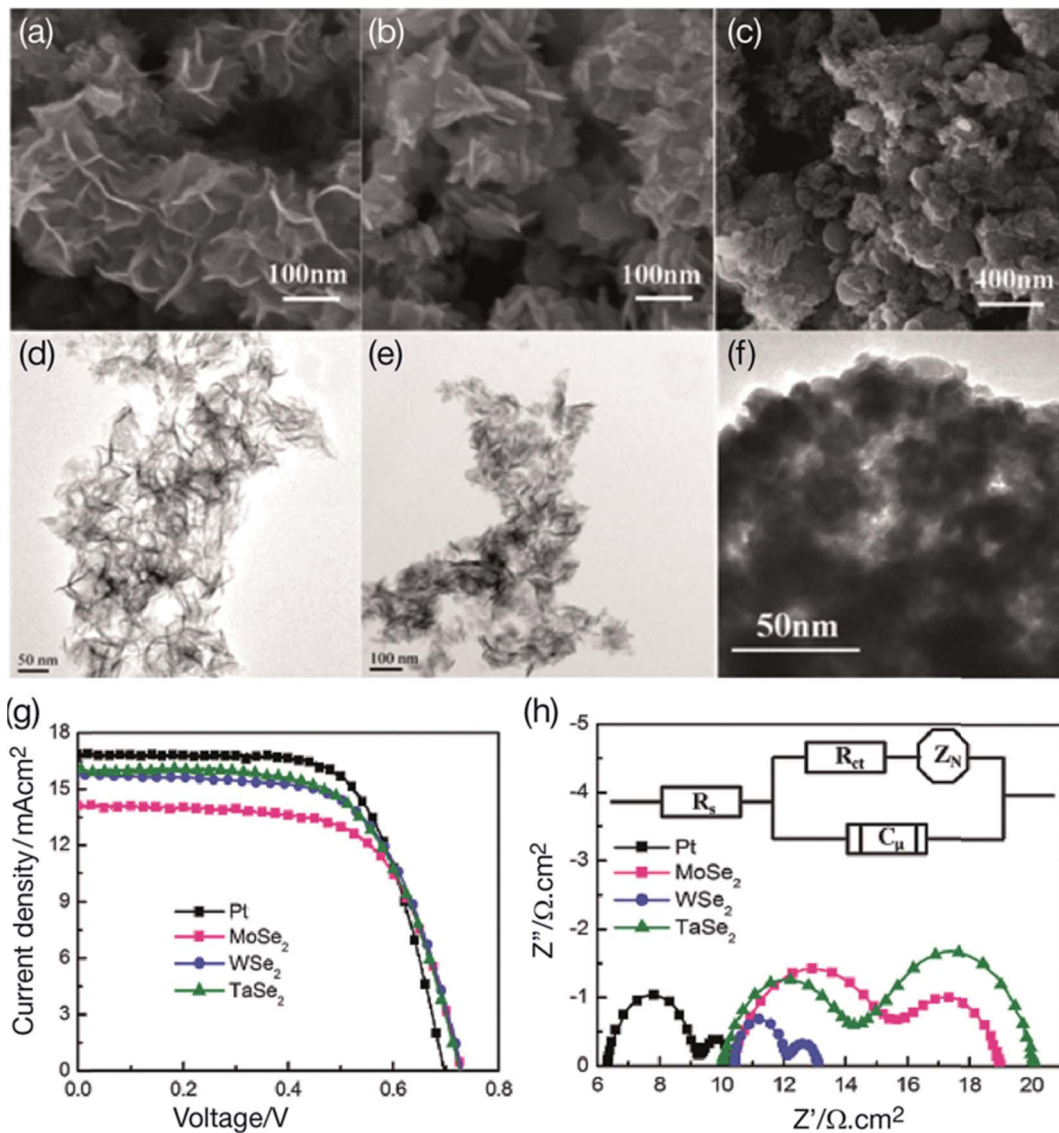


Fig. 23 SEM and TEM images of MoSe_2 (a and d), WSe_2 (b and e), and TaSe_2 (c and f). (g) Photocurrent–voltage (J – V) curves of the DSSCs based on MoSe_2 , WSe_2 , and Pt CEs, measured under simulated sunlight illumination (100 mW cm^{-2} , 1.5 AM G). (h) Nyquist plots of electrochemical impedance spectroscopy (EIS) measurements for DSSCs fabricated with two identical electrodes in the triiodide/iodide (I_3^-/I^-) redox couple in the electrolyte. The inset represents equivalent circuit of DSSCs for fitting Nyquist plots. Reprinted with permission from ref. 281, J. Guo, S. Liang, Y. Shi, C. Hao, X. Wang and T. Ma, transition metal selenides as efficient counter-electrode materials for dye-sensitized solar cells. *Phys. Chem. Chem. Phys.*, 2015, **17**, 28985–28992. Copyright © Royal Society of Chemistry/Owner Societies.



Pt-based CEs for DSSCs. The DSSCs with NbSe_2 nanoparticles and nanorods based CEs show PCE values of 6.27% and 5.05%, respectively, due to low FF arising from relatively smaller surface areas, as well as low exposure on the FTO glass substrates. DSSCs having NbSe_2 nanosheets based CE show the best IPCE spectral response, where the peak increases from 84% for a Pt CE to 89% for a NbSe_2 nanosheets based CE. On the other hand, lower IPCE peak values were observed for NbSe_2 nanoparticles and nanorods based CEs. The charge-transfer processes at the interface of TiO_2 /dye/electrolyte were analyzed by EIS. The NbSe_2 nanosheet based CEs for the DSSCs shows a middle-frequency semicircle, implying it had the highest electro-catalytic activity for the reduction of triiodide ions (I_3^-), and efficient generation of electrons, therefore, occurring of larger electrons at the TiO_2 /dye/electrolyte interface. This study suggests that NbSe_2 nanosheets could be used as alternative CEs to conventional Pt CEs in DSSCs because of their large surface area.

4.3 TaSe_2 counter electrodes

Three transition-metal selenides (MoSe_2 , WSe_2 , and TaSe_2) were prepared by Guo *et al.*²⁸¹ and compared as potential CEs for fabricating DSSC devices using a solvothermal method. These transition-metal selenides show high electrocatalytic activity for the reduction of triiodide (I_3^-), except for MoSe_2 , due to low adsorption and charge-transfer. Fig. 23 shows SEM and TEM images of MoSe_2 (a and d), WSe_2 (b and e), and TaSe_2 ; the Nyquist plots of EIS measurements recorded at -0.75 V bias of the DSSCs based on MoSe_2 , WSe_2 , and Pt CEs for the triiodide/iodide (I_3^-/I^-) redox couple in the electrolyte; and their J - V curves measured under simulated sunlight illumination. The MoSe_2 nanosheets had thickness of about 10 nm with lateral dimensions ranging 100–150 nm. WSe_2 consists of interlaced nanoplates with 15 nm average thickness and a width varying between 60 and 100 nm. The SEM image of TaSe_2 shows fluffy nanoparticles with a wide size distribution. The HRTEM images of MoSe_2 , WSe_2 , and TaSe_2 indicated spacings of 0.282 nm, 0.283 nm, and 0.291 nm, respectively. The WSe_2 shows a pore size distribution (PSD) curve at about 43 nm, MoSe_2 at 30 nm, and TaSe_2 at 10 nm. The mesoporous structure of WSe_2 facilitates the adsorption of triiodide (I_3^-) and transport during the electrocatalytic activity. The BET surface areas were 95.6, 104.4 and 78.8 $\text{m}^2 \text{g}^{-1}$, and the total pore volumes were 0.32 $\text{cm}^3 \text{g}^{-1}$, 0.41 $\text{cm}^3 \text{g}^{-1}$ and 0.14 $\text{cm}^3 \text{g}^{-1}$, for WSe_2 , MoSe_2 , TaSe_2 , respectively. The significant difference in BET surface area and the pore size distribution led to different adsorption properties and electrocatalytic activity of the DSSCs. The R_{CT} of the transition-metal selenides at the electrolyte/electrode interface indicates the level of electrocatalytic activity. The R_{CT} value of $0.78 \Omega \text{cm}^2$ for the WSe_2 CE is smaller compared with a Pt CE ($1.32 \Omega \text{cm}^2$) and a TaSe_2 ($1.89 \Omega \text{cm}^2$) CE, while the R_{CT} value of the MoSe_2 ($2.43 \Omega \text{cm}^2$) CE was larger than that of the Pt CE. Therefore, WSe_2 shows better electrocatalytic activity for triiodide (I_3^-) reduction. The ionic Z_N value of WSe_2 is $1.15 \Omega \text{cm}^2$, lower than that of the MoSe_2 , and TaSe_2 CEs, and comparable to the Pt CE, which demonstrates a larger diffusion coefficient for

triiodide (I_3^-) within the CEs. The conductivities measured by linear sweep voltammetry decrease in the relative order $\text{TaSe}_2 > \text{MoSe}_2 > \text{WSe}_2$. The DSSCs based on TaSe_2 and WSe_2 CEs showed larger J_{sc} than that of MoSe_2 CE. WSe_2 has larger pores and high electrocatalytic activity suitable for fast regeneration and transfer of triiodide (I_3^-). PCE values of 7.32% for TaSe_2 and 7.48% for WSe_2 were measured, which are comparable to a sputtered Pt CE ($\eta = 7.91\%$). The lower PCE value of 6.70% for MoSe_2 arises from a lower V_{oc} and J_{sc} for the DSSC.

4.4 NiSe_2 counter electrodes

Nickel diselenide (NiSe_2) has been studied as a CE of DSSCs for the reduction of I_3^- , which yielded higher PCE of 8.69% than that of a conventional Pt CE (8.04%) under the same experimental conditions.²⁸² Zhang *et al.*²⁸³ developed two types of NiSe_2 CEs on RGO; namely, microsphere NiSe_2/RGO , and octahedron NiSe_2/RGO through a hydrothermal process. The microsphere NiSe_2/RGO CE exhibited higher electrocatalytic performance than a Pt CE for the reduction of triiodide (I_3^-) because of better carrier transfer induced by graphene nanosheets.

CEs of ternary Ni–Co compounds having different morphological structures such as nanoparticles, nanotubes, nanowires, nanoflakes, follower-like, and urchin-like have been studied for DSSCs.^{284,285} For example, the CE made of flower-like $\text{NiCo}_2\text{S}_4/\text{NiS}$ microspheres²⁸⁶ exhibited a PCE of 8.8%, much higher than a standard Pt CE ($\eta = 8.1\%$). A similar concept was employed by Qian *et al.*²⁸⁷ for developing a very interesting class of CEs for DSSCs from nickel cobalt (Ni–Co) selenides having different morphological structures, due to the tuning of the Ni/Co molar ratios. The morphological structure and electrocatalytic performance of ternary Ni–Co selenides was optimized by using different Ni/Co molar ratios. Fig. 24 shows the SEM images of Co_3Se_4 , $\text{Ni}_{0.33}\text{Co}_{0.67}\text{Se}$ precursor, $\text{Ni}_{0.33}\text{Co}_{0.67}\text{Se}$, $\text{Ni}_{0.5}\text{Co}_{0.5}\text{Se}$, $\text{Ni}_{0.67}\text{Co}_{0.33}\text{Se}$, and NiSe , and also shows CV and J - V curves of their DSSCs. The different morphological structures were obtained by tuning the Ni/Co molar ratio, $\text{Ni}_x\text{Co}_{1-x}\text{Se}$, where, x was 0, 0.33, 0.5, 0.67, and 1.0. The 3D dandelion-like precursor of $\text{Ni}_{0.33}\text{Co}_{0.67}\text{Se}$ assembled into nanotubes having about 100 nm diameter, $\text{Ni}_{0.5}\text{Co}_{0.5}\text{Se}$ into a floccus-like microsphere structure with a diameter of 4 microns, $\text{Ni}_{0.67}\text{Co}_{0.33}\text{Se}$ microspheres compiled into nanosheets, and Co_3Se_4 built up rough-surface nanotubes. The specific surface areas determined from the BET method were 5.0, 10.1, 26.1, 28.9, and $35.6 \text{ m}^2 \text{g}^{-1}$, for NiSe , Co_3Se_4 , $\text{Ni}_{0.5}\text{Co}_{0.5}\text{Se}$, $\text{Ni}_{0.67}\text{Co}_{0.33}\text{Se}$ and $\text{Ni}_{0.33}\text{Co}_{0.67}\text{Se}$, respectively. Among all metal selenides, $\text{Ni}_{0.33}\text{Co}_{0.67}\text{Se}$ has the highest specific surface area, which is favorable for providing more active sites for catalysis and increasing the contact area between its CE and the electrolyte, which results in better electrochemical and photovoltaic properties of its DSSCs. The R_{CT} values of CEs follows the relative order of $\text{NiSe} > \text{Co}_3\text{Se}_4 > \text{Pt} > \text{Ni}_{0.67}\text{Co}_{0.33}\text{Se} > \text{Ni}_{0.5}\text{Co}_{0.5}\text{Se} > \text{Ni}_{0.33}\text{Co}_{0.67}\text{Se}$, which implies that the electrocatalytic activity increases in a reverse order. Thus, NiSe was of the lowest activity and $\text{Ni}_{0.33}\text{Co}_{0.67}\text{Se}$ was of the highest catalytic activity for the reduction of triiodide (I_3^-). Therefore, higher contents of Ni in the Ni–Co selenides CEs are



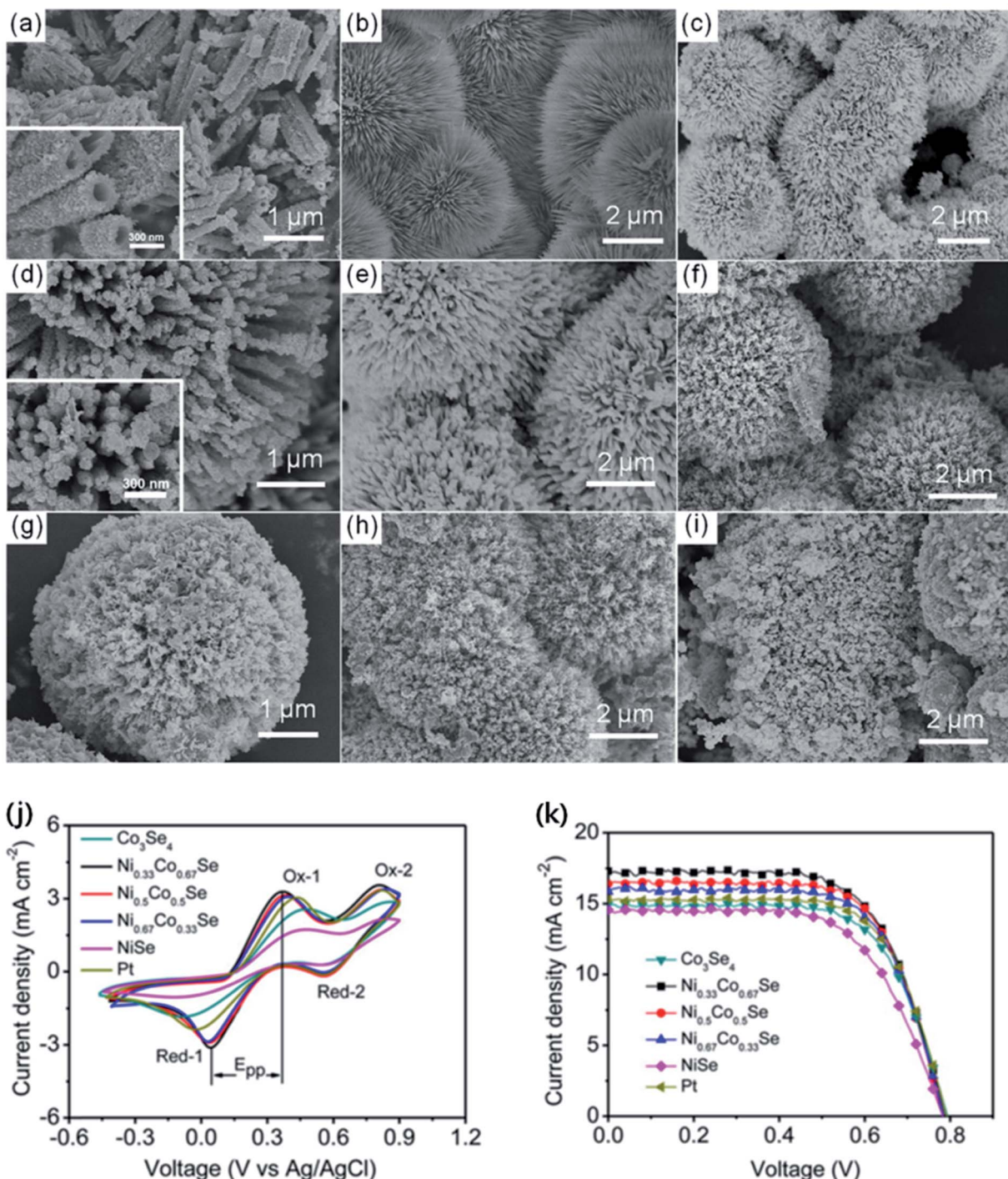


Fig. 24 SEM images of (a) Co_3Se_4 , (b) $\text{Ni}_{0.33}\text{Co}_{0.67}\text{Se}$ precursor, (c–e) $\text{Ni}_{0.33}\text{Co}_{0.67}\text{Se}$, (f and g) $\text{Ni}_{0.5}\text{Co}_{0.5}\text{Se}$, (h) $\text{Ni}_{0.67}\text{Co}_{0.33}\text{Se}$, and (i) NiSe. (j) CVs of DSSCs with Co_3Se_4 , $\text{Ni}_{0.33}\text{Co}_{0.67}\text{Se}$, $\text{Ni}_{0.5}\text{Co}_{0.5}\text{Se}$, $\text{Ni}_{0.67}\text{Co}_{0.33}\text{Se}$, NiSe, and Pt-based CEs at a scan rate of 50 mV s^{-1} . (k) Photocurrent density–voltage (J – V) curves of DSSCs with Co_3Se_4 , $\text{Ni}_{0.33}\text{Co}_{0.67}\text{Se}$, $\text{Ni}_{0.5}\text{Co}_{0.5}\text{Se}$, $\text{Ni}_{0.67}\text{Co}_{0.33}\text{Se}$, NiSe, and Pt CEs under AM 1.5G illumination. Reprinted with permission from ref. 287, X. Qian, H. Li, L. Shao, X. Jiang and L. Hou, morphology-tuned synthesis of nickel cobalt selenides as highly efficient Pt-free counter electrode catalysts for dye-sensitized solar cells. *ACS Appl. Mater. Interfaces*, 2016, 8, 29486–29495. Copyright© American Chemical Society.

not favorable for electrocatalytic activity. The values of cathodic peak current density (red-1) and the E_{pp} can also help understand the electrocatalytic activities of these CEs. The authors noted the following relative order of cathodic peak current

density: NiSe (1.044 mA cm^{-2}) $<$ Co_3Se_4 (1.849 mA cm^{-2}) $<$ Pt (2.373 mA cm^{-2}) $<$ $\text{Ni}_{0.67}\text{Co}_{0.33}\text{Se}$ (2.878 mA cm^{-2}) $<$ $\text{Ni}_{0.5}\text{Co}_{0.5}\text{Se}$ (2.917 mA cm^{-2}) $<$ $\text{Ni}_{0.33}\text{Co}_{0.67}\text{Se}$ (3.120 mA cm^{-2}). They also noted E_{pp} values of NiSe (602 mV) $>$ Co_3Se_4 (565 mV) $>$ Pt (460

mV) > Ni_{0.67}Co_{0.33}Se (365 mV) > Ni_{0.5}Co_{0.5}Se (349 mV) > Ni_{0.33}-Co_{0.67}Se (329 mV), which were in an agreement with EIS measurements of the CEs. The 3D dandelion-like Ni_{0.33}S_{0.67}Se microspheres based CEs exhibited the highest PCE of 9.01%, exceeding that of the Pt CE ($\eta = 8.30\%$). The DSSC with a Co₃Se₄ CE showed a PCE of 7.95%, higher than that of NiSe CE ($\eta = 7.23\%$). These results support the notion that the ternary Ni-Co selenides possess higher electrocatalytic activities and photovoltaic properties than those of binary selenides NiSe and Co₃Se₄ as well as Pt CEs for the triiodide (I₃⁻) reduction, due to their unique morphology and chemical composition.

4.5 FeSe₂ counter electrodes

Iron diselenide (FeSe₂) can be processed into nanosheets, nanocubes, flower-like structures, and nanorods, rod clusters, and microspheres,²⁸⁸⁻²⁹⁴ and has applications in catalysis,²⁹⁵ batteries,^{296,297} and photovoltaic devices.²⁹⁸ The first-row (3d) transition metal dichalcogenides (MX₂) with pyrite structure (where, M = Fe, Co, Ni, and X = S, Se) also exhibit electronic, optoelectronic, and magnetic properties comparable to other TMDs.²⁹⁹⁻³⁰² Huang *et al.*³⁰² used 2D FeSe₂ nanosheets with 7 nm average thickness as a CE for a DSSC. Fig. 25 shows the SEM and TEM images of the synthesized FeSe₂ nanosheets. The thickness of FeSe₂ nanosheets was found to be in the 4–7 nm range, as evaluated by TEM images. High-resolution TEM (HRTEM) indicated the crystalline nature of the nanosheets, having 0.168 nm interplanar spacing. The FeSe₂ nanosheets had specific surface area of 35.02 m² g⁻¹ as calculated by the BET analysis. The FeSe₂ nanosheets exhibit a low charge-transfer resistance (R_{CT}) and a high electrocatalytic activity for triiodide (I₃⁻) reduction in DSSCs. The FeSe₂ nanosheets CE based DSSC showed a PCE of 7.53%, comparable to a Pt CE, while the PCE of FeSe₂ microparticles CE based DSSC was slightly lower (η

= 6.88%). The large surface area of the FeSe₂ nanosheets contributed to a higher PCE by providing more active sites for electrocatalytic activity, as well as a larger electrode/electrolyte interface than that of the FeSe₂ microparticles. The electrochemical stability of the CEs of FeSe₂ nanosheets and Pt were investigated with sequential CV scanning. The current densities of the FeSe₂ CE showed no change after 1000 cycles, confirming corrosion resistance to the electrolyte. The PCEs of FeSe₂ nanosheets under nitrogen protection (N-FeSe₂) and exposure to air for one week (O-FeSe₂) were also studied. The R_{CT} of the N-FeSe₂ CE (0.53 Ω cm²) was much lower than the O-FeSe₂ CE (10.13 Ω cm²) and a Pt CE (1.68 Ω cm²), indicating poorer electrocatalytic activity of the O-FeSe₂ CE compared to the N-FeSe₂ and Pt CEs. The Tafel polarization curves decreased in the order N-FeSe₂ > Pt > O-FeSe₂, having the same order as of exchange current density, CV and EIS measurements. The O-FeSe₂ nanosheets CE based DSSC has a PCE of 6.15%, much lower than that of the N-FeSe₂ ($\eta = 7.53\%$) CE and Pt CE ($\eta = 7.47\%$) under similar conditions.

3D hierarchical FeSe₂ microspheres using a hot-injection method were prepared and studied by Huang *et al.*³⁰³ The morphologies of the FeSe₂ nanomaterials was controlled by the use of alkyl thiols; 1-dodecanethiol (1-DDT) or *tert*-dodecanethiol (*t*-DDT) and their contents were used in synthesis, which varied from irregular FeSe₂ micro/nanoparticles to 3D hierarchical FeSe₂ microspheres and consisted of ultrathin FeSe₂ nanosheets or urchin-like microspheres made of crystalline FeSe₂ nanorods having an average diameter of 650 nm. The FeSe₂ nanomaterials were used as CEs for DSSCs. 3D hierarchical FeSe₂ microspheres made of ultrathin FeSe₂ nanosheets showed the lowest R_{CT} of 0.49 Ω cm² at the electrolyte/electrode interface, a lower Z_N value of 0.39 Ω cm², and faster reaction kinetics for the reduction of I₃⁻ to I⁻ than that of a Pt CE (R_{CT} of 1.15 Ω cm² and Z_N value of 0.91 Ω cm²). R_{CT} values followed the relative order of FeSe₂ microparticles < FeSe₂ nanorods < Pt < FeSe₂ nanosheets, as supported by EIS measurements. A DSSC with a FeSe₂ nanosheets CE exhibited a PCE of 8.39%, slightly better than that of a Pt CE (8.20%) under simulated solar illumination of 100 mW cm⁻² (AM 1.5). FeSe₂ nanorods showed a PCE value of 8.03%, higher than that of FeSe₂ microparticles (7.68%). The PCE value of DSSCs is morphology dependent, where the FeSe₂ nanosheets CE has a high electrocatalytic activity and a larger specific surface area (30.03 m² g⁻¹) than that of FeSe₂ nanorods (19.82 m² g⁻¹). The FeSe₂ nanosheets CE based DSSC retained 99.5% of its initial photocurrent density, compared to 98.3% retained by the Pt CE, after simulated solar illumination of 100 mW cm⁻² for 1 hour, and this indicates better stability of the FeSe₂ nanosheets CE than that of standard Pt CE. Also, the 3D flower-like and sphere-shaped FeSe₂ films were used as CEs for DSSCs.³⁰⁴ The 3D flower-like FeSe₂-based CE exhibited a comparable PCE to a Pt CE ($\eta = 8.00\%$ *versus* 7.87%).

4.6 CoSe₂ counter electrodes

Cobalt diselenide (CoSe₂) has been extensively studied as a catalyst for oxygen reduction reactions.³⁰⁵⁻³⁰⁸ The CoSe₂

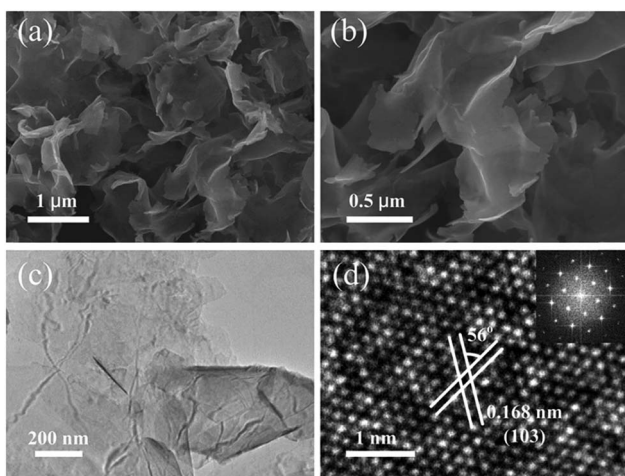


Fig. 25 (a, b) SEM images and (c) TEM image of the as-synthesized FeSe₂ nanosheets, and (d) HRTEM image of a small portion of FeSe₂ nanosheet (inset shows SAED pattern of the FeSe₂ nanosheets). Reprinted with permission from ref. 302, S. Huang, Q. He, W. Chen, Q. Qiao, J. Zai and X. Qian, ultrathin FeSe₂ nanosheets: controlled synthesis and application as a heterogeneous catalyst in dye-sensitized solar cells. *Chem.-Eur. J.*, 2015, 21, 4085–4091. Copyright© Wiley-VCH.



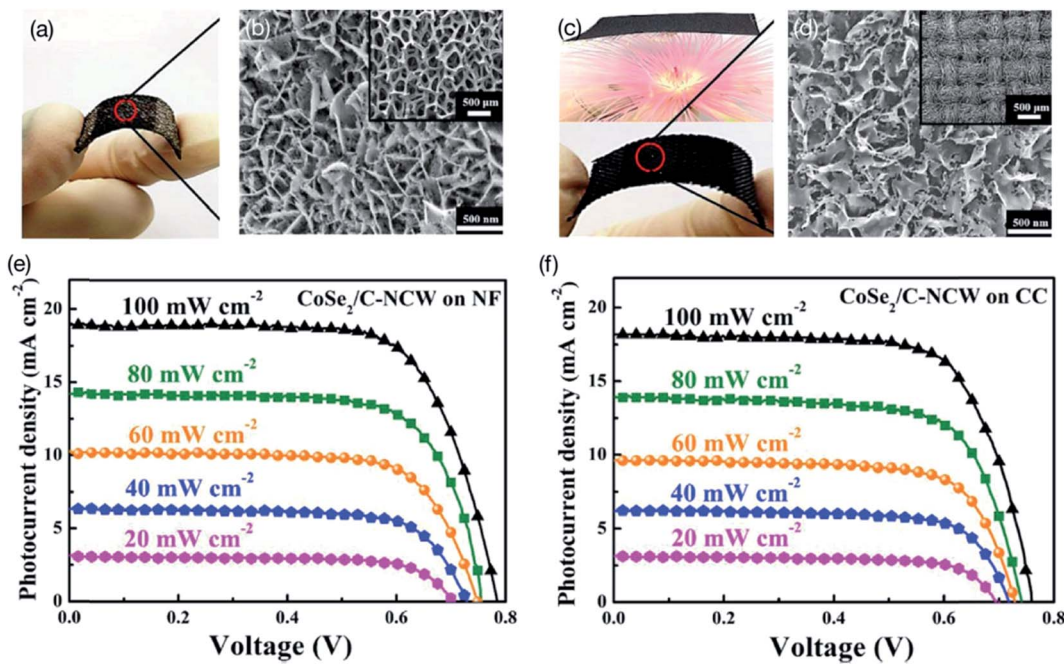


Fig. 26 (a) Photograph of the nickel foam (NF) and (b) SEM image of CoSe₂/C-NCW film on the nickel foam (NF). (c) Photograph of the carbon cloth (CC) and thin CC substrate on a soft flower having needle-like petals and (d) SEM image of CoSe₂/C-NCW film on carbon cloth (CC). Inset shows field-emission scanning electron microscopy (FE-SEM) images in a magnified version. (e) Photocurrent–voltage (*J*–*V*) curves of the DSSCs with CoSe₂/C-NCW on flexible nickel foam (NF) CE, measured at light intensities varying from 20 mW cm^{−2} (0.2 Sun) to 100 mW cm^{−2} (1 Sun). (f) Photocurrent–voltage (*J*–*V*) curves of the DSSCs with CoSe₂/C-NCW on flexible carbon cloth (CC) CE, under similar light intensities. Reprinted with permission from ref. 310, I. T. Chiu, C. T. Li, C. P. Lee, P. Y. Chen, Y. H. Tseng, R. Vittal and K. C. Ho, nanoclimbing-wall-like CoSe₂/carbon composite film for the counter electrode of a highly efficient dye-sensitized solar cell: a study on the morphology control. *Nano Energy*, 2016, 22, 594–606. Copyright © Elsevier.

nanorods synthesized by a hydrothermal method was studied as CEs for DSSCs.³⁰⁹ FESEM revealed a CoSe₂ nanorod morphology of the CoSe₂, which supports carrier transport from the surface of the nanorods to the redox electrolyte. The CoSe₂ CE also exhibited larger current density compared with a Pt CE, as measured by CV. EIS shows an R_s of 8.034 Ω cm² and a low R_{CT} of 0.097 Ω cm² for the CoSe₂ CE. The DSSC with a CoSe₂ CE showed a PCE value of 8.38%, higher than the DSSC based on a Pt CE ($\eta = 7.83\%$), under simulated sunlight illumination of 100 mW cm^{−2} (AM 1.5G).

A comprehensive and detailed study was conducted by Chiu *et al.*³¹⁰ on composite films of CoSe₂/carbon (CoSe₂/C) deposited on FTO substrates having three different morphologies, developed using electro-deposition, followed by an annealing process at 500 °C for 30 minutes in vacuum. In the first stage, three types of CoSe₂/carbon films containing nanowalls were deposited with an electro-deposition process employing different pH baths, while in the second stage, the morphology of the films was transformed after the annealing. The N719 dye-adsorbed TiO₂ film was used as a photoanode for DSSCs. CoSe₂/C films had three different morphologies, including nanograin (NG), nanorock (NR), and nanoclimbing-wall (NCW), which were used as CEs for DSSCs. The electrocatalytic activity of these three CEs was analyzed by CV, RDE, Tafel polarization curves, and EIS, which showed a relative order of CoSe₂/C-NCW > CoSe₂/C-NG > Pt > CoSe₂/C-NR as CEs in the DSSCs, a similar order as was

observed for the R_{CT} values obtained by EIS and Tafel measurements. The CoSe₂/C-NCW showed higher electrical conductivity and a large effective surface area and, therefore, the best electrocatalytic ability for triiodide (I₃[−]) reduction. The DSSCs with CoSe₂/C-NG, CoSe₂/C-NCR, CoSe₂/C-NCW, and Pt CEs exhibited IPCE values between 80–95% in the 400 to 600 nm wavelength region, where the highest IPCE value of 95% was observed for the CoSe₂/C-NCW CE. The DSSC having a CoSe₂/C-NCW CE showed the highest PCE value of 8.92%, even higher than compared with the Pt CE (8.25%). The CoSe₂/C-NCW CEs were electro-deposited onto low-cost, flexible, and highly porous substrates, such as carbon cloth (CC, sheet resistance = 0.63 Ω sq^{−1}) and nickel foam (NF, porosity = 95%, sheet resistance = 0.45 Ω sq^{−1}). Fig. 26 shows photographs of the flexible nickel foam (NF) and carbon cloth (CC), SEM images of CoSe₂/C-NCW film on the flexible NF and CC substrates, and *J*–*V* curves of the DSSCs, with CoSe₂/C-NCW on NF and CC CEs measured at different light intensities (20–100 mW cm^{−2}). The CoSe₂/carbon-NCW CEs shell covered all the minute parts of the carbon cloth and nickel foam core shell structures. The DSSC containing the CE with CoSe₂/C-NCW deposited on nickel foam exhibited the highest PCE of 10.46% at 100 mW cm^{−2} (1 Sun) and 7.90% at 20 mW cm^{−2} (0.2 Sun). The DSSC with the CE of CoSe₂/C-NCW deposited on low-weight carbon cloth showed a PCE of 9.87% at 1 Sun and 7.83% at 0.2 Sun. The low cost and flexible CoSe₂/C-NCW CEs seem to be promising materials to

Table 4 Photovoltaic parameters of MoSe_2 , WS_2 , TaSe_2 , NbSe_2 , FeSe_2 , CoSe_2 and Bi_2Se_3 based CEs for DSSCs. FTO glass is the common substrate used in assembling the DSSCs with different CE materials. The measurements were conducted at a simulated solar light intensity of 100 mW cm^{-2} (AM 1.5G) unless specified. The photovoltaic parameters short-circuit photocurrent density (J_{sc}), open-circuit voltage (V_{oc}), fill factor (FF), and power conversion efficiency (η), series resistance (R_s), charge-transfer resistance (R_{CT}), electrolyte and dye used for DSSCs are summarized and compared with a standard Pt CE^a

Counter electrodes	Redox couple	Dye	J_{sc} (mA cm^{-2})	V_{oc} (V)	FF (%)	PCE (η , %)	R_s (Ωcm^2)	R_{CT} (Ωcm^2)	Ref.
MoSe_2/Mo (<i>in situ</i> sulfurization)	I^-/I_3^-	N719	16.71	0.746	72.2	9.00	1.74	1.39	260
MoS_2/Mo (<i>in situ</i> sulfurization)	I^-/I_3^-	N719	16.95	0.726	70.6	8.69	1.21	5.25	260
Pt reference	I^-/I_3^-	N719	17.19	0.740	68.3	8.68	12.52	0.22	260
MoSe_2/Mo (<i>in situ</i> selenization)	I^-/I_3^-	N719	15.07	0.805	67	8.13	2.64	0.30	261
Pt reference	I^-/I_3^-	N719	16.11	0.794	63	8.06	15.98	8.95	261
NiSe_2	I^-/I_3^-	N719	14.3	0.75	68	7.3	20.9	45.0	262
NiS_2	I^-/I_3^-	N719	14.7	0.72	52	5.5	28.4	50.4	262
CoSe_2	I^-/I_3^-	N719	13.5	0.72	68	6.6	14.8	102.7	262
MoSe_2	I^-/I_3^-	N719	13.0	0.67	68	5.9	16.5	229.8	262
Pt reference	I^-/I_3^-	N719	14.0	0.75	69	7.2	18.5	34.2	262
MoSe_2 (hollow spheres)	I^-/I_3^-	N749	16.06	0.704	38.67	4.46	—	10.24	264
$\text{MoSe}_2/\text{graphene}$ (12.5% N_2 -doped)	I^-/I_3^-	N749	19.73	0.724	70.07	10.01	7.18	3.04	264
$\text{MoSe}_2/\text{graphene}$	I^-/I_3^-	N749	17.12	0.710	60.41	7.34	—	8.49	264
Graphene	I^-/I_3^-	N749	16.67	0.535	54.12	4.83	—	16.27	264
Pt reference	I^-/I_3^-	N749	19.93	0.723	73.22	10.55	7.14	2.81	264
$\text{MoSe}_2/\text{PEDOT:PSS}$	I^-/I_3^-	N719	15.97	0.70	67	7.58	18.08	5.43	265
Pt reference	I^-/I_3^-	N719	16.38	0.74	65	7.81	20.19	4.60	265
$\text{MoSe}_2/\text{PEDOT:PSS@Ti}$	I^-/I_3^-	N719	16.41	0.75	69	8.51	—	—	265
Pt@Ti reference	I^-/I_3^-	N719	16.31	0.74	68	8.21	—	—	265
Bare MoSe_2	I^-/I_3^-	N719	12.65	0.66	28	2.29	20.50	39.74	265
Bare PEDOT:PSS	I^-/I_3^-	N719	9.32	0.67	46	2.90	17.36	190.91	265
$\text{Co}_{0.85}\text{Se}$	I^-/I_3^-	N719	13.41	0.763	62.7	6.42	—	—	266
$3\text{Co}_{0.85}\text{Se}/0.5\text{MoSe}_2/0.5\text{MoO}_3$	I^-/I_3^-	N719	13.43	0.765	65.7	6.75	—	—	266
$2\text{Co}_{0.85}\text{Se}/\text{MoSe}_2/\text{MoO}_3$	I^-/I_3^-	N719	13.80	0.768	67.1	7.10	—	—	266
$\text{Co}_{0.85}\text{Se}/1.5\text{MoSe}_2/1.5\text{MoO}_3$	I^-/I_3^-	N719	13.06	0.760	64.4	6.39	—	—	266
$\text{MoSe}_2/\text{MoO}_3$	I^-/I_3^-	N719	12.95	0.754	62.7	6.12	—	—	266
Pt reference	I^-/I_3^-	N719	13.05	0.759	60.9	6.03	—	—	266
$\text{Co}_{0.85}\text{Se}$	I^-/I_3^-	N719	13.44	0.66	68	6.03	55.83	9.28	267
Pt reference	I^-/I_3^-	N719	14.37	0.67	67	6.45	30.64	13.89	267
$\text{Co}_{0.85}\text{Se}$ (front irradiation)	I^-/I_3^-	N719	16.74	0.742	66.8	8.30	—	2.84	268
$\text{Co}_{0.85}\text{Se}$ (rear irradiation)	I^-/I_3^-	N719	9.92	0.721	64.7	4.63	—	—	268
$\text{Ni}_{0.85}\text{Se}$ (front irradiation)	I^-/I_3^-	N719	16.67	0.740	63.6	7.85	—	2.96	268
$\text{Ni}_{0.85}\text{Se}$ (rear irradiation)	I^-/I_3^-	N719	9.26	0.731	64.6	4.37	—	—	268
$\text{Cu}_{0.50}\text{Se}$ (front irradiation)	I^-/I_3^-	N719	14.55	0.713	62.0	6.43	—	5.44	268
$\text{Cu}_{0.50}\text{Se}$ (rear irradiation)	I^-/I_3^-	N719	10.01	0.666	63.6	4.24	—	—	268
FeSe (front irradiation)	I^-/I_3^-	N719	17.10	0.733	61.0	7.64	—	4.90	268
FeSe (rear irradiation)	I^-/I_3^-	N719	10.49	0.732	65.8	5.05	—	—	268
$\text{Ru}_{0.33}\text{Se}$ (front irradiation)	I^-/I_3^-	N719	18.93	0.715	68.1	9.22	—	2.77	268
$\text{Ru}_{0.33}\text{Se}$ (rear irradiation)	I^-/I_3^-	N719	11.89	0.714	69.5	5.90	—	—	268
Pt (front irradiation)	I^-/I_3^-	N719	13.09	0.712	66.3	6.18	—	7.23	268
Pt (rear irradiation)	I^-/I_3^-	N719	9.48	0.652	57.6	3.56	—	—	268
NiCo_2S_4 (hydrothermal method)	I^-/I_3^-	N719	13.38	0.76	63.2	6.9	—	—	269
NiCo_2O_4 (hydrothermal method)	I^-/I_3^-	N719	8.2	0.67	26.7	1.5	—	—	269
Pt reference	I^-/I_3^-	N719	14.20	0.8	63.4	7.7	—	—	269
NbSe_2 (nanosheets)	I^-/I_3^-	N719	15.04	0.77	63	7.34	27.72	2.59	279
NbSe_2 (nanorods)	I^-/I_3^-	N719	13.94	0.76	64	6.78	19.38	6.21	279
NbSe_2/C	I^-/I_3^-	N719	15.58	0.77	65	7.80	24.07	3.52	279
Pt reference	I^-/I_3^-	N719	15.88	0.72	69	7.90	8.15	2.35	279
NbSe_2 (nanosheets)	I^-/I_3^-	N719	16.85	0.74	62	7.73	—	—	280
NbSe_2 (nanorods)	I^-/I_3^-	N719	14.85	0.74	46	5.05	—	—	280
NbSe_2 (microparticles)	I^-/I_3^-	N719	14.93	0.75	55	6.27	—	—	280
Pt reference	I^-/I_3^-	N719	15.59	0.72	62	7.01	—	—	280
MoSe_2 (solvothermal reaction)	I^-/I_3^-	N719	14.11	0.73	65	6.70	10.32	2.43	281
WSe_2 (solvothermal reaction)	I^-/I_3^-	N719	15.50	0.73	66	7.48	10.70	0.78	281
TaSe_2 (solvothermal reaction)	I^-/I_3^-	N719	15.81	0.73	64	7.32	10.00	1.89	281
Pt reference	I^-/I_3^-	N719	16.84	0.70	67	7.91	6.32	1.32	281
NiSe_2 (hydrothermal reaction)	I^-/I_3^-	N719	15.94	0.734	74.3	8.69	2.57	0.81	282
Pt reference	I^-/I_3^-	N719	15.26	0.731	72.1	8.04	2.50	0.97	282
$\text{NiCo}_2\text{S}_4/\text{NiS}$ (spin casting)	I^-/I_3^-	N719	17.7	0.744	67	8.8	—	—	286



Table 4 (Contd.)

Counter electrodes	Redox couple	Dye	J_{sc} (mA cm $^{-2}$)	V_{oc} (V)	FF (%)	PCE (η , %)	R_s (Ω cm 2)	R_{CT} (Ω cm 2)	Ref.
NiCo ₂ S ₄ (spin casting)	I $^-$ /I ₃ $^-$	N719	17.4	0.743	66	8.5	—	—	286
Co ₉ S ₈ (spin casting)	I $^-$ /I ₃ $^-$	N719	16.2	0.741	64	7.7	—	—	286
NiS (spin casting)	I $^-$ /I ₃ $^-$	N719	14.9	0.735	63	6.9	—	—	286
Pt reference	I $^-$ /I ₃ $^-$	N719	16.5	0.736	67	8.1	—	—	286
Ni _{0.33} Co _{0.67} Se	I $^-$ /I ₃ $^-$	N719	17.29	0.789	67	9.01	30.40	1.11	287
Ni _{0.5} Co _{0.5} Se	I $^-$ /I ₃ $^-$	N719	16.42	0.783	69	8.80	30.38	1.50	287
Ni _{0.67} Co _{0.33} Se	I $^-$ /I ₃ $^-$	N719	15.89	0.784	69	8.59	30.04	1.96	287
Co ₃ Se ₄	I $^-$ /I ₃ $^-$	N719	14.96	0.793	67	7.95	29.94	7.66	287
NiSe	I $^-$ /I ₃ $^-$	N719	14.54	0.783	64	7.23	29.87	13.88	287
Pt reference	I $^-$ /I ₃ $^-$	N719	15.33	0.791	69	8.30	30.30	2.88	287
FeSe ₂ (nanosheets, under N ₂)	I $^-$ /I ₃ $^-$	N719	17.49	0.718	60	7.53	8.07	0.53	302
FeSe ₂ (nanosheets, air exposed)	I $^-$ /I ₃ $^-$	N719	15.51	0.708	56	6.15	10.13	6.26	302
FeSe ₂ (microparticles)	I $^-$ /I ₃ $^-$	N719	16.32	0.715	59	6.88	8.51	4.10	302
Pt reference	I $^-$ /I ₃ $^-$	N719	17.77	0.725	58	7.47	7.94	1.68	302
FeSe ₂ microparticles (MPs)	I $^-$ /I ₃ $^-$	N719	15.63	0.745	66	7.68	9.03	2.32	303
FeSe ₂ nanosheets (NSs)	I $^-$ /I ₃ $^-$	N719	16.14	0.744	70	8.39	8.78	0.49	303
FeSe ₂ nanorods (NRs)	I $^-$ /I ₃ $^-$	N719	15.79	0.748	68	8.03	8.71	1.62	303
Pt reference	I $^-$ /I ₃ $^-$	N719	15.87	0.750	69	8.20	8.62	1.15	303
FeSe ₂ (3D flower-like)	I $^-$ /I ₃ $^-$	N719	14.93	0.744	72.1	8.00	16.82	0.53	304
FeSe ₂ (sphere-shaped)	I $^-$ /I ₃ $^-$	N719	14.60	0.724	69.8	7.38	27.05	0.96	304
Pt reference	I $^-$ /I ₃ $^-$	N719	15.13	0.741	70.2	7.87	17.01	0.78	304
CoSe ₂ (hydrothermal, 140 °C)	I $^-$ /I ₃ $^-$	N719	16.65	0.750	64.4	8.04	8.783	0.132	309
CoSe ₂ (hydrothermal, 160 °C)	I $^-$ /I ₃ $^-$	N719	17.04	0.743	66.2	8.38	8.034	0.097	309
CoSe ₂ (hydrothermal, 180 °C)	I $^-$ /I ₃ $^-$	N719	15.44	0.750	63.9	7.40	15.17	0.932	309
Pt reference	I $^-$ /I ₃ $^-$	N719	16.88	0.743	62.4	7.83	12.86	1.923	309
CoSe ₂ /C-NG	I $^-$ /I ₃ $^-$	N719	17.51	0.73	67	8.41	20.6	0.85	310
CoSe ₂ /C-NR	I $^-$ /I ₃ $^-$	N719	15.98	0.73	67	7.83	20.6	1.16	310
CoSe ₂ /C-NCW	I $^-$ /I ₃ $^-$	N719	18.03	0.73	67	8.92	20.6	0.52	310
CoSe ₂ /C-NCW on nickel foam	I $^-$ /I ₃ $^-$	N719	18.86	0.78	71	10.46	—	—	310
CoSe ₂ /C-NCW on carbon cloth	I $^-$ /I ₃ $^-$	N719	18.16	0.76	71	9.87	—	—	310
Pt reference	I $^-$ /I ₃ $^-$	N719	16.43	0.74	67	8.25	20.6	1.04	310
CoSe ₂	I $^-$ /I ₃ $^-$	N719	12.95	0.773	65	6.47	—	0.50	311
CoSe ₂ @RGO	I $^-$ /I ₃ $^-$	N719	12.24	0.792	72	7.01	—	0.20	311
Reduced graphene oxide (RGO)	I $^-$ /I ₃ $^-$	N719	12.11	0.761	40	3.66	—	64.75	311
Pt reference	I $^-$ /I ₃ $^-$	N719	13.12	0.765	67	6.77	—	0.61	311
Ni _{0.85} Se	I $^-$ /I ₃ $^-$	N719	15.63	0.739	72	8.32	1.8	1.8	312
Co _{0.85} Se	I $^-$ /I ₃ $^-$	N719	16.98	0.738	75	9.40	2.1	0.6	312
Pt reference	I $^-$ /I ₃ $^-$	N719	16.03	0.738	73	8.64	2.6	1.1	312
Bi ₂ Se ₃ nanoparticles	I $^-$ /I ₃ $^-$	N719	7.02	0.55	46	1.86	—	—	325
Bi ₂ Se ₃ /graphene (40 mg)	I $^-$ /I ₃ $^-$	N719	15.42	0.78	50	6.35	—	—	325
Bi ₂ Se ₃ /graphene (60 mg)	I $^-$ /I ₃ $^-$	N719	16.36	0.75	57	7.09	—	—	325
Bi ₂ Se ₃ /graphene (80 mg)	I $^-$ /I ₃ $^-$	N719	16.01	0.76	53	6.66	—	—	325
Pt reference	I $^-$ /I ₃ $^-$	N719	15.65	0.68	59	6.47	—	—	325
ZnO (photoanode)	I $^-$ /I ₃ $^-$	N719	8.189	0.656	55.2	2.96	16.6	7.23	335
Bi ₂ Te ₃ /ZnO (photoanode)	I $^-$ /I ₃ $^-$	N719	11.767	0.637	57.0	4.27	15.8	3.75	335

^a Nanograin (NG), nanorock (NR), nanoclimbing-wall (NCW), nickel foam (NF), carbon cloth (CC), rGO = reduced graphene oxide. In the case of R_s and R_{CT} : some of the authors used Ω instead of Ω cm 2 for the resistances without mentioning the size of the electrode.

replace expensive Pt CEs for DSSCs for indoor, outdoor or wearable applications.

CoSe₂ and RGO composites were also explored as CEs in DSSCs, which showed a PCE of 7.01% *versus* a Pt CE ($\eta = 6.77\%$).³¹¹ Co_{0.85}Se and Ni_{0.85}Se was deposited on FTO glass substrate by a low-temperature hydrothermal process and were used as CEs for DSSCs by Gong *et al.*³¹² Co_{0.85}Se has a graphene-like nanostructure and possesses a large surface area, while Ni_{0.85}Se is composed of aggregated particles. The graphene-like Co_{0.85}Se CE showed higher electrocatalytic activity than that of

the Pt CE for the reduction of triiodide (I₃ $^-$). DSSCs with Co_{0.85}Se CEs showed a PCE of 9.40%, significantly higher than that of a Pt CE (8.64%), under simulated solar light of 100 mW cm $^{-2}$ (AM 1.5G). In the case of the Ni_{0.85}Se CE, the PCE of 8.32% was slightly lower than a Pt CE. Both J_{sc} and PCE values showed a relative order of Ni_{0.85}Se < Pt < Co_{0.85}Se. The R_{CT} value was found to increase in the relative order Co_{0.85}Se (0.6 Ω cm 2) < Pt (1.1 Ω cm 2) < Ni_{0.85}Se (1.8 Ω cm 2), suggesting an inverse order of electrocatalytic activity of these CEs in the DSSCs. Table 4 summarizes the photovoltaic parameters of MoSe₂, WSe₂,



TaSe₂, NbSe₂, FeSe₂, CoSe₂ and Bi₂Se₃ based CEs for DSSCs, and their comparison with a standard Pt CE.

4.7 Bi₂Se₃ counter electrodes

Bismuth selenide (Bi₂Se₃) and bismuth telluride (Bi₂Te₃) have been previously studied as topological insulators.^{313,314} Bi₂Se₃, a semiconducting and thermoelectric material, can be processed into single layers, nanosheets, nanotubes, nanoribbons, and nanowires³¹⁵⁻³¹⁸ and has applications in field-effect transistors,³¹⁹ sensors,³²⁰ non-volatile memory devices,³²¹ photovoltaic devices,³²² and drug delivery and anti-cancer therapy.^{323,324} Bi₂Se₃/RGO nanocomposites were prepared by a microwave-assisted hydrothermal method as a CE for a DSSC by Zhu *et al.*³²⁵ Fig. 27 shows the TEM images of the graphene nanosheets, Bi₂Se₃ nanospheres and Bi₂Se₃/graphene nanocomposites containing 60 mg graphene contents. The TEM images showed that 10–15 nm Bi₂Se₃ nanoparticles were attached onto graphene nanosheets. SEM images showed that the graphene had a flake-like structure while the Bi₂Se₃ nanoparticles were large size spheres. Furthermore, the surface of the graphene oxide was found to be very smooth in comparison with graphene nanosheets doped with Bi₂Se₃ nanoparticles. The inclusion of Bi₂Se₃ nanoparticles onto graphene nanosheets was controlled to achieve high electrocatalytic activity of the CE for the reduction of triiodide (I₃[−]). The DSSC with a Bi₂Se₃/graphene (60 mg) CE yielded a high PCE of 7.09%,

which is comparable to a Pt CE ($\eta = 6.23\%$). The Bi₂Se₃/graphene nanocomposite CEs with 40 mg and 80 mg graphene content showed PCE values of 6.35% and 6.66% for the DSSCs, respectively, which was much higher than that of pure Bi₂Se₃ CE ($\eta = 1.86\%$), but still comparable to a Pt CE.

5. Bi₂Te₃ based photoanodes

Bismuth telluride (Bi₂Te₃) has been studied for thermoelectric applications and can be processed into nanowires arrays,³²⁶⁻³²⁹ nanotubes,³³⁰ nanoplates,³³¹ nanosheets,^{332,333} and thin films.³³⁴ Dou *et al.*³³⁵ developed hybrid photoanodes by dispersing Bi₂Te₃ nanotubes into ZnO nanoparticles. The 0.5, 1.0, 1.5, 2.0, and 2.5 wt% of highly crystalline Bi₂Te₃ nanotubes were mixed with ZnO nanoparticles to fabricate photoanodes for DSSCs. Pt films deposited on FTO glass was used as a CE. The electrolyte consisted of 0.05 M I₂, 0.5 M LiI, and 0.1 M 4-*tert*-butylpyridine in acetonitrile-propylene carbonate (1 : 1) solution. In the Bi₂Te₃/ZnO hybrid, Bi₂Te₃ nanotubes provided a conduction pathway which facilitated electron transfer. The J_{sc} value increased gradually with increasing Bi₂Te₃ nanotubes content up to 1.5 wt% (11.767 mA cm^{−2}) and then started decreasing as the Bi₂Te₃ nanotubes content exceeded 2.0 wt% (9.957 mA cm^{−2}), due to the low dye loading on the surface of ZnO nanoparticles. A similar trend was observed for the PCE values. The DSSCs with

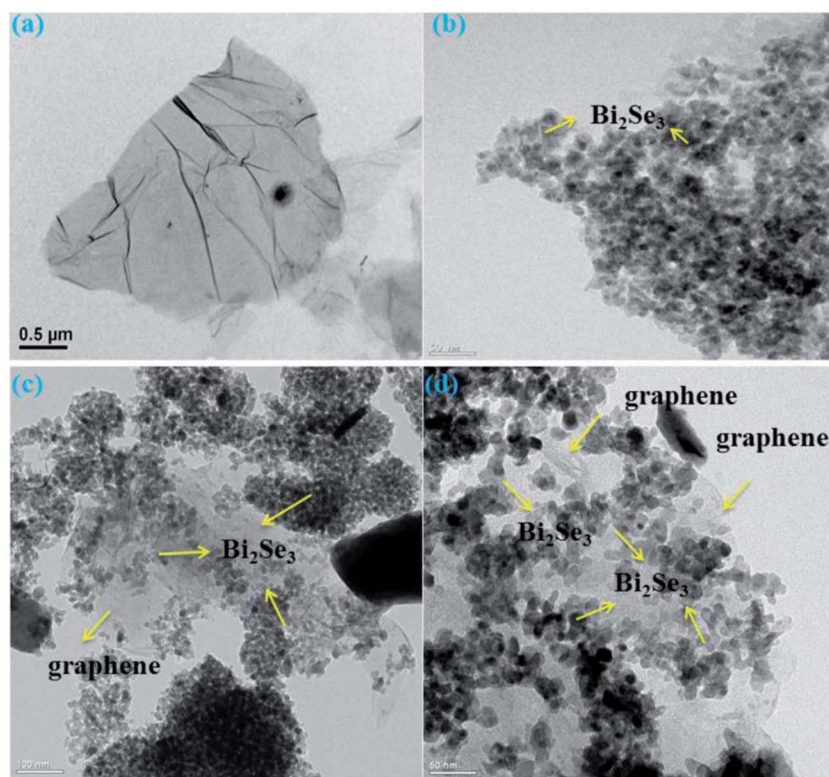


Fig. 27 TEM images of (a) graphene nanosheet, (b) Bi₂Se₃ nanospheres (c) and (d) Bi₂Se₃/graphene nanocomposite (60 mg graphene). Reprinted with permission from ref. 325, L. Zhu, K. Y. Cho and W. C. Oh, microwave-assisted synthesis of Bi₂Se₃/reduced graphene oxide nanocomposite as efficient catalytic counter electrode for dye-sensitized solar cell, *Fullerenes, Nanotubes, Carbon Nanostruct.*, 2016, **24**, 622–629. Copyright © Taylor & Francis Group.



a $\text{Bi}_2\text{Te}_3/\text{ZnO}$ composite photoanode containing 1.5 wt% Bi_2Te_3 nanotubes in the ZnO photoanode showed a PCE of 4.27%, which is 44.3% higher compared with a pure ZnO photoanode. The PCE values were 2.96% for the bare ZnO photoanode, and 3.74, 3.96, 4.27, 3.41 and 3.01% for the 0.5, 1.0, 1.5, 2.0 and 2.5 wt% Bi_2Te_3 nanotubes content photoanodes, respectively. This study indicated that loading of thermoelectric Bi_2Te_3 in a ZnO photoanode improves the photovoltaic performance of DSSCs. Wan *et al.*³³⁶ prepared hexagonal Bi_2Te_3 nanosheets of 300–400 nm length by a hydrothermal method. The nanocomposites of the Bi_2Te_3 nanosheets and ZnO nanoparticles were used as photoanodes for DSSCs, where the Bi_2Te_3 nanosheet concentration was varied from 0 to 0.25 wt%. The DSSCs with 0.15 wt% of Bi_2Te_3 nanosheets in the Bi_2Te_3 nanosheet/ ZnO nanoparticle composite photoanode showed a PCE of 4.10%, which was improved by 46.95% compared with the bare ZnO photoanode. The thermoelectric Bi_2Te_3 nanosheets in the composite photoanode helped in enhancing the electron density and reducing the temperature of the DSSCs. The Bi_2Te_3 nanosheet/ ZnO nanoparticles composite photoanode significantly improved the DSSC performance. A thermoelectric $\text{Bi}_2\text{Te}_3/\text{TiO}_2$ composite based photoanode was also used for DSSCs, where Bi_2Te_3 nanoplates help in converting heat into electricity and enhanced the rate of charge transfer.³³⁷ This resulted in a 28% increase of the PCE of the DSSC. The Bi_2Te_3 nanoplates have also been used for doping TiO_2 photoanodes.³³⁸ The effect of Bi_2Te_3 nanoplates size was evaluated for DSSCs, where a decrease in the size of the Bi_2Te_3 nanoplates led to a higher PCE. The performance of DSSCs with a $\text{Bi}_2\text{Te}_3/\text{TiO}_2$ photoanode increased by 15.3% compared to the undoped TiO_2 photoanode.

6. Long-term stability of TMDs based DSSCs

The long-term stability of DSSCs is one of the most important parameters for commercial applications. The stability of DSSC devices depends upon a number of factors and the components used in their fabrication. The decrease in power conversion

efficiency of a DSSC can be associated with the stability of different electrolyte components, photosensitizing dyes, aging of the TiO_2 photoanode, degradation of the CE (cathode), corrosion of components by electrolytes, sealant, leakage, exposure to solar irradiation, high humidity, and elevated temperature.^{339–349}

A few research reports have been published on the long-term stability of TMDs based DSSCs which are briefly discussed here. Infant *et al.*¹³¹ studied the stability of CVD-deposited vertically oriented MoS_2 thin films on an FTO surface used as a CE in a DSSC. The electrochemical stability of a MoS_2 CE based DSSC was analyzed by CV measurements, where electrodes were repeatedly subjected to 20 cycles at a 10 mV s^{−1} scan rate for the I^-/I_3^- redox couple in the electrolyte. The MoS_2 based CE showed no significant change up to 20th consecutive cycle, whereas the Pt CE exhibited some changes between the cycles (Fig. 28). This confirms that CVD deposited MoS_2 strongly adhered onto the surface of the FTO substrate. The stability of MoS_2 CEs was measured under ambient conditions by storing them for 15 days, where the PCE remained at 94% of its initial efficiency value, which was much higher than that of the Pt CE.

For preparing Pt-free dye-sensitized solar cells, Liu *et al.*³⁵⁰ fabricated DSSCs using MoS_2 and RGO composite as a CE for the reduction of triiodide (I_3^-) to iodide (I^-). AFM, XPS, and XRD confirmed the deposition of MoS_2 nanoparticles onto the RGO surface. The CV measurement showed a higher current density for the MoS_2/RGO nanocomposite based CE compared to RGO, MoS_2 , and Pt-sputtered CEs due to an increased surface area. The MoS_2/RGO CE also exhibited a low R_{CT} of 0.57 Ω cm² for the reduction of triiodide (I_3^-) to iodide (I^-). The MoS_2/RGO nanocomposite CE based DSSC showed a PCE of 6.04%, comparable to a PCE of 6.38% for the conventional Pt CE. MoS_2/RGO nanocomposites based CEs also have better electrochemical stability, as no degradation in current densities was observed up to 100 repeated CV tests. The stability test conducted on a DSSC having MoS_2/RGO nanocomposites as CEs showed over 10% degradation in PCE over a period of 20 days, as depicted in (Fig. 29a). Therefore, MoS_2/RGO nanocomposites based CEs were found to be stable both for environmental and consecutive electrochemical tests. Li *et al.*²⁰⁰ prepared a composite film of $\text{TiS}_2/\text{PEDOT:PSS}$ on an ITO substrate as a CE

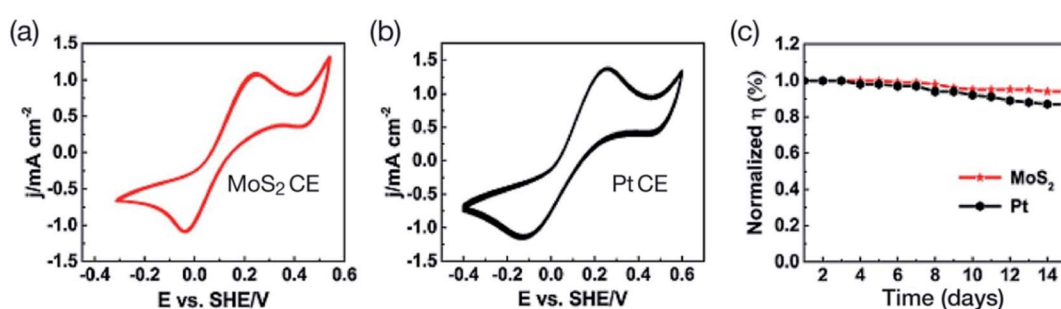


Fig. 28 Electrochemical properties of thin films of MoS_2 prepared at 600 °C for 15 minutes. 20 consecutive cyclic voltammogram (CV) curve of MoS_2 (a) and Pt (b) counter electrodes recorded at the scan rate of 10 mV s^{−1} and (c) PCE of MoS_2 and Pt CEs based DSSCs measured for 15 days under ambient conditions. Reprinted with permission from ref. 131, R. S. Infant, X. Xu, W. Yang, F. Yang, L. Hou and Y. Li, highly active and reflective MoS_2 counter electrode for enhancement of photovoltaic efficiency of dye sensitized solar cells. *Electrochim. Acta*, 2016, **212**, 614–620. Copyright © Elsevier.



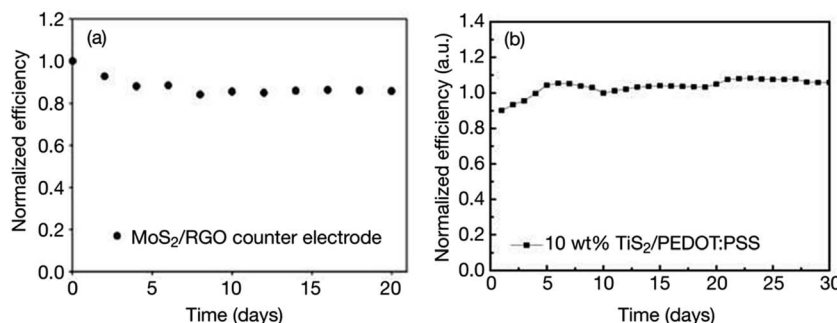


Fig. 29 (a) Stability of a DSSC with MoS₂/RGO based counter electrode recorded for 20 days. Reprinted with permission from ref. 350, C. J. Liu, S. Y. Tai, S. W. Chou, Y. C. Yu, K. D. Chang, S. Wang, F. S. S. Chien, J. Y. Lin and T. W. Lin, facile synthesis of MoS₂/graphene nanocomposite with high catalytic activity toward triiodide reduction in dye-sensitized solar cells. *J. Mater. Chem.*, 2015, **22**, 21057–21064. Copyright© Royal Society of Chemistry. (b) The long-term stability of the DSSCs with 10 wt% TiS₂/PEDOT:PSS composite CE. Reprinted with permission from ref. 200, C. T. Li, C. P. Lee, Y. Y. Li, M. H. Yeh and K. C. Ho, a composite film of TiS₂/PEDOT:PSS as the electrocatalyst for the counter electrode in dye-sensitized solar cells. *J. Mater. Chem. A*, 2013, **1**, 14888–14896. Copyright© Royal Society of Chemistry.

of DSSCs for the I[−]/I₃[−] redox system, which exhibited a PCE as high as 7.04% and is comparable to a Pt CE. Fig. 29b shows dark current density–voltage curves of DSSCs with Pt, bare TiS₂, bare PEDOT:PSS, and 10 wt% TiS₂/PEDOT:PSS composite CEs, and also the long-term stability of a 10 wt% TiS₂/PEDOT:PSS composite CE based DSSC. This another example of long-term stability of DSSCs based on TiS₂/PEDOT:PSS CEs.

The stability of DSSCs with a TiS₂/graphene hybrid CE was studied by Meng *et al.*¹⁹⁹ (Fig. 30). The TiS₂–graphene hybrid CE maintained 96% of its initial PCE value after 500 hours in air, also exhibiting higher electrochemical stability. The R_s and Z_N values for the TiS₂–graphene hybrid CE based DSSC did not change after 10 cyclic measurements. The R_{CT} value of a DSSC with Pt CE significantly increased with increasing cycling number, while there was no change in the R_{CT} value of the TiS₂–graphene hybrid after 10 cycles. This indicates better electrochemical stability of the TiS₂–graphene hybrid CE than the Pt CE. The stability of photovoltaic parameters of DSSCs having

mesoporous CoS₂ nanotube arrays as CEs was recorded for 10 days by Tsai *et al.*²³³ a slight drop in the V_{oc} and FF values were observed, which resulted in a 2.2% decrease in the PCE of the CoS₂ nanotube array CEs. The photovoltaic parameters of the DSSC were quite stable up to 10 days, indicating good stability of DSSCs with mesoporous CoS₂ nanotube array CEs (Fig. 31).

The electrochemical stability of DSSCs with FeSe₂ nanosheets and Pt CEs in an iodine-based electrolyte was studied by Huang *et al.*³⁰² Both CEs were subjected to consecutively CV scanning. The FeSe₂ nanosheets-based CE showed no change in the current densities and E_{pp} values up to 1000 cycles, whereas the E_{pp} value for the Pt-based CE was observed to increase after 1000 consecutive cycles (Fig. 32). This study confirmed a better corrosion resistance of FeSe₂ nanosheets CE to the iodine-based electrolyte than a Pt CE. Both CEs were also subjected to sequential EIS scanning, where negligible changes in R_{CT} were noticed after 10 cycles, again indicating an excellent electrochemical stability of both CEs. Furthermore, R_s and Z_N values also showed no change upon repeated scanning cycles.

The stability of a FeS₂ nanorod based CE was also measured in an iodide (I[−]) electrolyte up to 10 days, and CV plots showed slight change at different times of aging.²²² The hydrothermally synthesized CoSe₂ nanorods were used as an electrocatalyst for a DSSC for the reduction of I₃[−] using N719 dye by Sun *et al.*³⁵¹ The single crystalline CoSe₂ nanorods based CE showed a PCE of 10.20%, compared with a PCE of 8.17% for a Pt CE, under 1 Sun illumination. The DSSCs having CoSe₂ CEs were stored in daylight and their photovoltaic properties were measured every day, and showed long-term stability. These studies show an excellent electrochemical stability of TMDs-based CEs for DSSCs in iodine-based electrolyte, with no corrosion. The TMDs CEs are also quite stable when stored under ambient conditions of up to 2–3 weeks, as no significant changes were observed in the PCEs of the DSSC devices. Furthermore, TMDs based CEs should be further investigated to exhibit better electrochemical stability and environmental stability than that of standard Pt CEs, and endurance tests should be carried out to study the their stability. The DSSC devices should have a service life of at least 20 years under ambient conditions as pointed out by

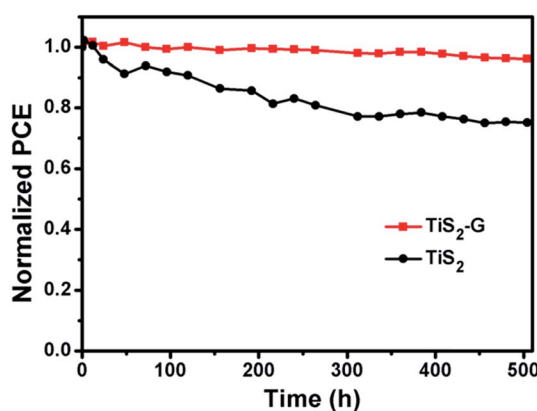


Fig. 30 Stability of DSSCs with TiS₂–graphene hybrid and Pt CEs. Reprinted with permission from ref. 199, X. Meng, C. Yu, B. Lu, J. Yang and J. Qiu, dual integration system endowing two-dimensional titanium disulfide with enhanced triiodide reduction performance in dye-sensitized solar cells. *Nano Energy*, 2016, **22**, 59–69. Copyright© Elsevier.

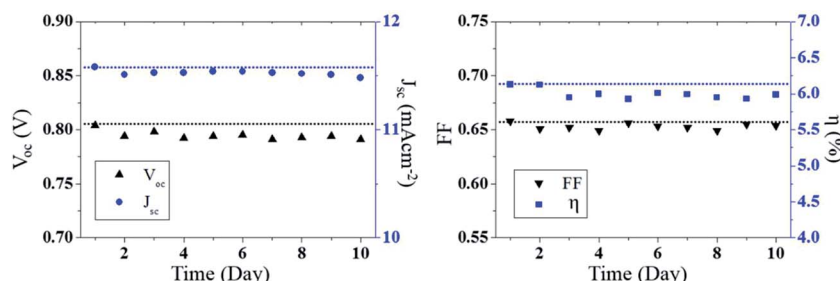


Fig. 31 Stability of photovoltaic parameters; open-circuit voltage (V_{oc}), short-circuit photocurrent density (J_{sc}), fill factor (FF), and power conversion efficiency (η) of DSSCs with mesoporous CoS_2 nanotube array CE as a function of time. Reprinted with permission from ref. 233, J. C. Tsai, M. H. Hon and I. C. Leu, fabrication of mesoporous CoS_2 nanotube arrays as the counter electrodes of dye-sensitized solar cells. *Chem.–Asian J.*, 2015, **10**, 1932–1939. Copyright © Wiley–VCH.

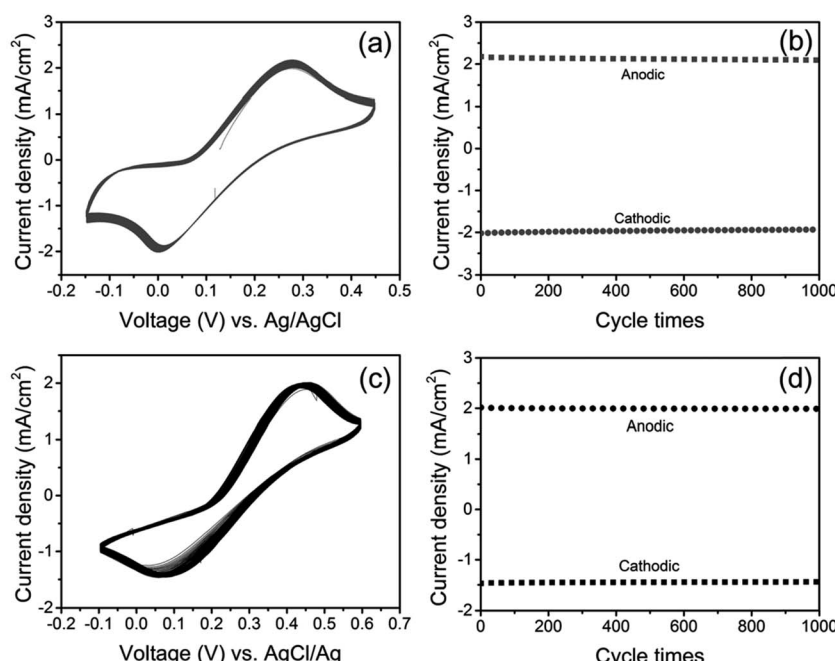


Fig. 32 1000 consecutive cycles of CVs of FeSe_2 nanosheets-based CE (a) and Pt-based CE (c) at a scan rate of 50 mV s^{-1} and the anodic as well as cathodic peak current densities up to 1000 cycles for FeSe_2 - (b) and Pt-based CEs (d), respectively. Reprinted with permission from ref. 302, S. Huang, Q. He, W. Chen, Q. Qiao, J. Zai and X. Qian, ultrathin FeSe_2 nanosheets: controlled synthesis and application as a heterogeneous catalyst in dye-sensitized solar cells. *Chem.–Eur. J.*, 2015, **21**, 4085–4091. Copyright © Wiley–VCH.

Grätzel.³⁴² The long-term stability of DSSCs is feasible by carefully selecting components and solar cell structure. The TMDs based CEs may overcome the concerns associated with scarcity, high production cost, and corrosion of Pt CEs in electrolyte solutions. Researchers in this field should address the stability for of TMDs based CEs to evaluate the performance of Pt-free DSSCs.

Some achievements and strategies to overcome the long-term stability of Pt-free DSSCs are summarized in the following section. Kato *et al.*³⁵² used Raman spectroscopy and EIS to evaluate the durability of DSSCs for 2.5 years in outdoor conditions. Both N719 dye-adsorbed TiO_2 CEs and carbon CEs were found to be stable. The V_{oc} and FF values were slightly decreased because of increased Z_N of triiodide (I_3^-), arising

from the change in electrolyte components. Matsui *et al.*³⁵³ achieved stability over 1000 hours for DSSCs at 85°C and under 85% relative humidity, and recorded no degradation of the photovoltaic performance between -40 and 90°C for 200 cycles. Xue *et al.*³⁵⁴ measured thermal stability of DSSCs between -20 to 25°C temperature range for 1080 hours. DSSCs with N719 dye absorbed on the TiO_2 photoanode retained 80% of their initial PCE values after aging for 1080 hours. The deterioration of the N719 dye was found to be the main cause for a decrease the PCE and degradation of DSSC devices. Harikisun and Desilvestro³⁵⁵ evaluated photovoltaic performance of Z907-based DSSCs after continuous light-soaking at 55 – 60°C for 25 600 hours, where a slight degradation was observed. The accelerated aging tests predicted a life time of 40 years for Middle European conditions



while 25 years for Southern European conditions. The 10% and 20% decrease of photovoltaic performance was measured for ionic liquid and solvent based electrolytes over 1000 hours at 180 °C, respectively.

Strategies to improve the long-term stability of DSSCs include developing new photosensitizing dyes, new non-volatile electrolytes, encapsulation, and of course new photoanodes and CEs. Like the heterojunction solar cells,²⁷ several strategies for improving electrochemical and thermal stability of DSSC devices have been proposed. The role of photosensitizing dyes containing π -conjugated organic systems have been studied for the stability of DSSCs. Wu *et al.*³⁵⁶ suggested a novel concept of molecular engineering of donor-acceptor- π -acceptor (D-A- π -A) based photosensitizers, not only to improve the stability of DSSCs but also to enhance the photovoltaic performance. Katoh *et al.*³⁵⁷ compared the stability of five sensitizing dyes in DSSCs with and without π -conjugated oligothiophene moiety, which indicated that dyes with π -conjugated oligothiophene exhibit higher stability than those of without oligothiophene moiety. Joly *et al.*³⁵⁸ fabricated DSSCs with a new organic sensitizer (RK1) which showed a J_{sc} of 18.26 mA cm⁻², V_{oc} of 0.76 V, and FF of 0.74, resulting in a PCE value of 10.2% under 1 Sun illumination for the triiodide/iodide (I_3^-/I^-) redox couple. A similar PCE of 10.19% was achieved for the ruthenium N719 dye. When RK1 dye was used with a viscous ionic liquid electrolyte, the DSSC yielded a J_{sc} of 15.40 mA cm⁻², V_{oc} of 0.665 V, FF of 0.69, and a PCE of 7.36%, with outstanding stability. The DSSC exhibited no degradation of photovoltaic performance after visible-light soaking at 65 °C for 2200 hours, but, thereafter, DSSC started degrading and retained 75% of its initial PCE at 65 °C after 5000 hours.

A new coumarin dye, namely 2-cyano-3-[5'-(1-cyano-2-(1,1,6,6-tetramethyl-10-oxo-2,3,5,6-tetrahydro-1H,4H,10H-11-oxa-3a-aza-benzo[*d*]anthracen-9-yl)-vinyl]-[2,2']bithiophenyl-5-yl)-acrylic acid (NKX-2883) was developed by Wang *et al.*³⁵⁹ to examine the stability of DSSCs in a nonvolatile electrolyte made of 0.1 M I_2 , 0.6 M 1,2-dimethyl-3-*n*-propylimidazolium iodide (DMPImI), and 0.1 M *N*-methylbenzimidazole (NMBI) in 3-methoxypropionitrile. The NKX-2883 dye-based DSSC showed a J_{sc} value of 18.8 mA cm⁻² and a PCE of 6.5% with 6 micron thick TiO_2 film. The DSSCs maintained a PCE of 6% under continuous light soaking of 100 mW cm⁻² (1 Sun illumination) at 50–55 °C for 1000 hours. Organic photosensitizing dyes having long alkyl chains were also proposed to improve long-term stability for both liquid and quasi-solid-state DSSCs.³⁶⁰ In another study, quinoxaline based metal-free organic sensitizing dyes were utilized to introduce long-term stability in DSSCs.³⁶¹ The length of the alkyl chains on the donor unit was found to affect the performance of DSSC devices. The quasi-solid-state DSSCs with a quinoxaline-based organic dye showed a PCE of 7.14%, and maintained 100% of its initial PCE value after continuous sunlight irradiation for 1000 hours, indicating that molecular engineering of dye molecules can lead to both high PCE and long-term stability of DSSC devices.

The electrochemical stability of CEs in corrosive triiodide/iodide (I_3^-/I^-) electrolyte is of significant concern because it restricts commercial applications of DSSCs. To overcome this

disadvantage of the I^-/I_3^- redox couple, research activities have been focused on finding alternative iodine-free non-corrosive redox electrolytes.^{19,362–366} Cell-sealing conditions are also important when using liquid electrolytes. The DSSCs can be made suitable for outdoor applications by using encapsulation. The role of electrolytes has been studied in the stability of DSSCs by Sauvage *et al.*³⁶⁷ suggesting a new electrolyte based on butyronitrile solvent with low volatility, along with thiophene-based sensitizer Na-Ru(4,4'-bis(5-(hexylthio)thiophen-2-yl)-2,2'-bipyridine)(4-carboxylic acid-4'-carboxylate-2,2'-bipyridine)(thiocyanate)2, coded C106, for DSSCs which showed >95% retention of PCE value after 1000 hours at 60 °C for an exposure to 100 mW cm⁻² light illumination. Yoon *et al.*³⁶⁸ fabricated DSSCs with 1-propyl-3-methyl imidazolium iodide (PMII) ion-gel electrolyte with a poly(styrene-block-ethyleneoxide-block-styrene) (SEOS) triblock copolymer. The DSSC with ion-gel electrolyte retained 92% of its initial PCE up to 1440 hours, compared to 78% for the ionic liquid electrolyte. Lee *et al.*³⁶⁹ reported long-term stability of DSSCs with organic tetrabutylammonium iodide (TBAI) or 1-methyl 3-propyl imidazolium iodide (PMII) in methoxypropionitrile-based electrolytes. The DSSCs having TBAI retained 96.9% of their initial efficiency after being stored for 1000 hours under 1 Sun light irradiation at 60 °C. Yang *et al.*³⁷⁰ proposed the use of poly(ethylene oxide)-poly(vinylidene fluoride) (PEO-PVDF) polymer-blend electrolytes with water and ethanol for improving stability of DSSCs. The electrical conductivity was found to increase after adding water and ethanol to the PEO-PVDF polymer-blend electrolytes. The cross-linking capability of hydroxyl-rich additives for modified electrolytes was found to have a positive impact. Chen *et al.*³⁷¹ demonstrated the long-time durability of DSSCs by using a succinonitrile, silica nanoparticles and 1-butyl-3-methylimidazolium tetrafluoroborate (BMI·BF₄) gel system which maintained 93% of its initial PCE after aging at 60 °C for 1000 hours. Dembele *et al.*³⁷² also demonstrated that adding 1.0 wt% concentration of MWCNTs to TiO_2 photoanodes can improve both PCE and stability of a DSSC, where the PCE value increased to 4.1% compared with 3.7% for pure TiO_2 photoanodes. The performance of the DSSC devices was measured for 10 consecutive days under ambient light exposure. The PCE decreased about 10% for the MWCNTs/ TiO_2 photoanodes, compared to 35% decrease in pure TiO_2 photoanodes.

The long-term stability of Pt-free DSSCs is of significant importance for both indoor and outdoor applications and different approaches can be examined to improve environmental stability.^{356–361,367–377} These studies show that long-term stability may be introduced in TMDs based DSSCs by similar strategies of using long alkyl chain organic dyes, ion-gel and polymer-based electrolytes, silica nanoparticles, or modifying TiO_2 photoanodes. Similar electrochemical and thermal stability studies should be conducted for TMD CEs for DSSC devices.

7. Conclusion and perspective

The electrochemical and photovoltaic properties of DSSC devices employing CEs (CEs) of 2D layered transition metal



dichalcogenides (MoS_2 , MoSe_2 , WS_2 , TiS_2 , NbSe_2 , TaSe_2 , NiSe_2 , FeSe_2 , CoSe_2 , SnS_2 , Bi_2Se_3 and their based composites) have been summarized and discussed. This data indicates that the PCEs of TMDs-based CEs surpasses conventional Pt CEs in dye-sensitized solar cell (DSSC) devices. The composites of TMDs with graphene, CNTs, carbon, carbon nanofibers (CNFs), and PEDOT:PSS also show a great potential as CEs for DSSCs. The DSSCs having CEs made of chemical vapor deposition (CVD)-grown vertically inclined MoS_2 films,¹³¹ hydrothermally prepared MoS_2 films,^{135,141} MoS_2 and MoSe_2 thin films deposited on Mo foil,^{260,261} MoS_2 /graphene, MoS_2 /CNTs,¹⁶⁴ MoS_2 /carbon,¹⁷¹ and MoSe_2 /PEDOT:PSS composites exhibit higher PCE values than that of Pt CEs for the reduction of triiodide (I_3^-) to iodide (I^-). Furthermore, the CEs of TiS_2 /graphene hybrids,¹⁹⁹ NiS_2 /reduced graphene oxide (RGO) composites,²¹⁰ FeS_2 ,²²¹ NbSe_2 ,²⁸⁰ and FeSe_2 nanosheets³⁰² also show a better photovoltaic performance than that of Pt CEs in DSSCs. The low cost and flexible CoSe_2 /carbon-nanoclimbing-wall CE deposited on nickel foam shows the highest PCE of 10.46% *versus* a Pt CE ($\eta = 8.25\%$) at 1 Sun illumination (100 mW cm⁻² (AM 1.5G)).³¹⁰ It has been observed that the morphology of CEs also plays an important role in determining the electrocatalytic activity of DSSC devices, where CEs with large surface area nanostructures tend to show larger PCE values and a higher electrocatalytic activity of the DSSCs.²⁸² The DSSCs with TiS_2 /graphene hybrids¹⁹⁹ and TiS_2 /PEDOT:PSS composites²⁰⁰ based CEs showed environmental stability of up to 20 and 30 days, respectively, with no degradation in the photovoltaic performance. Interestingly, thermoelectric Bi_2Te_3 nanosheet/ZnO nanoparticles composite based photoanodes³³⁵ exhibited a 46.95% increase in PCE value compared with a bare ZnO photoanode based DSSC. Also, the DSSC with the $\text{Bi}_2\text{Te}_3/\text{TiO}_2$ composite based photoanode³³⁶ showed a 28% increase in PCE than that of pure TiO_2 photoanode.

Transition metal dichalcogenides (TMDs) based materials which are analogues of 2D graphene are emerging as a great alternative to fabricating low-cost Pt-free DSSC devices. TMDs-based CEs have demonstrated better electrochemical stability than that of standard Pt CEs in iodine-based electrolyte and also under ambient conditions. In addition to long-term stability, TMDs may also cause cytotoxicity to humans, as has been observed for other nanostructured materials,^{378–383} therefore, aspects of toxicity should be investigated in studies with DSSC devices.

2D TMDs based CEs are a cheap alternative to Pt CEs for DSSCs. In this review, we have summarized recent developments of TMDs used as CE materials for DSSCs which are still in their infancy. The low-cost 2D TMDs are abundantly available in nature, and can easily be processed into thin films and hybridized with other inorganic and organic materials for fabricating DSSC devices. The vast majority of 2D TMDs have yet to be studied, even as 2D graphene-based materials, but at this early stage they offer a low-cost alternative and outperform their Pt counterparts. Tremendous possibilities exist for developing new TMDs based CEs for I_3^-/I^- , $\text{Co}^{2+}/\text{Co}^{3+}$ and T_2/T^- redox couples. The important requirements for commercial applications are ease of processing, low-cost manufacturing, high PCE

value, and long-term electrochemical stability. Like graphene-based materials, more edge active sites can be created in TMDs-based CEs to facilitate more dye adsorption. Research on the use of TMDs CEs are in very early stage of developing Pt-free DSSCs. TMDs based CEs offer increased charge transfer capability and fast reaction kinetics for the reduction of triiodide (I_3^-) to iodide (I^-) in electrolyte for DSSCs and their potential can be realized in parallel to graphene. The large family of TMDs, such as MoS_2 , MoSe_2 , MoTe_2 , WS_2 , WSe_2 , WTe_2 , FeSe_2 , TaS_2 , NbSe_2 , *etc.*, should also be explored with other inorganic and organic materials, as the family of 2D materials is enormously large and are expected to play an important role in developing low-cost highly efficient DSSCs for commercial applications.

Disclaimer

The authors cannot accept liability for any kind of scientific data contained in this review article whatsoever for the accuracy of contents or any omissions or any errors or a claim of completeness.

Acknowledgements

Eric Singh is thankful to Prof. Dr G. Y. Yeom for offering him a summer research internship in his group at the School of Advanced Materials Science and Engineering, Sungkyunkwan University (SKKU), South Korea. This work was supported by the Nano Material Technology Development Program through the National Research Foundation of Korea (NRF), funded by the Ministry of Education, Science and Technology (2016M3A7B4910429).

References

- 1 B. O'Regan and M. Grätzel, A low-cost, high-efficiency solar cell based on dye-sensitized, *Nature*, 1991, **353**, 737–740.
- 2 M. K. Nazeeruddin, A. Kay, I. Rodicio, R. Humphry-Baker, E. Müller, P. Liska, N. Vlachopoulos and M. Grätzel, Conversion of light to electricity by *cis*- X_2 bis(2,2'-bipyridyl-4,4'-dicarboxylate) ruthenium(II) charge-transfer sensitizers ($\text{X} = \text{Cl}^-$, Br^- , I^- , CN^- , and SCN^-) on nanocrystalline titanium dioxide electrodes, *J. Am. Chem. Soc.*, 1993, **115**, 6382–6390.
- 3 M. K. Nazeeruddin, P. Pechy and M. Grätzel, Efficient panchromatic sensitization of nanocrystalline TiO_2 films by a black dye based on a trithiocyanato-ruthenium complex, *Chem. Commun.*, 1997, 1705–1706.
- 4 S. Mathew, A. Yella, P. Gao, R. Humphry-Baker, B. F. Curchod, N. Ashari-Astani, I. Tavernelli, U. Rothlisberger, M. K. Nazeeruddin and M. Grätzel, Dye-sensitized solar cells with 13% efficiency achieved through the molecular engineering of porphyrin sensitizers, *Nat. Chem.*, 2014, **6**, 242–247.
- 5 M. Grätzel, Perspectives for dye-sensitized nanocrystalline solar cells, *Prog. Photovoltaics*, 2000, **8**, 171–185.



6 M. K. Hara and H. Arakawa, Dye-sensitized solar cells, *Handbook of Photovoltaic Science and Engineering*, ed. A. Luque and S. Hegedus, Wiley, New York, 2003, pp. 663–700.

7 M. Grätzel, Dye-sensitized solar cells, *J. Photochem. Photobiol. C*, 2003, **4**, 145–153.

8 B. E. Hardin, H. J. Snaith and M. D. McGehee, The renaissance of dye-sensitized solar cells, *Nat. Photonics*, 2012, **6**, 162–169.

9 J. H. Yum, E. Baranoff, S. Wenger, M. K. Nazeeruddin and M. Grätzel, Panchromatic engineering for dye-sensitized solar cells, *Energy Environ. Sci.*, 2011, **4**, 842–857.

10 T. Prakash, Review on nanostructured semiconductors for dye sensitized solar cells, *Electron. Mater. Lett.*, 2012, **8**, 231–243.

11 G. Boschloo and A. Hagfeldt, Characteristics of the iodide/triiodide redox mediator in dye-sensitized solar cells, *Acc. Chem. Res.*, 2009, **42**, 1819–1826.

12 A. Hagfeldt, G. Boschloo, L. Sun, L. Kloo and H. Pettersson, Dye-sensitized solar cells, *Chem. Rev.*, 2010, **110**, 6595–6663.

13 Q. Zhang and G. Cao, Nanostructured photoelectrodes for dye-sensitized solar cells, *Nano Today*, 2011, **6**, 91–109.

14 S. Zhang, X. Yang, Y. Numata and L. Han, Highly efficient dye-sensitized solar cells: progress and future challenges, *Energy Environ. Sci.*, 2013, **6**, 1443–1464.

15 N. Tétreault and M. Grätzel, Novel nanostructures for next generation dye-sensitized solar cells, *Energy Environ. Sci.*, 2012, **5**, 8506–8516.

16 A. Listorti, B. O'Regan and J. R. Durrant, Electron transfer dynamics in dye-sensitized solar cells, *Chem. Mater.*, 2011, **23**, 3381–3399.

17 M. Ye, X. Wen, M. Wang, J. Iocozzia, N. Zhang, C. Lin and Z. Lin, Recent advances in dye-sensitized solar cells: from photoanodes, sensitizers and electrolytes to counter electrodes, *Mater. Today*, 2015, **18**, 155–162.

18 (a) M. Wu, X. Lin, Y. Wang, L. Wang, W. Guo, D. Qi, X. Peng, A. Hagfeldt, M. Grätzel and T. Ma, Economical Pt-free catalysts for counter electrodes of dye-sensitized solar cells, *J. Am. Chem. Soc.*, 2012, **134**, 3419–3428; (b) F. Hao, P. Dong, Q. Luo, J. Li, J. Lou and H. Lin, Recent advances in alternative cathode materials for iodine-free dye-sensitized solar cells, *Energy Environ. Sci.*, 2013, **6**, 2003–2019.

19 (a) A. C. Cakir and S. Erten-Ela, Comparison between synthesis techniques to obtain ZnO nanorods and its effect on dye sensitized solar cells, *Adv. Powder Technol.*, 2012, **23**, 655–660; (b) Y. Çakmak, S. Kolemen, M. Buyuktemiz, Y. Dede and S. Erten-Ela, Synthesis and dye sensitized solar cell applications of Bodipy derivatives with bis-dimethylfluorenyl amine donor groups, *New J. Chem.*, 2015, **39**, 4086–4092.

20 (a) S. Erten-Ela, S. Cogal, G. C. Cogal and A. U. Oksuz, Highly conductive polymer materials based multi-walled carbon nanotubes as counter electrodes for dye-sensitized solar cells, *Fullerenes, Nanotubes, Carbon Nanostruct.*, 2016, **24**, 380–384; (b) M. Wu and T. Ma, Recent progress of counter electrode catalysts in dye-sensitized solar cells, *J. Phys. Chem. C*, 2014, **118**, 16727–16742.

21 S. Thomas, T. G. Deepak, G. S. Anjusree, T. A. Arun, S. V. Nair and A. S. Nair, A review on counter electrode materials in dye-sensitized solar cells, *J. Mater. Chem. A*, 2014, **2**, 4474–4490.

22 (a) *Encyclopedia of Nanoscience and Nanotechnology*; 10-volume set, ed. H. S. Nalwa, American Scientific Publishers, Los Angeles, 2004; (b) *Handbook of Nanostructured Materials and Nanotechnology*; 5-volume set, ed. H. S. Nalwa, Academic Press, San Diego, 2000; (c) *Nanomaterials for Energy Storage Applications*, ed. H. S. Nalwa, American Scientific Publishers, Los Angeles, 2009.

23 T. E. Graedel, E. M. Harper, N. T. Nassar, P. Nuss and B. K. Reck, Criticality of metals and metalloids, *Proc. Natl. Acad. Sci. U. S. A.*, 2015, **112**, 4257–4262, DOI: 10.1073/pnas.1500415112.

24 *Minerals, Critical Minerals, and the U.S. Economy*, National Research Council, National Academies Press, Washington D.C., U.S., 2008; *Assessments of Criticality*, National Research Council (US) Chemical Sciences Roundtable, 2012.

25 E. Singh and H. S. Nalwa, Graphene-based dye-sensitized solar cells: a review, *Sci. Adv. Mater.*, 2015, **7**, 1863–1912.

26 E. Singh and H. S. Nalwa, Graphene-based bulk-heterojunction solar cells: a review, *J. Nanosci. Nanotechnol.*, 2015, **15**, 6237–6278.

27 E. Singh and H. S. Nalwa, Stability of graphene-based heterojunction solar cells, *RSC Adv.*, 2015, **5**, 73575–73600.

28 J. A. Wilson and A. D. Yoffe, The transition metal dichalcogenides discussion and interpretation of the observed optical, electrical and structural properties, *Adv. Phys.*, 1969, **18**, 193–335.

29 X. Huang, Z. Zeng and H. Zhang, Metal dichalcogenide nanosheets: preparation, properties and applications, *Chem. Soc. Rev.*, 2013, **42**, 1934–1946.

30 M. Chhowalla, H. S. Shin, G. Eda, L. J. Li, K. P. Loh and H. Zhang, The chemistry of two-dimensional layered transition metal dichalcogenide nanosheets, *Nat. Chem.*, 2013, **5**, 263–275.

31 C. Ataca, H. Sahin and S. Ciraci, Stable, single-layer MX_2 transition-metal oxides and dichalcogenides in a honeycomb-like structure, *J. Phys. Chem. C*, 2012, **116**, 8983–8999.

32 A. K. Geim and I. V. Grigorieva, van der Waals heterostructures, *Nature*, 2013, **499**, 419–425.

33 B. Radisavljevic, A. Radenovic, J. Brivio, V. Giacometti and A. Kis, Single-layer MoS_2 transistors, *Nat. Nanotechnol.*, 2011, **6**, 147–150.

34 W. S. Yun, S. W. Han, S. C. Hong, I. G. Kim and J. D. Lee, Thickness and strain effects on electronic structures of transition metal dichalcogenides: $2H-MX_2$ semiconductors ($M = Mo, W$; $X = S, Se, Te$), *Phys. Rev. B: Condens. Matter Mater. Phys.*, 2012, **85**, 033305.

35 G. Eda and S. A. Maier, Two-Dimensional Crystals: Managing Light for Optoelectronics, *ACS Nano*, 2013, **7**, 5660–5665.

36 S. Tongay, J. Suh, C. Ataca, W. Fan, A. Luce, J. S. Kang, J. Liu, C. Ko, R. Raghunathanan, J. Zhou, F. Ogletree, J. Li,



J. C. Grossman and J. Wu, Defects activated photoluminescence in two-dimensional semiconductors: interplay between bound, charged, and free excitons, *Sci. Rep.*, 2013, **3**, 2657.

37 P. Tonndorf, R. Schmidt, P. Böttger, X. Zhang, J. Borner, A. Liebig, M. Albrecht, C. Kloc, O. Gorgan, D. R. T. Zahn, S. M. de Vasconcellos and R. Bratschitsch, Photoluminescence Emission and Raman Response of Monolayer MoS₂, MoSe₂, and WSe₂, *Opt. Express*, 2013, **21**, 4908–4916.

38 K. M. McCreary, A. T. Hanbicki, G. G. Jernigan, J. C. Culbertson and B. T. Jonker, Synthesis of large-area WS₂ monolayers with exceptional photoluminescence, *Sci. Rep.*, 2016, **6**, 19159.

39 K. Ueno, K. Saiki, T. Shimada and A. Koma, Epitaxial growth of transition metal dichalcogenides on cleaved faces of mica, *J. Vac. Sci. Technol., A*, 1990, **8**, 68–72.

40 K. S. Novoselov, D. Jiang, F. Schedin, T. J. Booth, V. V. Khotkevich, S. V. Morozov and A. K. Geim, Two-dimensional atomic crystals, *Proc. Natl. Acad. Sci. U. S. A.*, 2005, **102**, 10451–10453.

41 H. Li, G. Lu, Y. Wang, Z. Yin, C. Cong, Q. He, L. Wang, F. Ding, T. Yu and H. Zhang, Mechanical Exfoliation and Characterization of Single-and Few-Layer Nanosheets of WSe₂, TaS₂, and TaSe₂, *Small*, 2013, **9**, 1974–1981.

42 A. A. Al-Hilli and B. L. Evans, The preparation and properties of transition metal dichalcogenide single crystals, *J. Cryst. Growth*, 1972, **15**, 93–101.

43 Y. H. Lee, L. Yu, H. Wang, W. Fang, X. Ling, Y. Shi, C. T. Lin, J. K. Huang, M. T. Chang, C. S. Chang, M. Dresselhaus, T. Palacios, L. J. Li and J. Kong, Synthesis and transfer of single-layer transition metal disulfides on diverse surfaces, *Nano Lett.*, 2013, **13**, 1852–1857.

44 Y. Shi, H. Li and L. J. Li, Recent advances in controlled synthesis of two-dimensional transition metal dichalcogenides *via* vapour deposition techniques, *Chem. Soc. Rev.*, 2015, **44**, 2744–2756.

45 R. Gatensby, N. McEvoy, K. Lee, T. Hallam, N. C. Berner, E. Rezvani, S. Winters, M. O'Brien and G. S. Duesberg, Controlled synthesis of transition metal dichalcogenide thin films for electronic applications, *Appl. Surf. Sci.*, 2015, **297**, 139–146.

46 S. Jeong, D. Yoo, J. T. Jang, M. Kim and J. Cheon, Well-defined colloidal 2-D layered transition-metal chalcogenide nanocrystals *via* generalized synthetic protocols, *J. Am. Chem. Soc.*, 2012, **134**, 18233–18236.

47 M. S. Whittingham and F. R. Gamble, The lithium intercalates of the transition metal dichalcogenides, *Mater. Res. Bull.*, 1975, **10**, 363–371.

48 Z. Zeng, T. Sun, J. Zhu, X. Huang, Z. Yin, G. Lu, Z. Fan, Q. Yan, H. H. Hng and H. Zhang, An Effective Method for the Fabrication of Few-Layer-Thick Inorganic Nanosheets, *Angew. Chem., Int. Ed.*, 2012, **51**, 9052–9056.

49 A. Y. S. Eng, A. Ambrosi, Z. Sofer, P. Simek and M. Pumera, Electrochemistry of transition metal dichalcogenides: strong dependence on the metal-to-chalcogen composition and exfoliation method, *ACS Nano*, 2014, **8**, 12185–12198.

50 R. A. Gordon, D. Yang, E. D. Crozier, D. T. Jiang and R. F. Frindt, Structures of exfoliated single layers of WS₂, MoS₂, and MoSe₂ in aqueous suspension, *Phys. Rev. B: Condens. Matter Mater. Phys.*, 2002, **65**, 125407.

51 G. Cunningham, M. Lotya, C. S. Cucinotta, S. Sanvito, S. D. Bergin, R. Menzel, M. S. Shaffer and J. N. Coleman, Solvent exfoliation of transition metal dichalcogenides: dispersibility of exfoliated nanosheets varies only weakly between compounds, *ACS Nano*, 2012, **6**, 3468–3480.

52 R. J. Smith, P. J. King, M. Lotya, C. Wirtz, U. Khan, S. De, A. O'Neill, G. S. Duesberg, J. C. Grunlan, G. Moriarty and J. Chen, Large-scale exfoliation of inorganic layered compounds in aqueous surfactant solutions, *Adv. Mater.*, 2011, **23**, 3944–3948.

53 V. Nicolosi, M. Chhowalla, M. G. Kanatzidis, M. S. Strano and J. N. Coleman, Liquid exfoliation of layered materials, *Science*, 2013, **340**, 1226419.

54 J. N. Coleman, M. Lotya, A. O'Neill, S. D. Bergin, P. J. King, U. Khan, K. Young, A. Gaucher, S. De, R. J. Smith, I. V. Shvets, S. K. Arora, G. Stanton, H. Y. Kim, K. Lee, G. Kim, G. S. Duesberg, T. Hallam, J. J. Boland, J. J. Wang, J. F. Donegan, J. C. Grunlan, G. Moriarty, A. Shmeliov, R. J. Nicholls, J. M. Perkins, E. M. Grieveson, K. Theuwissen, D. W. McComb, P. D. Nellist and V. Nicolosi, Two-dimensional nanosheets produced by liquid exfoliation of layered materials, *Science*, 2011, **331**, 568–571.

55 L. Niu, K. Li, H. Zhen, Y. S. Chui, W. Zhang, F. Yan and Z. Zheng, Salt-Assisted High-Throughput Synthesis of Single-and Few-Layer Transition Metal Dichalcogenides and Their Application in Organic Solar Cells, *Small*, 2014, **10**, 4651–4657.

56 X. Zhang, X. F. Qiao, W. Shi, J. B. Wu, D. S. Jiang and P. H. Tan, Phonon and Raman scattering of two-dimensional transition metal dichalcogenides from monolayer, multilayer to bulk material, *Chem. Soc. Rev.*, 2015, **44**, 2757–2785.

57 A. S. Pawbake, M. S. Pawar, S. R. Jadkar and D. J. Late, Large area chemical vapor deposition of monolayer transition metal dichalcogenides and their temperature dependent Raman spectroscopy studies, *Nanoscale*, 2016, **8**, 3008–3018.

58 J. L. Verble and T. J. Wieting, Lattice Mode Degeneracy in MoS₂ and Other Layer Compounds, *Phys. Rev. Lett.*, 1970, **25**, 362.

59 G. Frey, R. Tenne, M. Matthews, M. Dresselhaus and G. Dresselhaus, Raman and resonance Raman investigation of MoS₂ nanoparticles, *Phys. Rev. B: Condens. Matter Mater. Phys.*, 1999, **60**, 2883–2892.

60 A. Castellanos-Gomez, J. Quereda, H. P. van der Meulen, N. Agrait and G. Rubio-Bollinger, Spatially resolved optical absorption spectroscopy of single-and few-layer MoS₂ by hyperspectral imaging, *Nanotechnology*, 2016, **27**, 115705.



61 S. K. Balasingam, J. S. Lee and Y. Jun, Few-layered MoSe₂ nanosheets as an advanced electrode material for supercapacitors, *Dalton Trans.*, 2015, **44**, 15491–15498.

62 W. Zhao, Z. Ghorannevis, K. K. Amara, J. R. Pang, M. Toh, X. Zhang, C. Kloc, P. H. Tan and G. Eda, Lattice dynamics in mono-and few-layer sheets of WS₂ and WSe₂, *Nanoscale*, 2013, **5**, 9677–9683.

63 C. Lee, H. Yan, L. E. Brus, T. F. Heinz, J. Hone and S. Ryu, Anomalous Lattice Vibrations of Single- and Few-Layer MoS₂, *ACS Nano*, 2010, **4**, 2695–2700.

64 A. Molina-Sanchez and L. Wirtz, Phonons in single-layer and few-layer MoS₂ and WS₂, *Phys. Rev. B: Condens. Matter Mater. Phys.*, 2011, **84**, 155413.

65 S. Tongay, J. Zhou, C. Ataca, K. Lo, T. S. Matthews, J. Li, J. C. Grossman and J. Wu, Thermally Driven Crossover from Indirect toward Direct Bandgap in 2D Semiconductors: MoSe₂ versus MoS₂, *Nano Lett.*, 2012, **12**, 5576–5580.

66 H. Li, Q. Zhang, C. C. R. Yap, B. K. Tay, T. H. T. Edwin, A. Olivier and D. Baillargeat, From Bulk to Monolayer MoS₂: Evolution of Raman Scattering, *Adv. Funct. Mater.*, 2012, **22**, 1385–1390.

67 A. Berkdemir, H. R. Gutierrez, A. R. Botello-Mendez, N. Perea-Lopez, A. L. Elias, C. I. Chia, B. Wang, V. H. Crespi, F. Lopez-Urias, J. C. Charlier, H. Terrones and M. Terrones, Identification of individual and few layers of WS₂ using Raman Spectroscopy, *Sci. Rep.*, 2013, **3**, 1755, DOI: 10.1038/srep01755.

68 H. Sahin, S. Tongay, S. Horzum, W. Fan, J. Zhou, J. Li, J. Wu and F. M. Peeters, Anomalous Raman spectra and thickness-dependent electronic properties of WSe₂, *Phys. Rev. B: Condens. Matter Mater. Phys.*, 2013, **87**, 165409.

69 R. Saito, Y. Tatsumi, S. Huang, X. Ling and M. S. Dresselhaus, Raman spectroscopy of transition metal dichalcogenides, *J. Phys.: Condens. Matter*, 2016, **28**, 353002.

70 H. Terrones, E. Del Corro, S. Feng, J. M. Poumirol, D. Rhodes, D. Smirnov, N. R. Pradhan, Z. Lin, M. A. T. Nguyen, A. L. Elias and T. E. Mallouk, New first order Raman-active modes in few layered transition metal dichalcogenides, *Sci. Rep.*, 2014, **4**, 4215.

71 S. Y. Chen, C. Zheng, M. S. Fuhrer and J. Yan, Helicity-resolved Raman scattering of MoS₂, MoSe₂, WS₂, and WSe₂ atomic layers, *Nano Lett.*, 2015, **15**, 2526–2532.

72 P. D. Fleischauer and R. Bauer, Chemical and structural effects on the lubrication properties of sputtered MoS₂ films, *Tribol. Trans.*, 1988, **31**, 239–250.

73 T. Spalvins, Lubrication with sputtered MoS₂ films: principles, operation, and limitations, *J. Mater. Eng. Perform.*, 1992, **1**, 347–351.

74 M. R. Hilton, R. Bauer, S. V. Didziulis, M. T. Dugger, J. M. Keem and J. Scholhamer, Structural and tribological studies of MoS₂ solid lubricant films having tailored metal-multilayer nanostructures, *Surf. Coat. Technol.*, 1992, **53**, 13–23.

75 A. Savan, E. Pflüger, P. Voumard, A. Schröer and M. Simmonds, Modern solid lubrication: recent developments and applications of MoS₂, *Lubr. Sci.*, 2000, **12**, 185–203.

76 L. Rapoport, Y. Bilik, Y. Feldman, M. Homyonfer, S. R. Cohen and R. Tenne, Hollow nanoparticles of WS₂ as potential solid-state lubricants, *Nature*, 1997, **387**, 791–793.

77 L. Rapoport, N. Fleischer and R. Tenne, Fullerene-like WS₂ Nanoparticles: Superior Lubricants for Harsh Conditions, *Adv. Mater.*, 2003, **15**, 651–655.

78 Y. Q. Liu, C. S. Li, J. H. Yang, Y. M. Yu and X. K. Li, Synthesis and tribological properties of tubular NbS₂ and TaS₂ nanostructures, *Chin. J. Chem. Phys.*, 2007, **20**, 768–772.

79 T. Polcar and A. Cavaleiro, Review on self-lubricant transition metal dichalcogenide nanocomposite coatings alloyed with carbon, *Surf. Coat. Technol.*, 2011, **206**, 686–695.

80 J. F. Yang, B. Parakash, J. Hardell and Q. F. Fang, Tribological properties of transition metal dichalcogenide based lubricant coatings, *Front. Mater. Sci.*, 2012, **6**, 116–127.

81 D. Krasnozhon, D. Lembke, C. Nyffeler, Y. Leblebici and A. Kis, MoS₂ transistors operating at gigahertz frequencies, *Nano Lett.*, 2014, **14**, 5905–5911.

82 H. Fang, S. Chuang, T. C. Chang, K. Takei, T. Takahashi and A. Javey, High-performance single layered WSe₂ p-FETs with chemically doped contacts, *Nano Lett.*, 2012, **12**, 3788–3792.

83 H. Wang, L. Yu, Y. H. Lee, Y. Shi, A. Hsu, M. L. Chin, L. J. Li, M. Dubey, J. Kong and T. Palacios, Integrated circuits based on bilayer MoS₂ transistors, *Nano Lett.*, 2012, **12**, 4674–4680.

84 H. Li, J. Wu, Z. Yin and H. Zhang, Preparation and applications of mechanically exfoliated single-layer and multilayer MoS₂ and WSe₂ nanosheets, *Acc. Chem. Res.*, 2014, **47**, 1067–1075.

85 C. Gong, H. Zhang, W. Wang, L. Colombo, R. M. Wallace and K. Cho, Band alignment of two-dimensional transition metal dichalcogenides: application in tunnel field effect transistors, *Appl. Phys. Lett.*, 2013, **103**, 053513.

86 D. Jariwala, V. K. Sangwan, L. J. Lauhon, T. J. Marks and M. C. Hersam, Emerging device applications for semiconducting two-dimensional transition metal dichalcogenides, *ACS Nano*, 2014, **8**, 1102–1120.

87 F. Schwierz, J. Pezoldt and R. Gratzner, Two-dimensional materials and their prospects in transistor electronics, *Nanoscale*, 2015, **7**, 8261–8283.

88 H. Y. Chang, S. Yang, J. Lee, L. Tao, W. S. Hwang, D. Jena, N. Lu and D. Akinwande, High-performance, highly bendable MoS₂ transistors with high-k dielectrics for flexible low-power systems, *ACS Nano*, 2013, **7**, 5446–5452.

89 R. Cheng, S. Jiang, Y. Chen, Y. Liu, N. Weiss, H. C. Cheng, H. Wu, Y. Huang and X. Duan, Few-layer molybdenum disulfide transistors and circuits for high-speed flexible electronics, *Nat. Commun.*, 2014, **5**, 5143.

90 W. S. Hwang, M. Remskar, R. Yan, V. Protasenko, K. Tahy, S. D. Chae, P. Zhao, A. Konar, H. G. Xing, A. Seabaugh and D. Jena, Transistors with chemically synthesized layered semiconductor WS₂ exhibiting 10⁵ room temperature





modulation and ambipolar behavior, *Appl. Phys. Lett.*, 2012, **101**, 013107.

91 M. Tosun, S. Chuang, H. Fang, A. B. Sachid, M. Hettick, Y. Lin, Y. Zeng and A. Javey, High-gain inverters based on WSe₂ complementary field-effect transistors, *ACS Nano*, 2014, **8**, 4948–4953.

92 S. Larentis, B. Fallahazad and E. Tutuc, Field-effect transistors and intrinsic mobility in ultra-thin MoSe₂ layers, *Appl. Phys. Lett.*, 2012, **101**, 223104.

93 B. Chamlagain, Q. Li, N. J. Ghimire, H. J. Chuang, M. M. Perera, H. Tu, Y. Xu, M. Pan, D. Xaio, J. Yan and D. Mandrus, Mobility improvement and temperature dependence in MoSe₂ field-effect transistors on polyethylene-C substrate, *ACS Nano*, 2014, **8**, 5079–5088.

94 S. Fathipour, N. Ma, W. S. Hwang, V. Protasenko, S. Vishwanath, H. G. Xing, H. Xu, D. Jena, J. Appenzeller and A. Seabaugh, Exfoliated multilayer MoTe₂ field-effect transistors, *Appl. Phys. Lett.*, 2014, **105**, 192101.

95 Y. F. Lin, Y. Xu, S. T. Wang, S. L. Li, M. Yamamoto, A. Aparecido-Ferreira, W. Li, H. Sun, S. Nakaharai, W. B. Jian and K. Ueno, Ambipolar MoTe₂ transistors and their applications in logic circuits, *Adv. Mater.*, 2014, **26**, 3263–3269.

96 E. Liu, Y. Fu, Y. Wang, Y. Feng, H. Liu, X. Wan, W. Zhou, B. Wang, L. Shao, C. H. Ho and Y. S. Huang, Integrated digital inverters based on two-dimensional anisotropic ReS₂ field-effect transistors, *Nat. Commun.*, 2015, **6**, 6991.

97 D. Gao, Q. Xue, X. Mao, W. Wang, Q. Xu and D. Xue, Ferromagnetism in ultrathin VS₂ nanosheets, *J. Mater. Chem. C*, 2013, **1**, 5909–5916.

98 T. Kanazawa, T. Amemiya, A. Ishikawa, V. Upadhyaya, K. Tsuruta, T. Tanaka and Y. Miyamoto, Few-layer HfS₂ transistors, *Sci. Rep.*, 2016, **6**, 22277.

99 (a) M. S. El-Bana, D. Wolverson, S. Russo, G. Balakrishnan, D. M. Paul and S. J. Bending, Superconductivity in two-dimensional NbSe₂ field effect transistors, *Supercond. Sci. Technol.*, 2013, **26**, 125020; (b) S. Yang, Q. Yue, H. Cai, K. Wu, C. Jiang and S. Tongay, Highly efficient gas molecule-tunable few-layer GaSe phototransistors, *J. Mater. Chem. C*, 2016, **4**, 248–253.

100 X. Geng, Y. Yu, X. Zhou, C. Wang, K. Xu, Y. Zhang, C. Wu, L. Wang, Y. Jiang and Q. Yang, Design and construction of ultra-thin MoSe₂ nanosheet-based heterojunction for high-speed and low-noise photodetection, *Nano Res.*, 2016, **9**, 2641–2651.

101 E. Zhang, Y. Jin, X. Yuan, W. Wang, C. Zhang, L. Tang, S. Liu, P. Zhou, W. Hu and F. Xiu, ReS₂-Based Field-Effect Transistors and Photodetectors, *Adv. Funct. Mater.*, 2015, **25**, 4076–4082.

102 S. Yang, C. Wang, C. Ataca, Y. Li, H. Chen, H. Cai, A. Suslu, J. C. Grossman, C. Jiang, Q. Liu and S. Tongay, Self-Driven Photodetector and Ambipolar Transistor in Atomically Thin GaTe-MoS₂ p-n vdW Heterostructure, *ACS Appl. Mater. Interfaces*, 2016, **8**, 2533–2539.

103 J. S. Ross, P. Klement, A. M. Jones, N. J. Ghimire, J. Yan, D. G. Mandrus, T. Taniguchi, K. Watanabe, K. Kitamura, W. Yao and D. H. Cobden, Electrically tunable excitonic light-emitting diodes based on monolayer WSe₂ pn junctions, *Nat. Nanotechnol.*, 2014, **9**, 268–272.

104 Z. Yin, X. Zhang, Y. Cai, J. Chen, J. I. Wong, Y. Y. Tay, J. Chai, J. Wu, Z. Zeng, B. Zheng and H. Y. Yang, Preparation of MoS₂-MoO₃ Hybrid Nanomaterials for Light-Emitting Diodes, *Angew. Chem., Int. Ed.*, 2014, **53**, 12560–12565.

105 A. Lipatov, P. Sharma, A. Gruverman and A. Sinitskii, Optoelectrical Molybdenum Disulfide (MoS₂)-Ferroelectric Memories, *ACS Nano*, 2015, **9**, 8089–8098.

106 J. Lee, Z. Wang, K. He, J. Shan and P. X. L. Feng, High frequency MoS₂ nanomechanical resonators, *ACS Nano*, 2013, **7**, 6086–6091.

107 F. Clerici, M. Fontana, S. Bianco, M. Serrapede, F. Perrucci, S. Ferrero, E. Tresso and A. Lamberti, *In situ* MoS₂ Decoration of Laser-Induced Graphene as Flexible Supercapacitor Electrodes, *ACS Appl. Mater. Interfaces*, 2016, **8**, 10459–10465.

108 X. Zhou, B. Xu, Z. Lin, D. Shu and L. Ma, Hydrothermal Synthesis of Flower-Like MoS₂ Nanospheres for Electrochemical Supercapacitors, *J. Nanosci. Nanotechnol.*, 2014, **14**, 7250–7254.

109 G. Du, Z. Guo, S. Wang, R. Zeng, Z. Chen and H. Liu, Superior Stability and High Capacity of Restacked Molybdenum Disulfide as Anode Material for Lithium Ion Batteries, *Chem. Commun.*, 2010, **46**, 1106–1108.

110 Z. Zhang, X. Shi, X. Yang, Y. Fu, K. Zhang, Y. Lai and J. Li, Nanoctahedra particles assembled FeSe₂ microspheres embedded into sulfur-doped reduced graphene oxide sheets as a promising anode for sodium ion batteries, *ACS Appl. Mater. Interfaces*, 2016, **8**, 13849–13856.

111 X. Xu, C. S. Rout, J. Yang, R. Cao, P. Oh, H. S. Shin and J. Cho, Freeze-dried WS₂ composites with low content of graphene as high-rate lithium storage materials, *J. Mater. Chem. A*, 2013, **1**, 14548–14554.

112 O. Lopez-Sanchez, E. Alarcon Llado, V. Koman, A. Fontcuberta i Morral, A. Radenovic and A. Kis, Light Generation and Harvesting in a van der Waals Heterostructure, *ACS Nano*, 2014, **8**, 3042–3048.

113 F. K. Perkins, A. L. Friedman, E. Cobas, P. M. Campbell, G. G. Jernigan and B. T. Jonker, Chemical vapor sensing with monolayer MoS₂, *Nano Lett.*, 2013, **13**, 668–673.

114 D. J. Late, T. Doneux and M. Bougouma, Single-layer MoSe₂ based NH₃ gas sensor, *Appl. Phys. Lett.*, 2014, **105**, 233103.

115 T. Wang, R. Zhu, J. Zhuo, Z. Zhu, Y. Shao and M. Li, Direct detection of DNA below ppb level based on thionin-functionalized layered MoS₂ electrochemical sensors, *Anal. Chem.*, 2014, **86**, 12064–12069.

116 M. Pumera and A. H. Loo, Layered transition-metal dichalcogenides (MoS₂ and WS₂) for sensing and biosensing, *TrAC, Trends Anal. Chem.*, 2014, **61**, 49–53.

117 Z. Li and S. L. Wong, Functionalization of 2D transition metal dichalcogenides for biomedical applications, *Mater. Sci. Eng., C*, 2016, **70**, 1095–1106.

118 E. Singh, K. S. Kim, G. Y. Yeom and H. S. Nalwa, Atomically thin-layered molybdenum disulfide (MoS₂) for bulk-

heterojunction solar cells, *ACS Appl. Mater. Interfaces*, 2017, **9**, 3223–3245.

119 (a) K. S. Kim, K. H. Kim, Y. Nam, J. Jeon, S. Yim, E. Singh, J. Y. Lee, S. Lee, Y. S. Jung, G. Y. Yeom and D. W. Kim, Atomic Layer Etching Mechanism of MoS₂ for Nanodevices, *ACS Appl. Mater. Interfaces*, 2017, **9**, 11967–11976; (b) Q. H. Wang, K. Kalantar-Zadeh, A. Kis, J. N. Coleman and M. S. Strano, Electronics and optoelectronics of two-dimensional transition metal dichalcogenides, *Nat. Nanotechnol.*, 2012, **7**, 699–712.

120 K. F. Mak and J. Shan, Photonics and optoelectronics of 2D semiconductor transition metal dichalcogenides, *Nat. Photonics*, 2016, **10**, 216–226.

121 J. U. Lee, K. Kim, S. Han, G. H. Ryu, Z. Lee and H. Cheong, Raman Signatures of Polytypism in Molybdenum Disulfide, *ACS Nano*, 2016, **10**, 1948–1953.

122 A. R. Beal, J. C. Knights and W. Y. Liang, Transmission spectra of some transition metal dichalcogenides II. Group VIA: trigonal prismatic coordination, *J. Phys. C: Solid State Phys.*, 1972, **5**, 3540.

123 J. A. Woollam and R. B. Somoano, Superconducting critical fields of alkali and alkaline-earth intercalates of MoS₂, *Phys. Rev. B: Solid State*, 1976, **13**, 3843.

124 F. Wypych and R. Schöllhorn, 1T-MoS₂, a new metallic modification of molybdenum disulfide, *J. Chem. Soc., Chem. Commun.*, 1992, 1386–1388.

125 L. Wang, Z. Xu, W. Wang and X. Bai, Atomic mechanism of dynamic electrochemical lithiation processes of MoS₂ nanosheets, *J. Am. Chem. Soc.*, 2014, **136**, 6693–6697.

126 S. N. Shirodkar and U. V. Waghmare, Emergence of Ferroelectricity at a Metal-Semiconductor Transition in a 1T Monolayer of MoS₂, *Phys. Rev. Lett.*, 2014, **112**, 157601.

127 M. Acerce, D. Voiry and M. Chhowalla, Metallic 1T phase MoS₂ nanosheets as supercapacitor electrode materials, *Nat. Nanotechnol.*, 2015, **10**, 313–318.

128 P. Cheng, K. Sun and Y. H. Hu, Memristive Behavior and Ideal Memristor of 1T Phase MoS₂ Nanosheets, *Nano Lett.*, 2015, **16**, 572–576.

129 R. Kappera, D. Voiry, S. E. Yalcin, B. Branch, G. Gupta, A. D. Mohite and M. Chhowalla, Phase-engineered low-resistance contacts for ultrathin MoS₂ transistors, *Nat. Mater.*, 2014, **13**, 1128–1134.

130 W. Wei, K. Sun and Y. H. Hu, An efficient counter electrode material for dye-sensitized solar cells—flower-structured 1T metallic phase MoS₂, *J. Mater. Chem. A*, 2016, **4**, 12398–12401.

131 R. S. Infant, X. Xu, W. Yang, F. Yang, L. Hou and Y. Li, Highly active and reflective MoS₂ counter electrode for enhancement of photovoltaic efficiency of dye sensitized solar cells, *Electrochim. Acta*, 2016, **212**, 614–620.

132 S. Jiang, X. Yin, J. Zhang, X. Zhu, J. Li and M. He, Vertical ultrathin MoS₂ nanosheets on a flexible substrate as an efficient counter electrode for dye-sensitized solar cells, *Nanoscale*, 2015, **7**, 10459–10464.

133 B. Lei, G. R. Li and X. P. Gao, Morphology dependence of molybdenum disulfide transparent counter electrode in dye-sensitized solar cells, *J. Mater. Chem. A*, 2014, **2**, 3919–3925.

134 J. Zhang, S. Najmaei, H. Lin and J. Lou, MoS₂ atomic layers with artificial active edge sites as transparent counter electrodes for improved performance of dye-sensitized solar cells, *Nanoscale*, 2014, **6**, 5279–5283.

135 M. Al-Mamun, H. Zhang, P. Liu, Y. Wang, J. Cao and H. Zhao, Directly hydrothermal growth of ultrathin MoS₂ nanostructured films as high performance counter electrodes for dye-sensitised solar cells, *RSC Adv.*, 2014, **4**, 21277–21283.

136 C. K. Cheng and C. K. Hsieh, Electrochemical deposition of molybdenum sulfide thin films on conductive plastic substrates as platinum-free flexible counter electrodes for dye-sensitized solar cells, *Thin Solid Films*, 2015, **584**, 52–60.

137 C. H. Lin, C. H. Tsai, F. G. Tseng, Y. Y. Yu, H. C. Wu and C. K. Hsieh, Low-Temperature Thermally Reduced Molybdenum Disulfide as a Pt-Free Counter Electrode for Dye-Sensitized Solar Cells, *Nanoscale Res. Lett.*, 2015, **10**, 1–10.

138 S. A. Patil, P. Y. Kalode, R. S. Mane, D. V. Shinde, A. Doyoung, C. Keumnam, M. M. Sung, S. B. Ambade and S. H. Han, Highly efficient and stable DSSCs of wet-chemically synthesized MoS₂ counter electrode, *Dalton Trans.*, 2014, **43**, 5256–5259.

139 W. H. Jhang and Y. J. Lin, Overpotential modification at the MoS₂ counter electrode/electrolyte interfaces by thermal annealing resulting improvement in photovoltaic performance of dye-sensitized solar cells, *J. Mater. Sci.: Mater. Electron.*, 2015, **26**, 3739–3743.

140 A. Antonelou, G. Syrrokostas, L. Sygellou, G. Leftheriotis, V. Dracopoulos and S. N. Yannopoulos, Facile, substrate-scale growth of mono-and few-layer homogeneous MoS₂ films on Mo foils with enhanced catalytic activity as counter electrodes in DSSCs, *Nanotechnology*, 2015, **27**, 045404.

141 M. Wu, Y. Wang, X. Lin, N. Yu, L. Wang, L. Wang, A. Hagfeldt and T. Ma, Economical and effective sulfide catalysts for dye-sensitized solar cells as counter electrodes, *Phys. Chem. Chem. Phys.*, 2011, **13**, 19298–19301.

142 H. Zhang, J. Choi, A. Ramani, D. Voiry, S. N. Natoli, M. Chhowalla, D. R. McMillin and J. H. Choi, Engineering Chemically Exfoliated Large-Area Two-Dimensional MoS₂ Nanolayers with Porphyrins for Improved Light Harvesting, *ChemPhysChem*, 2016, **17**, 2854–2862.

143 W. Liu, S. He, T. Yang, Y. Feng, G. Qian, J. Xu and S. Miao, TEOS-assisted synthesis of porous MoS₂ with ultra-small exfoliated sheets and applications in dye-sensitized solar cells, *Appl. Surf. Sci.*, 2014, **313**, 498–503.

144 S. S. Kim, J. W. Lee, J. M. Yun and S. I. Na, 2-Dimensional MoS₂ nanosheets as transparent and highly electrocatalytic counter electrode in dye-sensitized solar cells: effect of thermal treatments, *J. Ind. Eng. Chem.*, 2015, **29**, 71–77.

145 S. Hussain, S. F. Shaikh, D. Vikraman, R. S. Mane, O. S. Joo, M. Naushad and J. Jung, High-Performance Platinum-Free



Dye-Sensitized Solar Cells with Molybdenum Disulfide Films as Counter Electrodes, *ChemPhysChem*, 2015, **16**, 3959–3965.

146 H. Jeong, J. Y. Kim, B. Koo, H. J. Son, D. Kim and M. J. Ko, Rapid sintering of MoS₂ counter electrode using near-infrared pulsed laser for use in highly efficient dye-sensitized solar cells, *J. Power Sources*, 2016, **330**, 104–110.

147 J. Liang, J. Li, H. Zhu, Y. Han, Y. Wang, C. Wang, Z. Jin, G. Zhang and J. Liu, One-step fabrication of large-area ultrathin MoS₂ nanofilms with high catalytic activity for photovoltaic devices, *Nanoscale*, 2016, **8**, 16017–16025.

148 C. Tan, W. Zhao, A. Chaturvedi, Z. Fei, Z. Zeng, J. Chen, Y. Huang, P. Ercius, Z. Luo, X. Qi and B. Chen, Preparation of Single-Layer Mo₂xSe₂(1 – x) and Mo_xW_{1-x}S₂ Nanosheets with High-Concentration Metallic 1T Phase, *Small*, 2016, **12**, 1866–1874.

149 O. Eksik, J. Gao, S. A. Shojaee, A. Thomas, P. Chow, S. F. Bartolucci, D. A. Lucca and N. Koratkar, Epoxy nanocomposites with two-dimensional transition metal dichalcogenide additives, *ACS Nano*, 2014, **8**, 5282–5289.

150 C. Tan and H. Zhang, Two-dimensional transition metal dichalcogenide nanosheet-based composites, *Chem. Soc. Rev.*, 2015, **44**, 2713–2731.

151 J. Y. Lin, C. Y. Chan and S. W. Chou, Electrophoretic deposition of transparent MoS₂-graphene nanosheet composite films as counter electrodes in dye-sensitized solar cells, *Chem. Commun.*, 2013, **49**, 1440–1442.

152 G. Yue, J. Y. Lin, S. Y. Tai, Y. Xiao and J. Wu, A catalytic composite film of MoS₂/graphene flake as a counter electrode for Pt-free dye-sensitized solar cells, *Electrochim. Acta*, 2012, **85**, 162–168.

153 C. Yu, X. Meng, X. Song, S. Liang, Q. Dong, G. Wang, C. Hao, X. Yang, T. Ma, P. M. Ajayan and J. Qiu, Graphene-mediated highly-dispersed MoS₂ nanosheets with enhanced triiodide reduction activity for dye-sensitized solar cells, *Carbon*, 2016, **100**, 474–483.

154 P. Lynch, U. Khan, A. Harvey, I. Ahmed and J. N. Coleman, Graphene–MoS₂ nanosheet composites as electrodes for dye sensitised solar cells, *Mater. Res. Express*, 2016, **3**, 035007.

155 S. Li, H. Min, F. Xu, L. Tong, J. Chen, C. Zhu and L. Sun, All electrochemical fabrication of MoS₂/graphene counter electrodes for efficient dye-sensitized solar cells, *RSC Adv.*, 2016, **6**, 34546–34552.

156 C. K. Cheng, C. H. Lin, H. C. Wu, C. C. M. Ma, T. K. Yeh, H. Y. Chou, C. H. Tsai and C. K. Hsieh, The Two-Dimensional Nanocomposite of Molybdenum Disulfide and Nitrogen-Doped Graphene Oxide for Efficient Counter Electrode of Dye-Sensitized Solar Cells, *Nanoscale Res. Lett.*, 2016, **11**, 1–9.

157 M. S. Fan, C. P. Lee, C. T. Li, Y. J. Huang, R. Vittal and K. C. Ho, Nitrogen-doped graphene/molybdenum disulfide composite as the electrocatalytic film for dye-sensitized solar cells, *Electrochim. Acta*, 2016, **211**, 164–172.

158 J. Y. Lin, G. Yue, S. Y. Tai, Y. Xiao, H. M. Cheng, F. M. Wang and J. Wu, Hydrothermal synthesis of graphene flake embedded nanosheet-like molybdenum sulfide hybrids as counter electrode catalysts for dye-sensitized solar cells, *Mater. Chem. Phys.*, 2013, **143**, 53–59.

159 G. Yue, X. Ma, Q. Jiang, F. Tan, J. Wu, C. Chen, F. Li and Q. Li, PEDOT:PSS and glucose assisted preparation of molybdenum disulfide/single-wall carbon nanotubes counter electrode and served in dye-sensitized solar cells, *Electrochim. Acta*, 2014, **142**, 68–75.

160 S. Y. Tai, C. J. Liu, S. W. Chou, F. S. S. Chien, J. Y. Lin and T. W. Lin, Few-layer MoS₂ nanosheets coated onto multi-walled carbon nanotubes as a low-cost and highly electrocatalytic counter electrode for dye-sensitized solar cells, *J. Mater. Chem.*, 2012, **22**, 24753–24759.

161 C. H. Lin, C. H. Tsai, F. G. Tseng, C. C. M. Ma, H. C. Wu and C. K. Hsieh, Three-dimensional vertically aligned hybrid nanoarchitecture of two-dimensional molybdenum disulfide nanosheets anchored on directly grown one-dimensional carbon nanotubes for use as a counter electrode in dye-sensitized solar cells, *J. Alloys Compd.*, 2017, **692**, 941–949.

162 M. Zheng, J. Huo, Y. Tu, J. Wu, L. Hu and S. Dai, Flowerlike molybdenum sulfide/multi-walled carbon nanotube hybrid as Pt-free counter electrode used in dye-sensitized solar cells, *Electrochim. Acta*, 2015, **173**, 252–259.

163 W. Liu, S. He, Y. Wang, Y. Dou, D. Pan, Y. Feng, G. Qian, J. Xu and S. Miao, PEG-assisted synthesis of homogeneous carbon nanotubes–MoS₂–carbon as a counter electrode for dye-sensitized solar cells, *Electrochim. Acta*, 2014, **144**, 119–126.

164 G. Yue, W. Zhang, J. Wu and Q. Jiang, Glucose aided synthesis of molybdenum sulfide/carbon nanotubes composites as counter electrode for high performance dye-sensitized solar cells, *Electrochim. Acta*, 2013, **112**, 655–662.

165 J. Y. Lin, A. L. Su, C. Y. Chang, K. C. Hung and T. W. Lin, Molybdenum Disulfide/Reduced Graphene Oxide–Carbon Nanotube Hybrids as Efficient Catalytic Materials in Dye-Sensitized Solar Cells, *ChemElectroChem*, 2015, **2**, 720–725.

166 (a) S. Wang, X. Jiang, H. Zheng, H. Wu, S. J. Kim and C. Feng, Solvothermal synthesis of MoS₂/carbon nanotube composites with improved electrochemical performance for lithium ion batteries, *Nanosci. Nanotechnol. Lett.*, 2012, **4**, 378–383; (b) J. Z. Wang, L. Lu, M. Lotya, J. N. Coleman, S. L. Chou, H. K. Liu, A. I. Minett and J. Chen, Development of MoS₂–CNT composite thin film from layered MoS₂ for lithium batteries, *Adv. Energy Mater.*, 2013, **3**, 798–805.

167 T. Du, N. Wang, H. Chen, H. He, H. Lin and K. Liu, TiO₂-based solar cells sensitized by chemical-bath-deposited few-layer MoS₂, *J. Power Sources*, 2015, **275**, 943–949.

168 W. H. Jhang and Y. J. Lin, Interface modification of MoS₂ counter electrode/electrolyte in dye-sensitized solar cells by incorporating TiO₂ nanoparticles, *Curr. Appl. Phys.*, 2015, **15**, 906–909.

169 H. C. Hung, Y. J. Lin and Z. Y. Ke, Interface modification of MoS₂:TiO₂ counter electrode/electrolyte in dye-sensitized solar cells by doping with different Co contents, *J. Mater. Sci.: Mater. Electron.*, 2016, **27**, 5059–5063.



170 Z. He, W. Que, Y. Xing and X. Liu, Reporting performance in MoS_2 – TiO_2 bilayer and heterojunction films based dye-sensitized photovoltaic devices, *J. Alloys Compd.*, 2016, **672**, 481–488.

171 G. Yue, J. Wu, Y. Xiao, M. Huang, J. Lin and J. Y. Lin, High performance platinum-free counter electrode of molybdenum sulfide–carbon used in dye-sensitized solar cells, *J. Mater. Chem. A*, 2013, **1**, 1495–1501.

172 W. B. Li, M. X. Sun, J. He, S. F. Sun, Q. Zhang and Y. Y. Shi, Preparation of MoS_2 /Carbon Fiber Counter Electrodes and Its Application in DSSCs, *J. Mater. Sci. Eng.*, 2015, **3**, 020.

173 J. Theerthagiri, R. A. Senthil, P. Arunachalam, J. Madhavan, M. H. Buraidah, A. Santhanam and A. K. Arof, Synthesis of various carbon incorporated flower-like MoS_2 microspheres as counter electrode for dye-sensitized solar cells, *J. Solid State Electrochem.*, 2016, 1–10.

174 D. Song, M. Li, Y. Jiang, Z. Chen, F. Bai, Y. Li and B. Jiang, Facile fabrication of MoS_2 /PEDOT–PSS composites as low-cost and efficient counter electrodes for dye-sensitized solar cells, *J. Photochem. Photobiol. A*, 2014, **279**, 47–51.

175 X. Liang, H. W. Zheng, X. J. Li, Y. H. Yu, G. T. Yue, W. Zhang, J. J. Tian and T. F. Li, Nanocomposites of $\text{Bi}_5\text{FeTi}_3\text{O}_{15}$ with MoS_2 as Novel Pt-free Counter Electrode in Dye-Sensitized Solar Cells, *Ceram. Int.*, 2016, **42**, 12888–12893.

176 J. G. Song, J. Park, W. Lee, T. Choi, H. Jung, C. W. Lee, S. H. Hwang, J. M. Myoung, J. H. Jung, S. H. Kim and C. Lansalot-Matras, Layer-controlled, wafer-scale, and conformal synthesis of tungsten disulfide nanosheets using atomic layer deposition, *ACS Nano*, 2013, **7**, 11333–11340.

177 A. L. Elias, N. Perea-López, A. Castro-Beltrán, A. Berkdemir, R. Lv, S. Feng, A. D. Long, T. Hayashi, Y. A. Kim, M. Endo and H. R. Gutiérrez, Controlled synthesis and transfer of large-area WS_2 sheets: from single layer to few layers, *ACS Nano*, 2013, **7**, 5235–5242.

178 S. I. Nikitenko, Y. Koltypin, Y. Mastai, M. Koltypin and A. Gedanken, Sonochemical synthesis of tungsten sulfide nanorods, *J. Mater. Chem.*, 2002, **12**, 1450–1452.

179 Y. Q. Zhu, W. K. Hsu, H. Terrones, N. Grobert, B. H. Chang, M. Terrones, B. Q. Wei, H. W. Kroto, D. R. M. Walton, C. B. Boothroyd and I. Kinloch, Morphology, structure and growth of WS_2 nanotubes, *J. Mater. Chem.*, 2000, **10**, 2570–2577.

180 R. Rosentsveig, A. Margolin, Y. Feldman, R. Popovitz-Biro and R. Tenne, WS_2 nanotube bundles and foils, *Chem. Mater.*, 2002, **14**, 471–473.

181 Y. Wang, S. Li, Y. Bai, Z. Chen, Q. Jiang, T. Li and W. Zhang, Dye-sensitized solar cells based on low cost carbon-coated tungsten disulphide counter electrodes, *Electrochim. Acta*, 2013, **114**, 30–34.

182 S. Hussain, S. F. Shaikh, D. Vikraman, R. S. Mane, O. S. Joo, M. Naushad and J. Jung, Sputtering and sulfurization-combined synthesis of a transparent WS_2 counter electrode and its application to dye-sensitized solar cells, *RSC Adv.*, 2015, **5**, 103567–103572.

183 S. H. Ahn and A. Manthiram, Edge-Oriented Tungsten Disulfide Catalyst Produced from Mesoporous WO_3 for Highly Efficient Dye-Sensitized Solar Cells, *Adv. Energy Mater.*, 2016, **6**, 1501814, DOI: 10.1002/aenm.201501814.

184 S. Li, Z. Chen and W. Zhang, Dye-sensitized solar cells based on WS_2 counter electrodes, *Mater. Lett.*, 2012, **72**, 22–24.

185 G. Yue, J. Wu, J. Y. Lin, Y. Xiao, S. Y. Tai, J. Lin, M. Huang and Z. Lan, A counter electrode of multi-wall carbon nanotubes decorated with tungsten sulfide used in dye-sensitized solar cells, *Carbon*, 2013, **55**, 1–9.

186 J. Wu, G. Yue, Y. Xiao, M. Huang, J. Lin, L. Fan, Z. Lan and J. Y. Lin, Glucose aided preparation of tungsten sulfide/multi-wall carbon nanotube hybrid and use as counter electrode in dye-sensitized solar cells, *ACS Appl. Mater. Interfaces*, 2012, **4**, 6530–6536.

187 J. A. Wilson, Concerning the semimetallic characters of TiS_2 and TiSe_2 , *Solid State Commun.*, 1977, **22**, 551–553.

188 G. A. Benesh, A. M. Woolley and C. Umrigar, The pressure dependences of TiS_2 and TiSe_2 band structures, *J. Phys. C: Solid State Phys.*, 1985, **18**(8), 1595.

189 C. Bourgès, T. Barbier, G. Guélou, P. Vaqueiro, A. V. Powell, O. I. Lebedev, N. Barrier, Y. Kinemuchi and E. Guilmeau, Thermoelectric properties of TiS_2 mechanically alloyed compounds, *J. Eur. Ceram. Soc.*, 2016, **36**, 1183–1189.

190 M. Inoue, H. P. Hughes and A. D. Yoffe, The electronic and magnetic properties of the 3d transition metal intercalates of TiS_2 , *Adv. Phys.*, 1989, **38**, 565–604.

191 C. Wan, X. Gu, F. Dang, T. Itoh, Y. Wang, H. Sasaki, M. Kondo, K. Koga, K. Yabuki, G. J. Snyder and R. Yang, Flexible n-type thermoelectric materials by organic intercalation of layered transition metal dichalcogenide TiS_2 , *Nat. Mater.*, 2015, **14**, 622–627.

192 C. S. Cucinotta, K. Dolui, H. Pettersson, Q. M. Ramasse, E. Long, S. E. O'Brian, V. Nicolosi and S. Sanvito, Electronic Properties and Chemical Reactivity of TiS_2 Nanoflakes, *J. Phys. Chem. C*, 2015, **119**, 15707–15715.

193 J. Chen, S. L. Li, Z. L. Tao, Y. T. Shen and C. X. Cui, Titanium disulfide nanotubes as hydrogen-storage materials, *J. Am. Chem. Soc.*, 2003, **125**, 5284–5285.

194 S. Prabakar, C. W. Bumby and R. D. Tilley, Liquid-phase synthesis of flower-like and flake-like titanium disulfide nanostructures, *Chem. Mater.*, 2009, **21**, 1725–1730.

195 A. Margolin, R. Popovitz-Biro, A. Albu-Yaron, A. Moshkovich, L. Rapoport and R. Tenne, Fullerene-like nanoparticles of titanium disulfide, *Curr. Nanosci.*, 2005, **1**, 253–262.

196 K. H. Park, J. Choi, H. J. Kim, D. H. Oh, J. R. Ahn and S. U. Son, Unstable Single-Layered Colloidal TiS_2 Nanodisks, *Small*, 2008, **4**, 945–950.

197 X. Sun, P. Bonnick and L. F. Nazar, Layered TiS_2 Positive Electrode for Mg Batteries, *ACS Energy Lett.*, 2016, **1**, 297–301.

198 C. Lin, X. Zhu, J. Feng, C. Wu, S. Hu, J. Peng, Y. Guo, L. Peng, J. Zhao, J. Huang and J. Yang, Hydrogen-incorporated TiS_2 ultrathin nanosheets with ultrahigh



conductivity for stamp-transferrable electrodes, *J. Am. Chem. Soc.*, 2013, **135**, 5144–5151.

199 X. Meng, C. Yu, B. Lu, J. Yang and J. Qiu, Dual integration system endowing two-dimensional titanium disulfide with enhanced triiodide reduction performance in dye-sensitized solar cells, *Nano Energy*, 2016, **22**, 59–69.

200 C. T. Li, C. P. Lee, Y. Y. Li, M. H. Yeh and K. C. Ho, A composite film of TiS_2 /PEDOT:PSS as the electrocatalyst for the counter electrode in dye-sensitized solar cells, *J. Mater. Chem. A*, 2013, **1**, 14888–14896.

201 S. L. Yang, H. B. Yao, M. R. Gao and S. H. Yu, Monodisperse cubic pyrite NiS_2 dodecahedrons and microspheres synthesized by a solvothermal process in a mixed solvent: thermal stability and magnetic properties, *CrystEngComm*, 2009, **11**, 1383–1390.

202 X. Song, W. Shen, Z. Sun, C. Yang, P. Zhang and L. Gao, Size-engineerable NiS_2 hollow spheres photo co-catalysts from supermolecular precursor for H_2 production from water splitting, *Chem. Eng. J.*, 2016, **290**, 74–81.

203 C. Tang, Z. Pu, Q. Liu, A. M. Asiri and X. Sun, NiS_2 nanosheets array grown on carbon cloth as an efficient 3D hydrogen evolution cathode, *Electrochim. Acta*, 2015, **153**, 508–514.

204 F. Gautier, G. Krill, M. F. Lapierre and C. Robert, Influence of non-stoichiometry on the electrical and magnetic properties of NiS_2 , *Solid State Commun.*, 1972, **11**, 1201–1203.

205 A. Jamil, S. S. Batool, F. Sher and M. A. Rafiq, Determination of density of states, conduction mechanisms and dielectric properties of nickel disulfide nanoparticles, *AIP Adv.*, 2016, **6**, 055120.

206 Z. Wan, C. Jia and Y. Wang, *In situ* growth of hierarchical NiS_2 hollow microspheres as efficient counter electrode for dye-sensitized solar cell, *Nanoscale*, 2015, **7**, 12737–12742.

207 X. Zuo, S. Yan, B. Yang, G. Li, M. Wu, Y. Ma, S. Jin and K. Zhu, Hollow spherical NiS/NiS_2 , *J. Mater. Sci.: Mater. Electron.*, 2016, **27**, 7974.

208 X. Zuo, S. Yan, B. Yang, G. Li, H. Zhang, H. Tang, M. Wu, Y. Ma, S. Jin and K. Zhu, Template-free synthesis of nickel sulfides hollow spheres and their application in dye-sensitized solar cells, *Sol. Energy*, 2016, **132**, 503–510.

209 J. Zheng, W. Zhou, Y. Ma, W. Cao, C. Wang and L. Guo, Facet-dependent NiS_2 polyhedrons on counter electrodes for dye-sensitized solar cells, *Chem. Commun.*, 2015, **51**, 12863–12866.

210 Z. Li, F. Gong, G. Zhou and Z. S. Wang, NiS_2 /reduced graphene oxide nanocomposites for efficient dye-sensitized solar cells, *J. Phys. Chem. C*, 2013, **117**, 6561–6566.

211 L. Zhu, B. J. Richardson and Q. Yu, Anisotropic growth of iron pyrite FeS_2 nanocrystals *via* oriented attachment, *Chem. Mater.*, 2015, **27**, 3516–3525.

212 J. Puthusseri, S. Seefeld, N. Berry, M. Gibbs and M. Law, Colloidal iron pyrite (FeS_2) nanocrystal inks for thin-film photovoltaics, *J. Am. Chem. Soc.*, 2010, **133**, 716–719.

213 Y. Bi, Y. Yuan, C. L. Exstrom, S. A. Darveau and J. Huang, Air stable, photosensitive, phase pure iron pyrite nanocrystal thin films for photovoltaic application, *Nano Lett.*, 2011, **11**, 4953–4957.

214 M. Cabaán-Acevedo, M. S. Faber, Y. Tan, R. J. Hamers and S. Jin, Synthesis and properties of semiconducting iron pyrite (FeS_2) nanowires, *Nano Lett.*, 2012, **12**, 1977–1982.

215 S. Shukla, G. Xing, H. Ge, R. R. Prabhakar, S. Mathew, Z. Su, V. Nalla, T. Venkatesan, N. Mathews, T. Sritharan and T. C. Sum, Origin of photocarrier losses in iron pyrite (FeS_2) nanocubes, *ACS Nano*, 2016, **10**, 4431–4440.

216 M. Barawi, I. J. Ferrer, E. Flores, S. Yoda, J. R. Ares and C. Sánchez, Hydrogen photoassisted generation by visible light and an earth abundant photocatalyst: pyrite (FeS_2), *J. Phys. Chem. C*, 2016, **120**, 9547–9552.

217 I. G. Orletskii, P. D. Mar'yanchuk, E. V. Mastruk, M. N. Solovan and V. V. Brus, Low-temperature spray-pyrolysis of FeS_2 films and their electrical and optical properties, *Phys. Solid State*, 2016, **58**, 37–41.

218 F. Jiang, L. T. Peckler and A. J. Muscat, Phase pure pyrite FeS_2 nanocubes synthesized using oleylamine as ligand, solvent, and reductant, *Cryst. Growth Des.*, 2015, **15**, 3565–3572.

219 X. Zhang, T. Scott, T. Socha, D. Nielsen, M. Manno, M. Johnson, Y. Yan, Y. Losovyj, P. Dowben, E. S. Aydin and C. Leighton, Phase stability and stoichiometry in thin film iron pyrite: impact on electronic transport properties, *ACS Appl. Mater. Interfaces*, 2015, **7**, 14130–14139.

220 L. Xu, Y. Hu, H. Zhang, H. Jiang and C. Li, Confined synthesis of FeS_2 nanoparticles encapsulated in carbon nanotube hybrids for ultrastable lithium-ion batteries, *ACS Sustainable Chem. Eng.*, 2016, **4**, 4251–4255.

221 S. Shukla, N. H. Loc, P. P. Boix, T. M. Koh, R. R. Prabhakar, H. K. Mulmudi, J. Zhang, S. Chen, C. F. Ng, C. H. A. Huan and N. Mathews, Iron pyrite thin film counter electrodes for dye-sensitized solar cells: high efficiency for iodine and cobalt redox electrolyte cells, *ACS Nano*, 2014, **8**, 10597–10605.

222 Q. H. Huang, T. Ling, S. Z. Qiao and X. W. Du, Pyrite nanorod arrays as an efficient counter electrode for dye-sensitized solar cells, *J. Mater. Chem. A*, 2013, **1**, 11828–11833.

223 C. Song, S. Wang, W. Dong, X. Fang, J. Shao, J. Zhu and X. Pan, Hydrothermal synthesis of iron pyrite (FeS_2) as efficient counter electrodes for dye-sensitized solar cells, *Sol. Energy*, 2016, **133**, 429–436.

224 Y. C. Wang, D. Y. Wang, Y. T. Jiang, H. A. Chen, C. C. Chen, K. C. Ho, H. L. Chou and C. W. Chen, FeS_2 Nanocrystal Ink as a Catalytic Electrode for Dye-Sensitized Solar Cells, *Angew. Chem., Int. Ed.*, 2013, **52**, 6694–6698.

225 B. Kilic, S. Turkdogan, A. Astam, O. C. Ozer, M. Asgin, H. Cebeci, D. Urk and S. P. Mucur, Preparation of Carbon Nanotube/ TiO_2 Mesoporous Hybrid Photoanode with Iron Pyrite (FeS_2) Thin Films Counter Electrodes for Dye-Sensitized Solar Cell., *Sci. Rep.*, 2016, **6**, 27052.



226 S. Miyahara and T. Teranishi, Magnetic properties of FeS_2 and CoS_2 , *J. Appl. Phys.*, 1968, **39**, 896–897.

227 N. Wu, Y. B. Losovyj, D. Wisbey, K. Belashchenko, M. Manno, L. Wang, C. Leighton and P. A. Dowben, The electronic band structure of CoS_2 , *J. Phys.: Condens. Matter*, 2007, **19**, 156224.

228 W. Fang, D. Liu, Q. Lu, X. Sun and A. M. Asiri, Nickel promoted cobalt disulfide nanowire array supported on carbon cloth: an efficient and stable bifunctional electrocatalyst for full water splitting, *Electrochim. Commun.*, 2016, **63**, 60–64.

229 Q. Wang, L. Jiao, Y. Han, H. Du, W. Peng, Q. Huan, D. Song, Y. Si, Y. Wang and H. Yuan, CoS_2 hollow spheres: fabrication and their application in lithium-ion batteries, *J. Phys. Chem. C*, 2011, **115**, 8300–8304.

230 L. Yu, J. F. Yang and X. W. D. Lou, Formation of CoS_2 nanobubble hollow prisms for highly reversible lithium storage, *Angew. Chem., Int. Ed.*, 2016, **55**, 13422–13426.

231 D. Zhang, H. Liu, J. Zhang, X. Wang, R. Zhang, J. Zhou, J. Zhong and B. Yuan, Synthesis of novel CoS_2 nanodendrites with high performance supercapacitors, *Int. J. Electrochem. Sci.*, 2016, **11**, 6791–6798.

232 J. Jin, X. Zhang and T. He, Self-assembled CoS_2 nanocrystal film as an efficient counter electrode for dye-sensitized solar cells, *J. Phys. Chem. C*, 2014, **118**, 24877–24883.

233 J. C. Tsai, M. H. Hon and I. C. Leu, Fabrication of mesoporous CoS_2 nanotube arrays as the counter electrodes of dye-sensitized solar cells, *Chem.-Asian J.*, 2015, **10**, 1932–1939.

234 J. C. Tsai, M. H. Hon and C. Leu, Preparation of CoS_2 nanoflake arrays through ion exchange reaction of Co(OH)_2 and their application as counter electrodes for dye-sensitized solar cells, *RSC Adv.*, 2015, **5**, 4328–4333.

235 M. Congiu, L. G. S. Albano, F. Decker and C. F. O. Graeff, Single precursor route to efficient cobalt sulphide counter electrodes for dye sensitized solar cells, *Electrochim. Acta*, 2015, **151**, 517–524.

236 S. S. Rao, C. V. Gopi, S. K. Kim, M. K. Son, M. S. Jeong, A. D. Savariraj, K. Prabakar and H. J. Kim, Cobalt sulfide thin film as an efficient counter electrode for dye-sensitized solar cells, *Electrochim. Acta*, 2014, **133**, 174–179.

237 X. Cui, Z. Xie and Y. Wang, Novel CoS_2 embedded carbon nanocages by direct sulfurizing metal-organic frameworks for dye-sensitized solar cells, *Nanoscale*, 2016, **8**, 11984–11992.

238 H. J. Kim, C. W. Kim, D. Punnoose, C. V. Gopi, S. K. Kim, K. Prabakar and S. S. Rao, Nickel doped cobalt sulfide as a high performance counter electrode for dye-sensitized solar cells, *Appl. Surf. Sci.*, 2015, **328**, 78–85.

239 X. Duan, Z. Gao, J. Chang, D. Wu, P. Ma, J. He, F. Xu, S. Gao and K. Jiang, CoS_2 -graphene composite as efficient catalytic counter electrode for dye-sensitized solar cell, *Electrochim. Acta*, 2013, **114**, 173–179.

240 L. Sun, Y. Bai, N. Zhang and K. Sun, The facile preparation of a cobalt disulfide-reduced graphene oxide composite film as an efficient counter electrode for dye-sensitized solar cells, *Chem. Commun.*, 2015, **51**, 1846–1849.

241 B. Hai, K. Tang, C. Wang, C. An, Q. Yang, G. Shen and Y. Qian, Synthesis of SnS_2 nanocrystals via a solvothermal process, *J. Cryst. Growth*, 2001, **225**, 92–95.

242 C. Zhai, N. Du and H. Z. D. Yang, Large-scale synthesis of ultrathin hexagonal tin disulfide nanosheets with highly reversible lithium storage, *Chem. Commun.*, 2011, **47**, 1270–1272.

243 Y. T. Lin, J. B. Shi, Y. C. Chen, C. J. Chen and P. F. Wu, Synthesis and characterization of tin disulfide (SnS_2) nanowires, *Nanoscale Res. Lett.*, 2009, **4**, 694.

244 J. Wang, J. Liu, H. Xu, S. Ji, J. Wang, Y. Zhou, P. Hodgson and Y. Li, Gram-scale and template-free synthesis of ultralong tin disulfide nanobelts and their lithium ion storage performances, *J. Mater. Chem. A*, 2013, **1**, 1117–1122.

245 Y. Huang, H. Zang, J. S. Chen, E. A. Sutter, P. W. Sutter, C. Y. Nam and M. Cotlet, Hybrid quantum dot-tin disulfide field-effect transistors with improved photocurrent and spectral responsivity, *Appl. Phys. Lett.*, 2016, **108**, 123502.

246 A. Giberti, A. Gaiardo, B. Fabbri, S. Gherardi, V. Guidi, C. Malagù, P. Bellutti, G. Zonta, D. Casotti and G. Cruciani, Tin(iv) sulfide nanorods as a new gas sensing material, *Sens. Actuators, B*, 2016, **223**, 827–833.

247 W. Du, D. Deng, Z. Han, W. Xiao, C. Bian and X. Qian, Hexagonal tin disulfide nanoplatelets: a new photocatalyst driven by solar light, *CrystEngComm*, 2011, **13**, 2071–2076.

248 N. T. N. Truong and C. Park, Synthesis and characterization of tin disulfide nanocrystals for hybrid bulk hetero-junction solar cell applications, *Electron. Mater. Lett.*, 2016, **12**, 308–314.

249 Y. Bai, X. Zong, H. Yu, Z. G. Chen and L. Wang, Scalable low-cost SnS_2 nanosheets as counter electrode building blocks for dye-sensitized solar cells, *Chem.-Eur. J.*, 2014, **20**, 8670–8676.

250 B. Yang, X. Zuo, P. Chen, L. Zhou, X. Yang, H. Zhang, G. Li, M. Wu, Y. Ma, S. Jin and X. Chen, Nanocomposite of tin sulfide nanoparticles with reduced graphene oxide in high-efficiency dye-sensitized solar cells, *ACS Appl. Mater. Interfaces*, 2015, **7**, 137–143.

251 S. Sugai and T. Ueda, High-pressure Raman spectroscopy in the layered materials $2\text{H}-\text{MoS}_2$, 2HMoTe_2 , and $2\text{H}-\text{MoTe}_2$, *Phys. Rev. B: Condens. Matter Mater. Phys.*, 1982, **26**, 6554.

252 T. Böker, R. Severin, A. Müller, C. Janowitz, R. Manzke, D. Voß, P. Krüger, A. Mazur and J. Pollmann, Band structure of MoS_2 , MoSe_2 , and $\alpha\text{-MoTe}_2$: angle-resolved photoelectron spectroscopy and *ab initio* calculations, *Phys. Rev. B: Condens. Matter Mater. Phys.*, 2001, **64**, 235305.

253 N. L. Heda, A. Dashora, A. Marwal, Y. Sharma, S. K. Srivastava, G. Ahmed, R. Jain and B. L. Ahuja, Electronic properties and Compton profiles of molybdenum dichalcogenides, *J. Phys. Chem. Solids*, 2010, **71**, 187–193.

254 S. H. Rhim, Y. S. Kim and A. J. Freeman, Strain-induced giant second-harmonic generation in monolayered $2\text{H}-\text{MoX}_2$ ($\text{X} = \text{S}, \text{Se}, \text{Te}$), *Appl. Phys. Lett.*, 2015, **107**, 241908.



255 S. Caramazza, C. Marini, L. Simonelli, P. Dore and P. Postorino, Temperature dependent EXAFS study on transition metal dichalcogenides MoX_2 (X = S, Se, Te), *J. Phys.: Condens. Matter*, 2016, **28**, 325401.

256 H. Jiang, Electronic band structures of molybdenum and tungsten dichalcogenides by the GW approach, *J. Phys. Chem. C*, 2012, **116**, 7664–7671.

257 U. Ahuja, R. Joshi, D. C. Kothari, H. Tiwari and K. Venugopalan, Optical response of mixed molybdenum dichalcogenides for solar cell applications using the modified becke-johnson potential, *Z. Naturforsch., A: Phys. Sci.*, 2016, **71**, 213–223.

258 A. Abderrahmane, P. J. Ko, T. V. Thu, S. Ishizawa, T. Takamura and A. Sandhu, High photosensitivity few-layered MoSe_2 back-gated field-effect phototransistors, *Nanotechnology*, 2014, **25**, 365202.

259 H. J. Chuang, B. Chamlagain, M. Koehler, M. M. Perera, J. Yan, D. Mandrus, D. Tomaánek and Z. Zhou, Low-resistance 2D/2D ohmic contacts: a universal approach to high-performance WSe_2 , MoS_2 , and MoSe_2 transistors, *Nano Lett.*, 2016, **16**, 1896–1902.

260 L. T. L. Lee, J. He, B. Wang, Y. Ma, K. Y. Wong, Q. Li, X. Xiao and T. Chen, Few-layer MoSe_2 possessing high catalytic activity towards iodide/tri-iodide redox shuttles, *Sci. Rep.*, 2014, **4**, 4063–4069.

261 H. Chen, Y. Xie, H. Cui, W. Zhao, X. Zhu, Y. Wang, X. Lü and F. Huang, *In situ* growth of a MoSe_2/Mo counter electrode for high efficiency dye-sensitized solar cells, *Chem. Commun.*, 2014, **50**, 4475–4477.

262 I. A. Ji, H. M. Choi and J. H. Bang, Metal selenide films as the counter electrode in dye-sensitized solar cell, *Mater. Lett.*, 2014, **123**, 51–54.

263 J. Jia, J. Wu, J. Dong, Y. Tu, Z. Lan, L. Fan and Y. Wei, High-performance molybdenum diselenide electrodes used in dye-sensitized solar cells and supercapacitors, *IEEE J. Photovoltaics*, 2016, **6**, 1196–1202.

264 E. Bi, H. Chen, X. Yang, F. Ye, M. Yin and L. Han, Fullerene-structured MoSe_2 hollow spheres anchored on highly nitrogen-doped graphene as a conductive catalyst for photovoltaic applications, *Sci. Rep.*, 2015, **5**, 13214.

265 Y. J. Huang, M. S. Fan, C. T. Li, C. P. Lee, T. Y. Chen, R. Vittal and K. C. Ho, MoSe_2 nanosheet/poly(3,4-ethylenedioxythiophene):poly(styrenesulfonate) composite film as a Pt-free counter electrode for dye-sensitized solar cells, *Electrochim. Acta*, 2016, **211**, 794–803.

266 J. Dong, J. Wu, J. Jia, L. Hu and S. Dai, Cobalt/molybdenum ternary hybrid with hierarchical architecture used as high efficient counter electrode for dye-sensitized solar cells, *Sol. Energy*, 2015, **122**, 326–333.

267 Q. Jiang and G. Hu, $\text{Co}_{0.85}\text{Se}$ hollow nanoparticles as Pt-free counter electrode materials for dye-sensitized solar cells, *Mater. Lett.*, 2015, **153**, 114–117.

268 Y. Duan, Q. Tang, J. Liu, B. He and L. Yu, Transparent metal selenide alloy counter electrodes for high-efficiency bifacial dye-sensitized solar cells, *Angew. Chem., Int. Ed.*, 2014, **53**, 14569–14574.

269 A. Banerjee, K. K. Upadhyay, S. Bhatnagar, M. Tathavadekar, U. Bansode, S. Agarkar and S. B. Ogale, Nickel cobalt sulfide nanoneedle array as an effective alternative to Pt as a counter electrode in dye sensitized solar cells, *RSC Adv.*, 2014, **4**, 8289–8294.

270 D. Jerome, A. J. Grant and A. D. Yoffe, Pressure enhanced superconductivity in NbSe_2 , *Solid State Commun.*, 1971, **9**, 2183–2185.

271 D. H. Galvan, J. H. Kim, M. B. Maple, M. Avalos-Borja and E. Adem, Formation of NbSe_2 nanotubes by electron irradiation, *Fullerene Sci. Technol.*, 2000, **8**, 143–151.

272 N. E. Staley, J. Wu, P. Eklund, Y. Liu, L. Li and Z. Xu, Electric field effect on superconductivity in atomically thin flakes of NbSe_2 , *Phys. Rev. B: Condens. Matter Mater. Phys.*, 2009, **80**, 184505.

273 V. V. Ivanovskaya, A. N. Enyashin, N. I. Medvedeva and A. L. Ivanovskii, Electronic properties of superconducting NbSe_2 nanotubes, *Phys. Status Solidi B*, 2003, **238**, R1–R4.

274 T. Tsuneta, T. Toshima, K. Inagaki, T. Shibayama, S. Tanda, S. Uji, M. Ahlskog, P. Hakonen and M. Paalanen, Formation of metallic NbSe_2 nanotubes and nanofibers, *Curr. Appl. Phys.*, 2003, **3**, 473–476.

275 E. Hitz, J. Wan, A. Patel, Y. Xu, L. Meshi, J. Dai, Y. Chen, A. Lu, A. V. Davydov and L. Hu, Electrochemical intercalation of lithium ions into NbSe_2 nanosheets, *ACS Appl. Mater. Interfaces*, 2016, **8**, 11390–11395.

276 K. J. Reynolds, G. L. Frey and R. H. Friend, Solution-processed niobium diselenide as conductor and anode for polymer light-emitting diodes, *Appl. Phys. Lett.*, 2003, **82**, 1123–1125.

277 (a) M. Yoshida, J. Ye, T. Nishizaki, N. Kobayashi and Y. Iwasa, Electrostatic and electrochemical tuning of superconductivity in two-dimensional NbSe_2 crystals, *Appl. Phys. Lett.*, 2016, **108**, 202602; (b) X. Zhu, Y. Guo, H. Cheng, J. Dai, X. An, J. Zhao, K. Tian, S. Wei, X. C. Zeng, C. Wu and Y. Xie, Signature of coexistence of superconductivity and ferromagnetism in two-dimensional NbSe_2 triggered by surface molecular adsorption, *Nat. Commun.*, 2016, **7**, 11210.

278 D. W. Murphy, F. A. Trumbore and J. N. Carides, A new niobium selenide cathode for nonaqueous lithium batteries, *J. Electrochem. Soc.*, 1977, **124**, 325–329.

279 J. Guo, Y. Shi, C. Zhu, L. Wang, N. Wang and T. Ma, Cost-effective and morphology-controllable niobium diselenides for highly efficient counter electrodes of dye-sensitized solar cells, *J. Mater. Chem. A*, 2013, **1**, 11874–11879.

280 M. A. Ibrahim, W. C. Huang, T. W. Lan, K. M. Boopathi, Y. C. Hsiao, C. H. Chen, W. Budiawan, Y. Y. Chen, C. S. Chang, L. J. Li, C. H. Tsai and C. C. Chu, Controlled mechanical cleavage of bulk niobium diselenide to nanoscaled sheet, rod, and particle structures for Pt-free dye-sensitized solar cells, *J. Mater. Chem. A*, 2014, **2**, 11382–11390.

281 J. Guo, S. Liang, Y. Shi, C. Hao, X. Wang and T. Ma, Transition metal selenides as efficient counter-electrode



materials for dye-sensitized solar cells, *Phys. Chem. Chem. Phys.*, 2015, **17**, 28985–28992.

282 F. Gong, X. Xu, Z. Li, G. Zhou and Z. S. Wang, NiSe₂ as an efficient electrocatalyst for a Pt-free counter electrode of dye-sensitized solar cells, *Chem. Commun.*, 2013, **49**, 1437–1439.

283 X. Zhang, T. Z. Jing, S. Q. Guo, G. D. Gao and L. Liu, Synthesis of NiSe₂/reduced graphene oxide crystalline materials and their efficient electrocatalytic activity in dye-sensitized solar cells, *RSC Adv.*, 2014, **4**, 50312–50317.

284 J. Xiao, L. Wan, S. Yang, F. Xiao and S. Wang, Design hierarchical electrodes with highly conductive NiCo₂S₄ nanotube arrays grown on carbon fiber paper for high-performance pseudocapacitors, *Nano Lett.*, 2014, **14**, 831–838.

285 Q. Wang, B. Liu, X. Wang, S. Ran, L. Wang, D. Chen and G. Shen, Morphology evolution of urchin-like NiCo₂O₄ nanostructures and their applications as pseudocapacitors and photoelectrochemical cells, *J. Mater. Chem.*, 2012, **22**, 21647–21653.

286 J. Huo, J. Wu, M. Zheng, Y. Tu and Z. Lan, Flower-like nickel cobalt sulfide microspheres modified with nickel sulfide as Pt-free counter electrode for dye-sensitized solar cells, *J. Power Sources*, 2016, **304**, 266–272.

287 X. Qian, H. Li, L. Shao, X. Jiang and L. Hou, Morphology-tuned synthesis of nickel cobalt selenides as highly efficient Pt-free counter electrode catalysts for dye-sensitized solar cells, *ACS Appl. Mater. Interfaces*, 2016, **8**, 29486–29495.

288 R. G. Coleman, New occurrences of ferroselite (FeSe₂), *Geochim. Cosmochim. Acta*, 1959, **16**, 296–301.

289 H. D. Lutz and B. Müller, Lattice vibration spectra LXVIII. Single-crystal Raman spectra of marcasite-type iron chalcogenides and pnictides, FeX₂ (X = S, Se, Te; P, As, Sb), *Phys. Chem. Miner.*, 1991, **18**, 265–268.

290 E. Bastola, K. P. Bhandari, A. J. Matthews, N. Shrestha and R. J. Ellingson, Elemental anion thermal injection synthesis of nanocrystalline marcasite iron dichalcogenide FeSe₂ and FeTe₂, *RSC Adv.*, 2016, **6**, 69708–69714.

291 X. Mao, J. G. Kim, J. Han, H. S. Jung, S. G. Lee, N. A. Kotov and J. Lee, Phase-pure FeSe_x (x = 1, 2) nanoparticles with one-and two-photon luminescence, *J. Am. Chem. Soc.*, 2014, **136**, 7189–7192.

292 B. Yuan, W. Luan and S. T. Tu, One-step synthesis of cubic FeS₂ and flower-like FeSe₂ particles by a solvothermal reduction process, *Dalton Trans.*, 2012, **41**, 772–776.

293 J. Xu, K. Jang, J. Lee, H. J. Kim, J. Jeong, J. G. Park and S. U. Son, Phase-selective growth of assembled FeSe₂ nanorods from organometallic polymers and their surface magnetism, *Cryst. Growth Des.*, 2011, **11**, 2707–2710.

294 W. Shi, X. Zhang, G. Che, W. Fan and C. Liu, Controlled hydrothermal synthesis and magnetic properties of three-dimensional FeSe₂ rod clusters and microspheres, *Chem. Eng. J.*, 2013, **215**, 508–516.

295 X. Chang, J. Jian, G. Cai, R. Wu and J. Li, Three-dimensional FeSe₂ microflowers assembled by nanosheets: synthesis, optical properties, and catalytic activity for the hydrogen evolution reaction, *Electron. Mater. Lett.*, 2016, **12**, 237–242.

296 G. D. Park, J. H. Kim and Y. C. Kang, Large-scale production of spherical FeSe₂-amorphous carbon composite powders as anode materials for sodium-ion batteries, *Mater. Charact.*, 2016, **120**, 349–356.

297 B. G. Ganga, C. Ganeshraj, A. G. Krishna and P. N. Santhosh, Electronic and optical properties of FeSe₂ polymorphs: solar cell absorber, arXiv preprint arXiv:1303.1381, 2013.

298 R. Jin, K. Zhao, X. Pu, M. Zhang, F. Cai, X. Yang, H. Kim and Y. Zhao, Structural and photovoltaic properties of FeSe₂ films prepared by radio frequency magnetron sputtering, *Mater. Lett.*, 2016, **179**, 179–181.

299 D. Kong, J. J. Cha, H. Wang, H. R. Lee and Y. Cui, First-row transition metal dichalcogenide catalysts for hydrogen evolution reaction, *Energy Environ. Sci.*, 2013, **6**, 3553–3558.

300 J. Yang, G. H. Cheng, J. H. Zeng, S. H. Yu, X. M. Liu and Y. T. Qian, Shape control and characterization of transition metal diselenides MSe₂ (M = Ni, Co, Fe) prepared by a solvothermal-reduction process, *Chem. Mater.*, 2001, **13**, 848–853.

301 X. Chen and R. Fan, Low-temperature hydrothermal synthesis of transition metal dichalcogenides, *Chem. Mater.*, 2001, **13**, 802–805.

302 S. Huang, Q. He, W. Chen, Q. Qiao, J. Zai and X. Qian, Ultrathin FeSe₂ nanosheets: controlled synthesis and application as a heterogeneous catalyst in dye-sensitized solar cells, *Chem.-Eur. J.*, 2015, **21**, 4085–4091.

303 S. Huang, Q. He, W. Chen, J. Zai, Q. Qiao and X. Qian, 3D hierarchical FeSe₂ microspheres: controlled synthesis and applications in dye-sensitized solar cells, *Nano Energy*, 2015, **15**, 205–215.

304 W. Wang, X. Pan, W. Liu, B. Zhang, H. Chen, X. Fang, J. Yao and S. Dai, FeSe₂ films with controllable morphologies as efficient counter electrodes for dye-sensitized solar cells, *Chem. Commun.*, 2014, **50**, 2618–2620.

305 D. Kong, H. Wang, Z. Lu and Y. Cui, CoSe₂ nanoparticles grown on carbon fiber paper: an efficient and stable electrocatalyst for hydrogen evolution reaction, *J. Am. Chem. Soc.*, 2014, **136**, 4897–4900.

306 Y. Liu, H. Cheng, M. Lyu, S. Fan, Q. Liu, W. Zhang, Y. Zhi, C. Wang, C. Xiao, S. Wei and B. Ye, Low overpotential in vacancy-rich ultrathin CoSe₂ nanosheets for water oxidation, *J. Am. Chem. Soc.*, 2014, **136**, 15670–15675.

307 R. Wu, Y. Xue, B. Liu, K. Zhou, J. Wei and S. H. Chan, Cobalt diselenide nanoparticles embedded within porous carbon polyhedra as advanced electrocatalyst for oxygen reduction reaction, *J. Power Sources*, 2016, **330**, 132–139.

308 C. L. McCarthy, C. A. Downes, E. C. Schueller, K. Abuyen and R. L. Brutney, Method for the solution deposition of phase-pure CoSe₂ as an efficient hydrogen evolution reaction electrocatalyst, *ACS Energy Lett.*, 2016, **1**, 607–611.

309 J. Dong, J. Wu, J. Jia, S. Wu, P. Zhou, Y. Tu and Z. Lan, Cobalt selenide nanorods used as a high efficient counter electrode for dye-sensitized solar cells, *Electrochim. Acta*, 2015, **168**, 69–75.



310 I. T. Chiu, C. T. Li, C. P. Lee, P. Y. Chen, Y. H. Tseng, R. Vittal and K. C. Ho, Nanoclimbing-wall-like CoSe_2 /carbon composite film for the counter electrode of a highly efficient dye-sensitized solar cell: a study on the morphology control, *Nano Energy*, 2016, **22**, 594–606.

311 W. Y. Choi, Synthesis of CoSe_2/RGO composites and their application in a counter electrode of dye-sensitized solar cells, Master thesis, Department of Chemical Engineering, Graduate school of Ulsan National Institute of Science and Technology (UNIST), South Korea, 2015, <http://scholarworks.unist.ac.kr/handle/201301/10604>.

312 F. Gong, H. Wang, X. Xu, G. Zhou and Z. S. Wang, *In situ* growth of $\text{Co}_{0.85}\text{Se}$ and $\text{Ni}_{0.85}\text{Se}$ on conductive substrates as high-performance counter electrodes for dye-sensitized solar cells, *J. Am. Chem. Soc.*, 2012, **134**, 10953–10958.

313 H. Zhang, C. X. Liu, X. L. Qi, X. Dai, Z. Fang and S. C. Zhang, Topological insulators in Bi_2Se_3 , Bi_2Te_3 and Sb_2Te_3 with a single Dirac cone on the surface, *Nat. Phys.*, 2009, **5**, 438–442.

314 P. A. Sharma, A. L. Sharma, M. Hekmaty, K. Hattar, V. Stavila, R. Goeke, K. Erickson, D. L. Medlin, M. Brahlek, N. Koirala and S. Oh, Ion beam modification of topological insulator bismuth selenide, *Appl. Phys. Lett.*, 2014, **105**, 242106.

315 Y. Sun, H. Cheng, S. Gao, Q. Liu, Z. Sun, C. Xiao, C. Wu, S. Wei and Y. Xie, Atomically thick bismuth selenide freestanding single layers achieving enhanced thermoelectric energy harvesting, *J. Am. Chem. Soc.*, 2012, **134**, 20294–20297.

316 S. K. Batabyal, C. Basu, A. R. Das and G. S. Sanyal, Solvothermal synthesis of bismuth selenide nanotubes, *Mater. Lett.*, 2006, **60**, 2582–2585.

317 H. Tang, X. Wang, Y. Xiong, Y. Zhao, Y. Zhang, Y. Zhang, J. Yang and D. Xu, Thermoelectric characterization of individual bismuth selenide topological insulator nanoribbons, *Nanoscale*, 2015, **7**, 6683–6690.

318 Y. Zou, Z. G. Chen, Y. Huang, L. Yang, J. Drennan and J. Zou, Anisotropic electrical properties from vapor-solid-solid grown Bi_2Se_3 nanoribbons and nanowires, *J. Phys. Chem. C*, 2014, **118**, 20620–20626.

319 H. Zhu, E. Zhao, C. A. Richter and Q. Li, Topological insulator Bi_2Se_3 nanowire field effect transistors, *ECS Trans.*, 2014, **64**, 51–59.

320 Y. Fan, G. Hao, S. Luo, X. Qi and J. Zhong, Photoresponse properties of Bi_2Se_3 nanoplates, *Sci. Adv. Mater.*, 2015, **7**, 1589–1593.

321 X. Zhang, F. Wen, J. Xiang, X. Wang, L. Wang, W. Hu and Z. Liu, Wearable non-volatile memory devices based on topological insulator $\text{Bi}_2\text{Se}_3/\text{Pt}$ fibers, *Appl. Phys. Lett.*, 2015, **107**, 103109.

322 Z. Yuan, Z. Wu, S. Bai, W. Cui, J. Liu, T. Song and B. Sun, Layered bismuth selenide utilized as hole transporting layer for highly stable organic photovoltaics, *Org. Electron.*, 2015, **26**, 327–333.

323 Z. Li, Y. Hu, K. A. Howard, T. Jiang, X. Fan, Z. Miao, Y. Sun, F. Besenbacher and M. Yu, Multifunctional bismuth selenide nanocomposites for antitumor thermo-chemotherapy and imaging, *ACS Nano*, 2015, **10**, 984–997.

324 Z. Li, J. Liu, Y. Hu, K. A. Howard, Z. Li, X. Fan, M. Chang, Y. Sun, F. Besenbacher, C. Chen and M. Yu, Multimodal imaging-guided antitumor photothermal therapy and drug delivery using bismuth selenide spherical-sponge, *ACS Nano*, 2016, **10**, 9646–9658.

325 L. Zhu, K. Y. Cho and W. C. Oh, Microwave-assisted synthesis of $\text{Bi}_2\text{Se}_3/\text{reduced graphene oxide}$ nanocomposite as efficient catalytic counter electrode for dye-sensitized solar cell, *Fullerenes, Nanotubes, Carbon Nanostruct.*, 2016, **24**, 622–629.

326 A. L. Prieto, M. S. Sander, M. S. Martín-González, R. Gronsky, T. Sands and A. M. Stacy, Electrodeposition of ordered Bi_2Te_3 nanowire arrays, *J. Am. Chem. Soc.*, 2001, **123**, 7160–7161.

327 L. Ma, Q. Zhang, Q. Zhao, Z. Li, C. Ji and X. J. Xu, Synthesis and characterization of $\text{Bi}_2\text{Te}_3/\text{Te}$ superlattice nanowire arrays, *J. Nanosci. Nanotechnol.*, 2016, **16**, 1207–1210.

328 J. Lee, J. Kim, W. Moon, A. Berger and J. Lee, Enhanced seebeck coefficients of thermoelectric Bi_2Te_3 nanowires as a result of an optimized annealing process, *J. Phys. Chem. C*, 2012, **116**, 19512–19516.

329 J. Gooth, R. Zierold, P. Sergelius, B. Hamdou, J. Garcia, C. Damm, B. Rellinghaus, H. J. Pettersson, A. Pertsova, C. Canali and M. Borg, Local magnetic suppression of topological surface states in Bi_2Te_3 nanowires, *ACS Nano*, 2016, **10**, 7180–7188.

330 R. Du, H. C. Hsu, A. C. Balram, Y. Yin, S. Dong, W. Dai, W. Zhao, D. Kim, S. Y. Yu, J. Wang and X. Li, Robustness of topological surface states against strong disorder observed in Bi_2Te_3 nanotubes, *Phys. Rev. B*, 2016, **93**, 195402.

331 J. S. Son, M. K. Choi, M. K. Han, K. Park, J. Y. Kim, S. J. Lim, M. Oh, Y. Kuk, C. Park, S. J. Kim and T. Hyeon, n-Type nanostructured thermoelectric materials prepared from chemically synthesized ultrathin Bi_2Te_3 nanoplates, *Nano Lett.*, 2012, **12**, 640–647.

332 H. W. Tsai, T. H. Wang, T. C. Chan, P. J. Chen, C. C. Chung, A. Yaghoubi, C. N. Liao, E. W. G. Diau and Y. L. Chueh, Fabrication of large-scale single-crystal bismuth telluride (Bi_2Te_3) nanosheet arrays by a single-step electrolysis process, *Nanoscale*, 2014, **6**, 7780–7785.

333 L. Miao, J. Yi, Q. Wang, D. Feng, H. He, S. Lu, C. Zhao, H. Zhang and S. Wen, Broadband third order nonlinear optical responses of bismuth telluride nanosheets, *Opt. Mater. Express*, 2016, **6**, 2244–2251.

334 N. W. Park, J. Y. Ahn, A. Umar, S. G. Yoon and S. K. Lee, Thermoelectric properties of n-type bismuth telluride (Bi_2Te_3) thin films prepared by RF sputtering, *Sci. Adv. Mater.*, 2016, **8**, 1172–1176.

335 Y. Dou, F. Wu, L. Fang, G. Liu, C. Mao, K. Wan and M. Zhou, Enhanced performance of dye-sensitized solar cell using Bi_2Te_3 nanotube/ZnO nanoparticle composite photoanode by the synergistic effect of photovoltaic and thermoelectric conversion, *J. Power Sources*, 2016, **307**, 181–189.

336 K. Wan, F. Wu, Y. Dou, L. Fang and C. Mao, Enhance the performance of dye-sensitized solar cells by Bi_2Te_3 nanosheet/ZnO nanoparticle composite photoanode, *J. Alloys Compd.*, 2016, **680**, 373–380.

337 T. Chen, G. H. Guai, C. Gong, W. Hu, J. Zhu, H. Yang, Q. Yan and C. M. Li, Thermoelectric Bi_2Te_3 -improved charge collection for high-performance dye-sensitized solar cells, *Energy Environ. Sci.*, 2012, **5**, 6294–6298.

338 L. Hu, L. Fang, F. Wu and J. Wang, Effect of the size of Bi_2Te_3 nanoplates on the performance of TiO_2 -based novel hybrid DSSC combined PV and TE effect, in *MRS Proceedings (Vol. 1640, mrsf13-1640)*, Cambridge University Press, 2014.

339 A. Hinsch, J. M. Kroon, R. Kern, I. Uhendorf, J. Holzbock, A. Meyer and J. Ferber, Long-term stability of dye-sensitized solar cells, *Prog. Photovoltaics*, 2001, **9**, 425–438.

340 H. Pettersson and T. Gruszecki, Long-term stability of low-power dye-sensitized solar cells prepared by industrial methods, *Sol. Energy Mater. Sol. Cells*, 2001, **70**, 203–212.

341 P. M. Sommeling, M. Späth, H. J. P. Smit, N. J. Bakker and J. M. Kroon, Long-term stability testing of dye-sensitized solar cells, *J. Photochem. Photobiol. A*, 2004, **164**, 137–144.

342 M. Grätzel, Photovoltaic performance and long-term stability of dye-sensitized mesoscopic solar cells, *C. R. Chim.*, 2006, **9**, 578–583.

343 S. Dai, J. Weng, Y. Sui, S. Chen, S. Xiao, Y. Huang, F. Kong, X. Pan, L. Hu, C. Zhang and K. Wang, The design and outdoor application of dye-sensitized solar cells, *Inorg. Chim. Acta*, 2008, **361**, 786–791.

344 Y. Takeda, N. Kato, K. Higuchi, A. Takeichi, T. Motohiro, S. Fukumoto, T. Sano and T. Toyoda, Monolithically series-interconnected transparent modules of dye-sensitized solar cells, *Sol. Energy Mater. Sol. Cells*, 2009, **93**, 808–811.

345 M. I. Asghar, K. Miettunen, J. Halme, P. Vahermaa, M. Toivola, K. Aitola and P. Lund, Review of stability for advanced dye solar cells, *Energy Environ. Sci.*, 2010, **3**, 418–426.

346 A. G. Kontos, T. Stergiopoulos, V. Likodimos, D. Milliken, H. Desilvestro, G. Tulloch and P. Falaras, Long-term thermal stability of liquid dye solar cells, *J. Phys. Chem. C*, 2013, **117**, 8636–8646.

347 R. Jiang, A. Anderson, P. R. Barnes, L. Xiaoe, C. Law and B. C. O'Regan, 2000 hours photostability testing of dye sensitised solar cells using a cobalt bipyridine electrolyte, *J. Mater. Chem. A*, 2014, **2**, 4751–4757.

348 F. Sauvage, A review on current status of stability and knowledge on liquid electrolyte-based dye-sensitized solar cells, *Adv. Chem.*, 2014, 939525, DOI: /10.1155/2014/939525.

349 S. Yun, P. D. Lund and A. Hinsch, Stability assessment of alternative platinum free counter electrodes for dye-sensitized solar cells, *Energy Environ. Sci.*, 2015, **8**, 3495–3514.

350 C. J. Liu, S. Y. Tai, S. W. Chou, Y. C. Yu, K. D. Chang, S. Wang, F. S. S. Chien, J. Y. Lin and T. W. Lin, Facile synthesis of MoS_2 /graphene nanocomposite with high catalytic activity toward triiodide reduction in dye-sensitized solar cells, *J. Mater. Chem.*, 2015, **22**, 21057–21064.

351 H. Sun, L. Zhang and Z. S. Wang, Single-crystal CoSe_2 nanorods as an efficient electrocatalyst for dye-sensitized solar cells, *J. Mater. Chem. A*, 2014, **2**, 16023–16029.

352 N. Kato, Y. Takeda, K. Higuchi, A. Takeichi, E. Sudo, H. Tanaka, T. Motohiro, T. Sano and T. Toyoda, Degradation analysis of dye-sensitized solar cell module after long-term stability test under outdoor working condition, *Sol. Energy Mater. Sol. Cells*, 2009, **93**, 893–897.

353 H. Matsui, K. Okada, T. Kitamura and N. Tanabe, Thermal stability of dye-sensitized solar cells with current collecting grid, *Sol. Energy Mater. Sol. Cells*, 2009, **93**, 1110–1115.

354 G. Xue, Y. Guo, T. Yu, J. Guan, X. Yu, J. Zhang, J. Liu and Z. Zou, Degradation mechanisms investigation for long-term thermal stability of dye-sensitized solar cells, *Int. J. Electrochem. Sci.*, 2012, **7**, 1496–1511.

355 R. Harikisun and H. Desilvestro, Long-term stability of dye solar cells, *Sol. Energy*, 2011, **85**, 1179–1188.

356 Y. Wu, W. H. Zhu, S. M. Zakeeruddin and M. Grätzel, Insight into D-A-π-A structured sensitizers: a promising route to highly efficient and stable dye-sensitized solar cells, *ACS Appl. Mater. Interfaces*, 2015, **7**, 9307–9318.

357 R. Katoh, A. Furube, S. Mori, M. Miyashita, K. Sunahara, N. Kouruma and K. Hara, Highly stable sensitizer dyes for dye-sensitized solar cells: role of the oligothiophene moiety, *Energy Environ. Sci.*, 2009, **2**, 542–546.

358 D. Joly, L. Pellejà, S. Narbey, F. Oswald, J. Chiron, J. N. Clifford, E. Palomares and R. Demadrille, A robust organic dye for dye sensitized solar cells based on iodine/iodide electrolytes combining high efficiency and outstanding stability, *Sci. Rep.*, 2014, **4**, 4033.

359 Z. S. Wang, Y. Cui, K. Hara, Y. Dan-oh, C. Kasada and A. Shinpo, A high-light-harvesting-efficiency coumarin dye for stable dye-sensitized solar cells, *Adv. Mater.*, 2007, **19**, 1138–1141.

360 S. Kim, D. Kim, H. Choi, M. S. Kang, K. Song, S. O. Kang and J. Ko, Enhanced photovoltaic performance and long-term stability of quasi-solid-state dye-sensitized solar cells via molecular engineering, *Chem. Commun.*, 2008, 4951–4953.

361 X. Lu, Q. Feng, T. Lan, G. Zhou and Z. S. Wang, Molecular engineering of quinoxaline-based organic sensitizers for highly efficient and stable dye-sensitized solar cells, *Chem. Mater.*, 2012, **24**, 3179–3187.

362 S. Yanagida, Y. Yu and K. Manseki, Iodine/iodide-free dye-sensitized solar cells, *Acc. Chem. Res.*, 2009, **42**, 1827–1838.

363 H. Tian and L. Sun, Iodine-free redox couples for dye-sensitized solar cells, *J. Mater. Chem.*, 2011, **21**, 10592–10601.

364 M. Wang, C. Grätzel, S. M. Zakeeruddin and M. Grätzel, Recent developments in redox electrolytes for dye-sensitized solar cells, *Energy Environ. Sci.*, 2012, **5**, 9394–9405.

365 S. Ahmad, T. Bessho, F. Kessler, E. Baranoff, J. Frey, C. Yi, M. Grätzel and M. K. Nazeeruddin, A new generation of platinum and iodine free efficient dye-sensitized solar cells, *Phys. Chem. Chem. Phys.*, 2012, **14**, 10631–10639.



366 J. Cong, X. Yang, L. Kloo and L. Sun, Iodine/iodide-free redox shuttles for liquid electrolyte-based dye-sensitized solar cells, *Energy Environ. Sci.*, 2012, **5**, 9180–9194.

367 F. Sauvage, S. Chhor, A. Marchioro, J. E. Moser and M. Grätzel, Butyronitrile-based electrolyte for dye-sensitized solar cells, *J. Am. Chem. Soc.*, 2011, **133**, 13103–13109.

368 J. Yoon, D. Kang, J. Won, J. Y. Park and Y. S. Kang, Dye-sensitized solar cells using ion-gel electrolytes for long-term stability, *J. Power Sources*, 2012, **201**, 395–401.

369 K. M. Lee, W. H. Chiu, M. D. Lu and W. F. Hsieh, Improvement on the long-term stability of flexible plastic dye-sensitized solar cells, *J. Power Sources*, 2011, **196**, 8897–8903.

370 Y. Yang, C. H. Zhou, S. Xu, H. Hu, B. L. Chen, J. Zhang, S. J. Wu, W. Liu and X. Z. Zhao, Improved stability of quasi-solid-state dye-sensitized solar cell based on poly(ethylene oxide)-poly(vinylidene fluoride) polymer-blend electrolytes, *J. Power Sources*, 2008, **185**, 1492–1498.

371 Z. Chen, H. Yang, X. Li, F. Li, T. Yi and C. Huang, Thermostable succinonitrile-based gel electrolyte for efficient, long-life dye-sensitized solar cells, *J. Mater. Chem.*, 2007, **17**, 1602–1607.

372 K. T. Dembele, R. Nechache, L. Nikolova, A. Vomiero, C. Santato, S. Licoccia and F. Rosei, Effect of multi-walled carbon nanotubes on the stability of dye sensitized solar cells, *J. Power Sources*, 2013, **233**, 93–97.

373 S. R. Kim, M. K. Parvez, I. In, H. Y. Lee and J. M. Park, Novel photo-crosslinkable polymeric electrolyte system based on poly(ethylene glycol) and trimethylolpropane triacrylate for dye-sensitized solar cell with long-term stability, *Electrochim. Acta*, 2009, **54**, 6306–6311.

374 F. Sauvage, M. K. Fischer, A. Mishra, S. M. Zakeeruddin, M. K. Nazeeruddin, P. Bäuerle and M. Grätzel, A dendritic oligothiophene ruthenium sensitizer for stable dye-sensitized solar cells, *ChemSusChem*, 2009, **2**, 761–768.

375 M. K. Parvez, I. In, J. M. Park, S. H. Lee and S. R. Kim, Long-term stable dye-sensitized solar cells based on UV photo-crosslinkable poly(ethylene glycol) and poly(ethylene glycol) diacrylate based electrolytes, *Sol. Energy Mater. Sol. Cells*, 2011, **95**, 318–322.

376 F. Bella, D. Pugliese, J. R. Nair, A. Sacco, S. Bianco, C. Gerbaldi, C. Barolo and R. Bongiovanni, A UV-crosslinked polymer electrolyte membrane for quasi-solid dye-sensitized solar cells with excellent efficiency and durability, *Phys. Chem. Chem. Phys.*, 2013, **15**, 3706–3711.

377 F. Bella, G. Griffini, M. Gerosa, S. Turri and R. Bongiovanni, Performance and stability improvements for dye-sensitized solar cells in the presence of luminescent coatings, *J. Power Sources*, 2015, **283**, 195–203.

378 S. Singh and H. S. Nalwa, Nanotechnology and health safety-toxicity and risk assessments of nanostructured materials on human health, *J. Nanosci. Nanotechnol.*, 2007, **7**, 3048–3070.

379 *Nanotoxicology-Interactions of Nanomaterials with Biological Systems*, ed. Y. L. Zhao and H. S. Nalwa, American Scientific Publishers, Los Angeles, 2007.

380 X. Hu and Q. Zhou, Health and Ecosystem Risks of Graphene, *Chem. Rev.*, 2013, **113**, 3815–3835.

381 E. L. K. Chng and M. Pumera, Toxicity of graphene related materials and transition metal dichalcogenides, *RSC Adv.*, 2015, **5**, 3074–3080.

382 J. Hao, G. Song, T. Liu, X. Yi, K. Yang, L. Cheng and Z. Liu, *In vivo* long-term biodistribution, excretion, and toxicology of PEGylated transition-metal dichalcogenides MS_2 ($M = Mo, W, Ti$) nanosheets, *Adv. Sci.*, 2017, **4**, 1600160, DOI: 10.1002/advs.201600160.

383 W. Z. Teo, E. L. K. Chng, Z. Sofer and M. Pumera, Cytotoxicity of exfoliated transition-metal dichalcogenides (MoS_2 , WS_2 , and WSe_2) is lower than that of graphene and its analogues, *Chem.-Eur. J.*, 2014, **20**, 9627–9632.

